Calculation of Faraday Rotation Angle from SMOS Radiometric Data

A Degree Thesis

Submitted to the Faculty of the

Escola Tècnica d'Enginyeria de Telecomunicació de Barcelona

Universitat Politècnica de Catalunya

by

Paola Villalobos Feliu

In partial fulfilment

of the requirements for the degree in

TELECOMMUNICATIONS ENGINEERING

Advisor: Nuria Duffo Ubeda

Barcelona, June 2022

Abstract

The Faraday Rotation (FR) consists of a rotation in the components of the electromagnetic field emitted by the Earth as it propagates through the ionosphere. It depends on the frequency, the geomagnetic field, and the Vertical Total Electron Content (VTEC) of the ionosphere. For the Soil Moisture and Ocean Salinity (SMOS) mission, which operates in the L-band, this effect is not negligible and must be compensated.

This project is born from a methodology that consists of the estimation of the ionosphere VTEC of every SMOS overpass through an inversion procedure based on the measured FRA. However, there are some zones where the FRA and VTEC cannot be retrieved due to the presence of Radio Frequency Interferences (RFI) or in zones of dense forest or ice.

In order to improve the maps of the recovered VTEC and FRA, these zones where they cannot be recovered have been analyzed. First, the brightness temperature (TB) maps have been reproduced and the FRA formula has been analyzed to observe in detail where the FRA cannot be recovered, focusing on Canada. It will be found that this happens because of an indetermination of the formula.

Then, three approaches will be proposed, each one with a different methodology with the aim of improving the recovered VTEC maps. The VTEC cannot have negative values, but in the core methodology, some negative values appear which are then rejected when plotting them on the map, since they correspond to VTEC values that have not been correctly recovered. Therefore, the VTEC recovery maps will be improved by applying one of these approaches, although the statistic will worsen a bit.

Finally, more suitable and optimal thresholds are going to be looked for in order to improve the statistics of the maps.

Resum

La Rotació de Faraday (RF) consisteix en una rotació en els components del camp electromagnètic emès per la Terra en propagar-se per la ionosfera. Depèn de la freqüència, del camp geomagnètic i del contingut total vertical d'electrons (VTEC) de la ionosfera. Per a la missió *Soil Moisture and Ocean Salinity* (SMOS), que opera en la banda L, aquest efecte no és menyspreable i ha de ser compensat.

Aquest projecte neix d'una metodologia que consisteix en l'estimació del VTEC de la ionosfera de cada passada del SMOS mitjançant un procediment invers basat en el FRA mesurat. No obstant això, hi ha algunes zones en les quals el FRA i el VTEC no es poden recuperar a causa de la presència d'interferències de radiofreqüència (RFI) o en zones de bosc o gel.

Per a poder millorar la recuperació de la FRA i el VTEC, s'han analitzat aquestes zones on no es poden recuperar. Primer, s'han reproduït els mapes de temperatura de lluentor (TB) i s'ha analitzat la fórmula del FRA per a poder observar amb detall on i perquè no es pot recuperar el FRA, centrant-nos en el Canadà. Es veurà que això es produeix a causa d'una indeterminació de la fórmula.

Després, es presentaran tres enfocaments, cadascun amb una metodologia diferent amb la finalitat de millorar els mapes de la recuperació de VTEC. El VTEC no pot tenir valors negatius, no obstant això, en la metodologia apareixen alguns valors negatius que després són rebutjats al moment de fer les gràfiques, ja que corresponen a valors de VTEC que no han estat recuperats correctament. Pel que, en aplicar un d'aquests tres enfocaments, els mapes de la recuperació de VTEC milloraran però empitjorant una mica les estadístiques.

Per últim, es buscaran llindars més adequats i òptims per a millorar les estadístiques dels mapes.

Resumen

La Rotación de Faraday (RF) consiste en una rotación en los componentes del campo electromagnético emitido por la Tierra al propagarse por la ionosfera. Depende de la frecuencia, del campo geomagnético y del contendido total vertical de electrones (VTEC) de la ionosfera. Para la misión *Soil Moisture and Ocean Salinity* (SMOS), que opera en la banda L, este efecto no es despreciable y debe ser compensado.

Este proyecto nace de una metodología que consiste en la estimación del VTEC de la ionosfera de cada pasada del satélite SMOS mediante un procedimiento inverso basado en el FRA medido. Sin embargo, hay algunas zonas en las que el FRA y el VTEC no se pueden recuperar debido a la presencia de interferencias de radiofrecuencia (RFI) o en zonas de bosque o hielo.

Para poder mejorar la recuperación de la FRA y el VTEC, se han analizado estas zonas donde no se pueden recuperar. Primero, se han reproducido los mapas de temperatura de brillo (TB) y se ha analizado la fórmula del FRA para poder observar con detalle dónde y porqué no se puede recuperar el FRA, centrándonos en Canadá. Se verá que esto ocurre debido a una indeterminación de la fórmula.

Después, se presentarán tres enfoques, cada uno con una metodología diferente con el fin de mejorar los mapas de la recuperación de VTEC. El VTEC no puede tener valores negativos, sin embargo, en la metodología base aparecen algunos valores negativos que luego son rechazados al momento de hacer las gráficas, ya que corresponden a valores de VTEC que no han sido recuperados correctamente. Por lo que, al aplicar uno de estos tres enfoques, los mapas de la recuperación de VTEC mejorarán, aunque a veces empeorando un poco las estadísticas.

Por ultimo, se van a buscar umbrales más adecuados y óptimos para mejorar las estadísticas de los mapas.

Acknowledgements

Firstly, I would like to thank my advisor Nuria Duffo for her guidance, dedication, help, and for giving me the opportunity to learn a lot of new and interesting things through this project, I also want to thank Roselena Rubio for her help and support along the project.

And finally, I want to thank my partner, family, and friends for their support and encouragement. Without them I could not have made it this far.

Revision history and approval record

Revision	**Date**	**Purpose**
0	03/05/2022	Document creation
1	15/06/2022	Document revision
2	21/06/2022	Document revision

DOCUMENT DISTRIBUTION LIST

Name	**e-mail**
Paola Villalobos Feliu	Paola.valentina.villalobos@estudiantat.upc.edu
Nuria Duffo Ubeda	Nuria.duffo@upc.edu

Written by:		Reviewed and approved by:	
Date	03/05/2022	Date	15/06/2022
Name	Paola Villalobos Feliu	Name	Nuria Duffo Ubeda
Position	Project Author	Position	Project Supervisor

Table of contents

List of Figures

List of Tables:

1. Introduction

This project has been carried out at the Universitat Politècnica de Catalunya (UPC) at the Signal and Communications Theory Department, where they participate in the processing of the data obtained by SMOS (Soil Moisture and Ocean Salinity) satellite since its launch in 2009. The SMOS mission is carried out by the ESA (European Space Agency) with the objective of capturing global data to obtain Soil Moisture (SM) and Ocean Salinity (OS) maps, to improve the knowledge of the Earth's water cycle and the meteorological modelling. The unique SMOS payload is the Microwave Imaging Radiometer with Aperture Synthesis (MIRAS), that measures the brightness temperature of the Earth in the L-band [2].

There are a wide variety of applications such as meteorological disasters and fire prediction, plant growth monitoring, meteorological modelling, forest decline modelling, hydrological modelling, thin ice floating measurements, thermohaline circulation, absorption of CO_2 estimation, and others [21].

The Faraday Rotation (FR) consists of a rotation in the components of the electromagnetic field emitted by the Earth as it propagates through the ionosphere. It depends on the frequency, the geomagnetic field, and the Vertical Total Electron Content (VTEC) of the ionosphere. For the SMOS, that operates in the L-band, this effect is not negligible and must be compensated [20].

The Faraday Rotation can be retrieved from SMOS radiometric data. Despite this being possible by using MIRAS full-polarization mode and to the improvements made in image reconstruction (third and fourth Strokes parameters), it is not an easy task due to the thermal noise (relatively poor radiometric sensitivity) and spatial bias of MIRAS [3].

This project is born from a methodology, developed by Rubio, R. et al., 2022, that consists of the estimation of the ionosphere VTEC (Vertical Total Electron Content) of every SMOS overpass through an inversion procedure based on the measured FRA (Faraday Rotation Angle). It mitigates the effect of noise by using spatial-temporal filtering techniques and correcting the systematic error pattern when estimating the FRA and VTEC from SMOS measurements. However, there are some zones where the FRA and VTEC cannot be retrieved. This happens when the zone is contaminated by Radio Frequency Interferences (RFI), which degrade the quality of the brightness temperature. It also happens in zones of dense forest or ice because the electric field in both polarizations, horizontal and vertical, are practically equal, making the recovery of VTEC and FRA quite challenging [20].

In order to improve the maps of the recovered VTEC and FRA, these zones where they cannot be recovered are going to be analyzed. First, the brightness temperature maps are going to be reproduced and the formula of the FRA is going to be analyzed, to observe in detail where and why the FRA cannot be recovered, focusing on Canada.

Then, three approaches will be proposed, each one with a different methodology with the aim of improving the recovered VTEC maps. The VTEC cannot have negative values, but in the core methodology some negative values appear which are then rejected when plotting them on the map, since they correspond to VTEC values that have not been correctly recovered. Therefore, with these approaches, it will be tried to correctly recover the VTEC.

Finally, more suitable and optimal thresholds are going to be looked for in order to improve the statistics of the maps.

1.1. Scope

The purpose of this project is to retrieve the Vertical Total Electron Content (VTEC) from SMOS Radiometric Data with the aim to better correct the Faraday Rotation Angle (FRA) and to improve the quality of these maps.

This was done by using the MTS software, that is an independent processor developed at the UPC to analyze and process SMOS data in near real time. It reads the raw data sent by MIRAS transmitter and it automatically computes a series of data products which includes the levels: L1A (calibrated visibilities), L1B (brightness temperature maps in the antenna frame) and L1C (geolocated brightness temperatures) [6].

The project goals are:

1. To understand how an interferometric radiometer work, what brightness temperature is and how it is measured.
2. To learn how to use the MTS (MIRAS Testing Software) software that has been done in the Signal and Communications Theory Department with Matlab, in order to reproduce global temperature graphs and interpret their values.
3. To understand what Faraday Rotation (FR) is, how it can be measured and why it is of interest to know it efficiently. Reproduce FR and VTEC plots globally.
4. To investigate how can we improve the acquisition of the FRA and VTEC by studying the singularities it presents.
5. To find the more suitable noise thresholds to be taking into account and see if the statistics have improved.

1.2. Work Plan and Gantt diagram

1.2.1. Work Plan

Project: First Stage of Research	WP ref: (WP1)	
Major constituent: Research	Sheet 1 of 12	
Short description: Read information to familiarize with the SMOS mission, especially with this project application, in order to understand what the project is based on, the concepts involved, and the formulas used.	Planned start date: 01/02/2022 Planned end date: 28/02/2022 Start event: 01/02/2022 End event: 28/02/2022	
Internal task T1: To look in depth the official website, what is the SMOS mission and its applications. Internal task T2: Read about the Theoretical Framework of the SMOS. Internal task T3: Read about the Faraday Rotation Angle and Vertical Total Electron Content. Internal task T4: Read about the Faraday Rotation Angle and Vertical Total Electron Content from SMOS Radiometric Data.	Deliverables:	Dates:

Project: Getting familiarized with the Matlab program used	WP ref: (WP2)	
Major constituent: Simulation of the plots used on the thesis	Sheet 2 of 12	
Short description: Getting familiar with the Matlab program used to extract the Bright Temperatures (TB), Faraday Rotation Angle (FRA) and Vertical Total Electron Content (VTEC). Using the Matlab program and with a first input data L1B file provided, to reproduce different maps.	Planned start date: 23/02/2022 Planned end date: 15/03/2022 Start event: 23/02/2022 End event: 15/03/2022	
Internal task T1: Using the Matlab function **L1Bviewer** to reproduce the Brightness Temperature (TB) maps of a first input data L1B file, to obtain Tx, Ty, T3 and T4 polarizations. Observe these maps in order to see if any interferences are found. Internal task T2: Using the Matlab function **L1Claunch** to reproduce T3, Tx and Ty maps (antenna frame), with the same input data L1B file. Compare the T3 and Tx-Ty polarizations and detect the areas where these values are zero (to detect singularities). Internal task T3: Using the Matlab function **FRA_processor** to reproduce the FRA and VTEC maps, with the same input data L1B files.	Deliverables:	Dates:

Project: Project Proposal and Work Plan	WP ref: (WP3)	
Major constituent: Documentation	Sheet 3 of 12	
Short description: Creating a document with my project proposal and working plan.	Planned start date: 15/02/2022 Planned end date: 8/03/2022 Start event: 28/02/2022 End event: 8/03/2022	
Internal task T1: Complete the document with my project proposal and working plan.	Deliverables: ProjectProposal_PVF	Dates: 08/03/2022

Project: Second Stage of Research	WP ref: (WP4)	
Major constituent: Research	Sheet 4 of 12	
Short description: Continue to read information to have a better understanding about SMOS.	Planned start date: 9/03/2022 Planned end date: 21/03/2022 Start event: 9/03/2022 End event: 21/03/2022	
Internal task T1: To see more in depth the development of a formula with all its scenarios. Internal task T2: Read about the Characterization and Correction of systematic error patterns in the Faraday Rotation Angle.	Deliverables:	Dates:

Project: Matlab program	WP ref: (WP5)	
Major constituent: Simulation of the plots used on the thesis	Sheet 5 of 12	
Short description: Using the Matlab program and with another input data L1B file, the one used in the thesis, to reproduce the same maps as in the thesis in order to analyze them. This input data L1B file was a **descending** and **ascending** orbit from the Pacific.	Planned start date: 21/03/2022 Planned end date: 11/04/2022	
	Start event: 21/03/2022 End event: 11/04/2022	
Internal task T1: Using the Matlab function **L1Bviewer** to reproduce the Brightness Temperature (TB) maps of the input data L1B file, to obtain Tx, Ty, T3 and T4 polarizations. Observe these maps in order to see if any interferences are found. Internal task T2: Using the Matlab function **L1Claunch** to reproduce T3, Tx and Ty maps (antenna frame), with the same input data L1B file. Compare the T3 and Tx-Ty polarizations and detect the areas where these values are zero (to detect singularities). Internal task T3: Using the Matlab function **FRA_processor** to reproduce the FRA and VTEC maps, with the same input data L1B files. Compare them with the ones in Chapter 5.	Deliverables:	Dates:

Project: Project Critical Review	WP ref: (WP6)	
Major constituent: Documentation	Sheet 6 of 12	
Short description: Creating the document Project Critical Review.	Planned start date: 31/03/2022 Planned end date: 14/04/2022	
	Start event: 04/04/2022 End event: 14/04/2022	
Internal task T1: Complete de document Project Critical Review	Deliverables: ProjectCriticalReview_PVF	Dates: 14/04/2022

Project: Analyzing FRA	WP ref: (WP7)	
Major constituent: Analysis and SW.	Sheet 7 of 12	
Short description: Improve the errors in the acquisition of the Faraday Rotation Angle (FRA) by studying the singularities it presents in two areas in particular.	Planned start date: 12/04/2022 Planned end date: 25/04/2022	
	Start event: 12/04/2022 End event: 25/04/2022	
Internal task T1: Investigate how the acquisition of the FRA can be improved by studying the singularities it presents. There are 2 areas to study in detail. Internal task T2: Look at the formula of FRA and the plots of TB in the Amazon zone, since in this zone the FRA cannot be recovered so we know for sure that there is a singularity (0/0) in the formula of FRA. Internal task T3: Reproduce the plots of TB in the Canada zone. Investigate what is going on and if this zone presents singularity in the formula of FRA. Internal task T4: Reproduce the plots but in the ground frame (Tv, Th) of this zone of Canada. Done with the L1Claunch function in Matlab. Investigate in detail what is happening. Internal task T5: Conclusions.	Deliverables:	Dates:

Project: Analyzing VTEC of descending orbits.	WP ref: (WP8)	
Major constituent: Analysis and SW.	Sheet 8 of 12	
Short description: There are zones where the VTEC gives a negative value, which does not make sense because VTEC can only have positive values, this happens mostly in the ascending orbits. Investigate the **descending orbits**, since they are not much affected, to see if applying the **new methodology**, we get the same results or if we even get an improvement.	Planned start date: 26/04/2022 Planned end date: 14/05/2022	
	Start event: 26/04/2022 End event: 14/05/2022	
Internal task T1: Reproduce the same descending orbit graphs as the core methodology to then compare them with the new methodology. Internal task T2: Apply the new methodology, which is applying first the temporal filer and then reject the pixels with a |costhB| < 0.05 over TB snapshots. This is done by modifying the Matlab code provided (FRA_processor). Internal task T3: Reproduce a plot of costhB. Internal task T4: Reproduce the recovered VTEC plots to see if they have improved.	Deliverables:	Dates:

Project: Analyzing VTEC of ascending orbits.	WP ref: (WP9)	
Major constituent: Analysis and SW.	Sheet 9 of 12	
Short description: There are zones where the VTEC gives a negative value, which does not make sense because VTEC can only have positive values, this happens in the ascending orbits. Investigate the **ascending orbits** to see why this is happening and if applying the **new methodology**, we stop having negative values of VTEC.	Planned start date: 26/04/2022 Planned end date: 14/05/2022	
	Start event: 16/05/2022 End event: 14/05/2022	
Internal task T1: Reproduce the same ascending orbit graphs as in the core methodology to then compare them with the new methodology. Internal task T2: Apply the new methodology, which is applying first the temporal filter and then reject the pixels with a |costhB| < 0.05 over TB snapshots. This is done by modifying the Matlab code provided (FRA_processor). Internal task T3: Reproduce a plot of costhB. Internal task T4: Reproduce the recovered VTEC plots to see if they have improved.	Deliverables:	Dates:

Project: Improving the methodology proposed	WP ref: (WP10)	
Major constituent: Analysis and SW.	Sheet 10 of 12	
Short description: Since the methodology proposed in WP8 and WP9 did not turn out as expected, a new methodology for improving the recovered VTEC maps (for descending and ascending orbits) is proposed.	Planned start date: 04/05/2022 Planned end date: 01/06/2022	
	Start event: 04/05/2022 End event: 01/06/2022	
Internal task T1: Modify the function “fra_calc2” in the Matlab code in order to improve the recovered VTEC maps. By directly obtaining the solution of FRA that not only is the minimum but also has the same sign as the costhB, in order to reject the negative VTEC values. Internal task T2: Directly reject the negative values of VTEC in the function “FRA_processor” in the Matlab code. Internal task T3: Adjust the scale of the maps.	Deliverables:	Dates:

Project: Analyzing FRA and VTEC	WP ref: (WP11)	
Major constituent: Analysis and SW.	Sheet 11 of 12	
Short description: Improve the error in the acquisition of Faraday Rotation Angle and Vertical Total Electron Content by improving the noise threshold.	Planned start date: 23/05/2022 Planned end date: 03/06/2022	
	Start event: 23/05/2022 End event: 03/06/2022	
Internal task T1: Find the more suitable noise thresholds to be taking into account. Internal task T2: Compare the VTEC difference plots using the old thresholds and obtaining the same plots using the new ones to see if the error improves.	Deliverables:	Dates:

Project: Final Project Template	WP ref: (WP12)	
Major constituent: Documentation	Sheet 12 of 12	
Short description: Creating the document Final Report Template.	Planned start date: 25/05/2022 Planned end date: 21/06/2022	
	Start event: 25/05/2022 End event: 21/06/2022	
Internal task T1: Complete the document Final Report Template	Deliverables: FinalReportTemplate_PVF	Dates: 21/06/2022

1.2.2. Work Plan Modifications

There have been some modifications along the project, different methodologies have been applied with respect to what was initially proposed. When the new methodology described in WP8 and WP9 was applied, the results obtained were not as expected, this will be explained in detail later on. Another way was proposed, they were divided into three different approaches each one with a proposed methodology to see which one achieves the results wanted. The WP have been restructured, the main changes are instead of applying first the temporal filter and then reject the pixels with a |costhB| < 0.05 over TB snapshots (done in the function *FRA_processor* of the MTS software), it was thought to modify the function *fra_calc2* instead. So first, it was tried to directly obtain the solution of FRA that not only is the minimum but also has the same sign as the costhB, in order to reject the negative VTEC values. Then, it was realized that there was an easy way of doing it, that directly rejecting the negative VTEC values in the function *FRA_processor*.

1.2.3. Milestones

Table 1.1. Milestones of the project.

WP#	Task#	Short title	Milestone / deliverable	Date (week)
WP2	T2	Reproduce Tx-Ty and T3 polarizations.		W7
WP2	T3	Reproduce FRA and VTEC maps		W8
WP3	T1	Document Project Proposal	ProjectProposal_PVF	W10
WP5	T2	Reproduce Tx-Ty and T3 polarizations with the input data of the thesis.		W14
WP5	T3	Reproduce FRA and VTEC maps with the input data of the thesis.		W15
WP6	T1	Document Project Critical Review	ProjectCriticalReview_PVF	W15
WP7	T5	Conclusions on the singularity of the FRA formula.		W17
WP8	T2	Applying new methodology on descending orbits.		W19
WP8	T4	Reproducing the new VTEC maps.		W19
WP9	T2	Applying new methodology on ascending orbits.		W19
WP9	T4	Reproducing the new VTEC maps.		W20
WP10	T2	Improving the methodology		W21
WP11	T1	Noise Thresholds		W21
WP12	T1	Document Final Report Template	FinalReportTemplate_PVF	W25

1.2.4. Gantt diagram

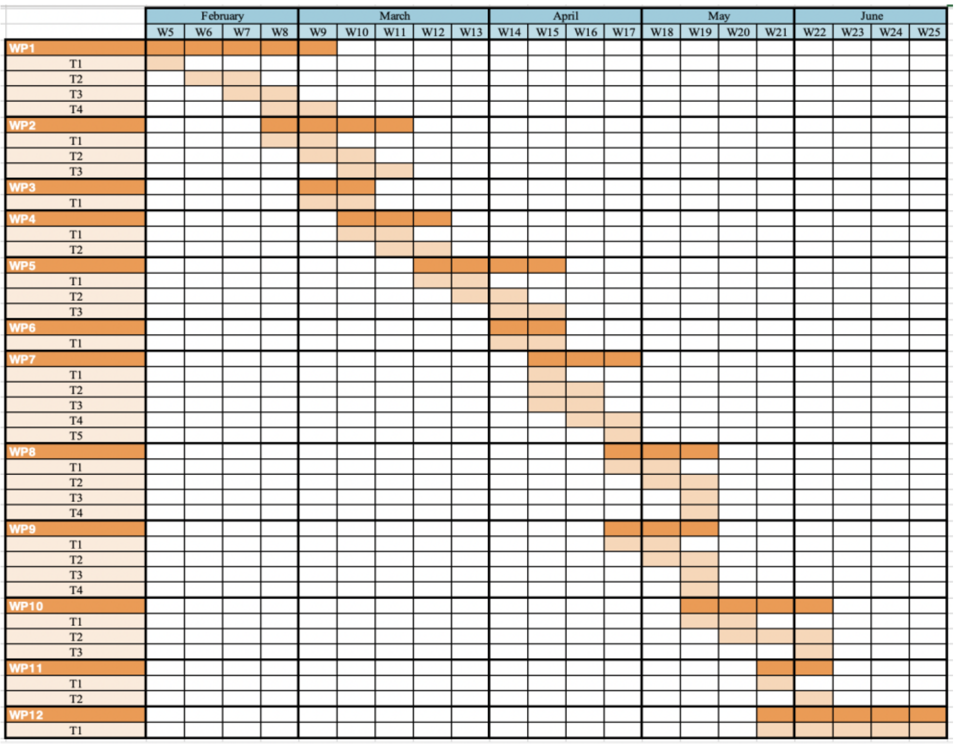

Figure 1.1. Gantt diagram.

2. State of the art of the technology used or applied in this thesis:

2.1. The SMOS Mission

On November of 2009, the Soil Moisture and Ocean Salinity (SMOS) satellite mission was launched by the ESA (European Space Agency), entering an orbit at 788.4 kilometres altitude. It is the second mission of the Earth Explorer Opportunity in the ESA's Living Planet Program. And due to the continuous exchange in Earth's water cycle between the land, the oceans, and the atmosphere, it is the first mission to provide global observations of soil moisture (SM) and ocean salinity (OS) variability, being these two the key parameters associated with the Earth's water cycle [1] [2].

The objective of this mission is to have a better understanding of the Earth's water cycle as from the processing of the data obtained from the satellite, these data are fundamental for the hydrological and vegetation studies that allows the development of various applications related to the Earth's water cycle. The SMOS satellite has been providing global maps every 3 days with a 50 km of spatial resolution [4].

The satellite acquires global earth data from the microwave emission (L-band) of the unique payload it carries. The L-band, in the low microwave frequency range, allows measurements to be unaffected by the atmosphere and clouds, which means that the attenuation is low, and are able to penetrate vegetation, even in dark, to a depth of typically 5cm. Moreover, this band is protected for Earth exploration and research, preventing undesired human emission and Radio Frequency Interferences (RFI), although it is not fully respected.

The unique SMOS payload is the Microwave Imaging Radiometer with Aperture Synthesis (MIRAS), it is a two-dimensional L-band (1.4135 GHz) synthetic aperture radiometer.

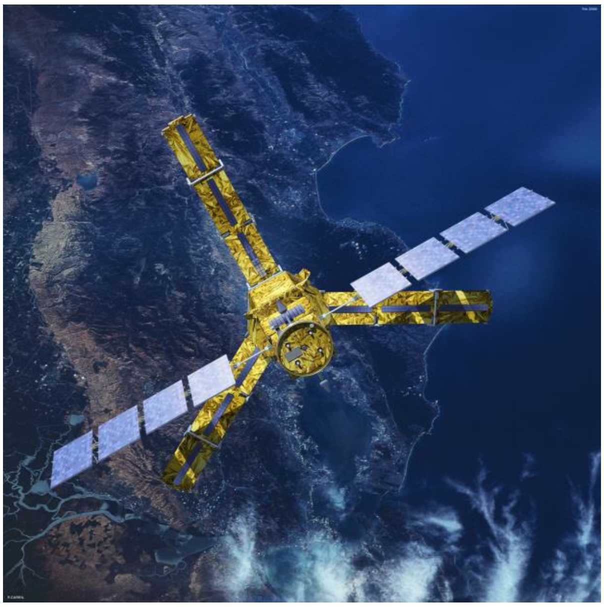

Figure 2.1. SMOS Satellite

The SMOS mission products obtained during the data processing are divided into:

- Raw data: received observation and telemetry data from the satellite.
- Level 0: consists of raw SMOS data including Earth Explorer headers.
- Level 1: are divided into three categories:
    - Level 1A (L1A): consist of calibrated visibilities, which is the output of the correlations between the different pairs of antennas.
    - Level 1B (L1B): consist of the Fourier components of brightness temperatures (TB) in the antenna frame of polarization reference at the measured instants (T_B^{xx}, T_B^{yy} and T_B^{xy}).
    - Level 1C (L1C): consist of the brightness temperature (TB) bands referenced to a fixed grid on a terrestrial ellipsoid (T_B^{hh}, $T_B^{vv}$and T_B^{hv}).
- Level 2: consist of swath-based maps of Soil Moisture and Ocean Salinity calculated from the data obtained on L1C.

2.2. MIRAS

MIRAS is an innovative two-dimensional L-band synthetic aperture radiometer. It has dual polarization and full polarimetry imaging capabilities that provides measurements of the brightness temperature of the Earth's surface at different angles of incidence. It consists of a central structure, called hub, connected to three equally spaced 8 m diameter deployable arms, which are Y-shaped. Each arm consists of three segments with six equally spaced receivers, known as LICEF (Lightweight Cost-Effective Front-End) that measure the phase difference of incident radiation. There are also NIRs (Noise Injection Radiometers) which are added for calibration purposes. Therefore, the required antenna aperture is synthesized by 69 antennas (66 LICEFs plus 3 NIRs) but 72 receivers (66 LICEFs plus 6. NIRs) [5].

LICEF units are radiometric receivers integrated with dual-polarized antennas that allow full polarimetric capabilities. These units generate 1-bit digital signals equivalent to the sign of the in-phase and quadrature components of the received noise signal. NIRs provides precise measurement of the scene's average brightness temperature. Both LICEFs and NIRs measure the radiometric temperature of the antenna. This stands for the radiation noise power delivered by the antenna to the receiver, corresponding to the brightness temperature of the scene [7].

Once the signal is acquired, it is transmitted to a central correlation unit. The technique consists of cross correlating the observations of every possible pair of receiver combinations. Every 1.2 seconds a two-dimensional "measurement image" is taken. Each observed area is viewed at different viewing angles as the satellite moves along its orbital path.

2.2.1. Measurements Fundamentals

The principle of operation of MIRAS is based on two-dimensional interferometric aperture synthesis, which consist of cross-correlation of the power density (antenna temperature) collected by every pair of antennas ($b_1(\mathrm{f})$ and $b_2(\mathrm{f})$), Eq. (2.1)

$$\overline{|b_1(\mathrm{f})|^2} = kT_{A1} \qquad \overline{|b_2(\mathrm{f})|^2} = kT_{A2} \qquad \rightarrow \qquad \overline{b_1(\mathrm{f})b_2^*(f)} = kV_{12} \tag{ 2.1}$$

Where $\overline{b_1(\mathrm{f})b_2^*(f)}$ corresponds to the cross-power density and V_{12} to the visibility function.

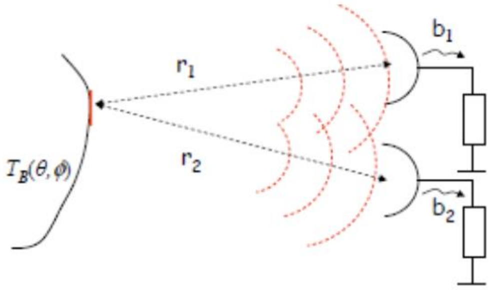

Figure 2.2. MIRAS Operating principle [6].

The aim is to measure the visibility function $V(u,v)$, to allow the reconstruction of the brightness temperature (TB) maps, these visibilities are processed in the data processor.

It has been concluded that the visibility function can be expressed as:

$$V_{12}(u,v) = \frac{1}{\sqrt{\Omega_1\Omega_2}} \iint_{\xi^2+\eta^2\le 1} \frac{T_B(\xi,\eta)-T_r}{\sqrt{1-\xi^2-\eta^2}} F_{n1}(\xi,\eta)F_{n2}^*(\xi,\eta)e^{-j2\pi(u\xi+v\eta)}\,d\xi d\eta \qquad (2.2)$$

Where Ω corresponds to the solid angle, the $T_B(\xi,\eta)$ to the brightness temperature, the T_r is the noise equivalent temperature generated by the receivers and entering the antennas, and $F_n(\xi,\eta)$ are antenna patterns in the director cosines.

Therefore, if all the antennas were the same and if $F_{n1}(\xi,\eta)F_{n2}^*(\xi,\eta)$ were common, by doing the inverse Fourier transform it would be possible to obtain the brightness temperatures (TB) from the visibility function. Or something similar if the antennas were different.

2.2.1.1. Field of View and Measurement Modes of MIRAS

As mentioned before, the MIRAS antennas are equally spaced, at a distance of $d = 0.875\lambda$. This distance does not meet the Nyquist criteria, which means that there will be aliasing in the field of view (FoV) of the TB snapshots.

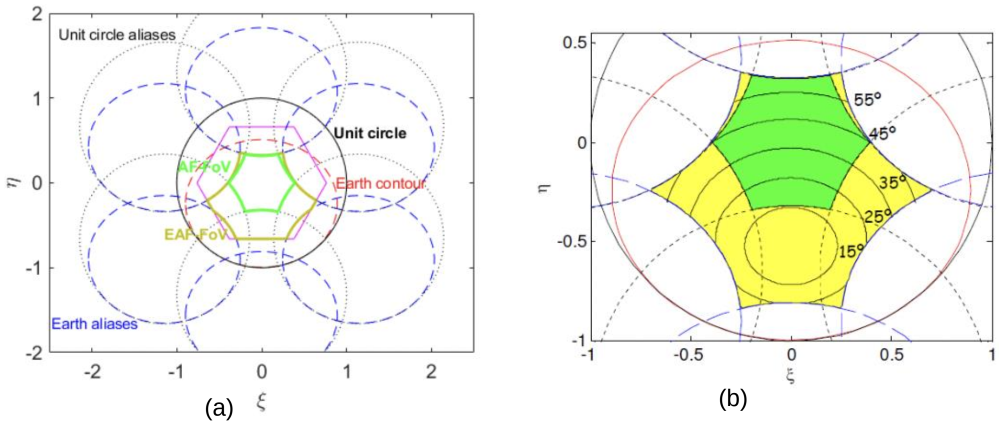

(a)

(b)

Figure 2.3. Field of View: (a)AF-FoV and EAF-FoV. (b)Incidence angles in SMOS antenna frame FoV [6].

Figure 2.3.a. Shows the Alias-Free Field of View (AF-FoV) that is the region without any overlapping by any circles (green line), and the Extended Alias-Free Field of View (EAF-FoV) is the extension of the AF-FoV in an area limited by the Earth-sky horizon (gold line). Figure 2.3.b. Shows the incidence angles at which MIRAS is able to measure due to its interferometric capabilities.

MIRAS is able to measure in full polarimetric mode, that means that it measures in the h, v polarizations, and in the cross-correlation hv and vh polarizations. To achieve this, it requires a four-step sequence in which each receiver has to select, in different orders, each polarization twice. At different instances of the sequence, it ends up obtaining hh, hv, vh, and vv correlations. Each of the four integration periods must be 1.2 s long.

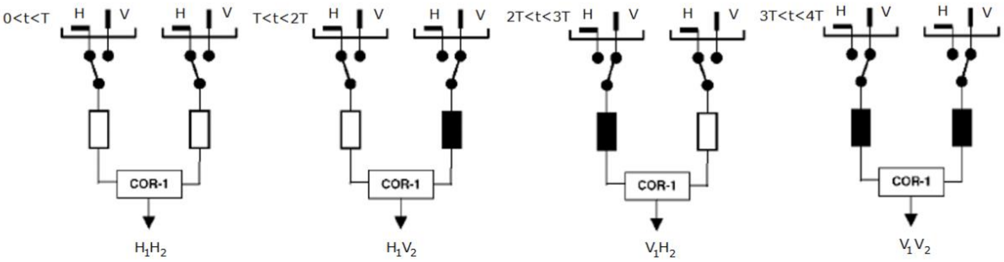

Figure 2.4. Example of the four different instances of the sequence, the switching of a pair of receivers [10].

In the first integration period, since all receivers are measuring in the horizontal polarization, samples of the hh-baseline are obtained. In the second integration period, there is only one arm (out of the three that MIRAS has) that is in one polarization, say the v-polarization, and the rest is in the other one, h-polarization. This implies that the vv, vh, and hv baselines visibilities samples are generated with a shorter integration time, obtaining a worse radiometric sensitivity. However, a complete TB polarimetric block is obtained after 2.4 s.

In the third integration time, all the receivers are in the v-polarization, a measurement of all vv-baseline samples with the same radiometric sensitivity as the hh-baselines samples of the first integration period is possible. The fourth integration period is the same as the second but with the other polarization, the h-polarization, and the hh, hv, and vh baselines visibilities are also generated with the same integration time as the second period [10].

Table 2.1. MIRAS arm switching sequence.

Integration period	Arm A	Arm B	Arm C	Integration time (s)
1st	H	H	H	1.2
2nd	V	H	H	0.4
	H	V	H	0.4
	H	H	V	0.4
3rd	V	V	V	1.2
4th	H	V	V	0.4
	V	H	V	0.4
	V	V	H	0.4

The radiometric sensitivity is the smallest variation of the brightness temperature that the instrument can measure. The hv and vh polarizations have a much worse radiometric sensitivity than the hh and vv polarizations, due to a shorter integration time.

2.2.1.2. Stokes Parameters

The Earth's surface radiates in both vertical and horizontal polarizations, which are orthogonal between them. The antennas have to measure in both polarizations to capture both contributions. The Stokes parameters are defined to describe an electromagnetic wave, there are four of them:

$$I_s = \begin{bmatrix} I \\ Q \\ U \\ V \end{bmatrix} = \begin{bmatrix} T_v + T_h \\ T_v - T_h \\ T_3 \\ T_4 \end{bmatrix}$$

(2.3)

The first parameter, I, represents the total radiated power density. The second one, Q, represents the difference between the power density in the vertical and horizontal polarizations. The last two parameters, T_3 and T_4, characterize the correlation between both h and v polarizations [11].

Between the ground frame of the Earth's surface (polarizations h and v) and the antenna frame of the instrument (polarizations x and y), a relative alignment exists. Consequently, there is a geometric rotation φ in each spatial direction from the instrument to the Earth's surface, that must be applied to T_B^{xx} and T_B^{yy} to obtain the brightness temperature in the ground frame [10].

Furthermore, the propagation axes rotate an angle equivalent to the Faraday Rotation (FR), this is due to the propagation of electromagnetic waves through the ionosphere. The total angle of rotation is:

$$\varphi_T = \varphi + \Omega_f$$

(2.4)

Under the assumption that T_B^{xy} and T_B^{yx} represents the complex cross-polarization brightness temperatures in the antenna frame, which are hermitic to each other, and that the h and v polarizations of the ground frame are uncorrelated, $T_B^{hv} = T_B^{vh} = 0$, the full polarimetric measurement of the instrument at each snapshot is related to the ground emission by:

$$\begin{bmatrix} T_B^{xx} \\ 2\Re e(T_B^{xy}) \\ T_B^{yy} \end{bmatrix} = \begin{bmatrix} cos^2(\varphi + \Omega_f) & sin^2(\varphi + \Omega_f) \\ -sin2(\varphi + \Omega_f) & sin2(\varphi + \Omega_f) \\ sin^2(\varphi + \Omega_f) & cos^2(\varphi + \Omega_f) \end{bmatrix} \begin{bmatrix} T_B^{hh} \\ T_B^{vv} \end{bmatrix}$$

(2.5)

Taking into account the geometric rotation and the correction of the Faraday Rotation Angle (FRA) introduced by the ionosphere, as well as the fact that the SMOS has multiangular information, the brightness temperatures have to be geolocated from the antenna frame (x and y polarizations) to the ground frame (h and v polarizations). The ESA chose the Icosahedral Snyder Equal Area (ISEA) grid, which provides the greatest angular resolution and the smallest average error.

2.2.1.3. Radio Frequency Interference

The Radio Frequency Interference (RFI) is "the effect of unwanted energy due to one or a combination of emissions, radiations, or inductions upon reception in a radio-communication system, manifested by any performance degradation, misinterpretation, or loss of information which could be extracted in the absence of such unwanted energy" defined by No. 1.166 of the ITU Radio Regulations (RR).

As mentioned before, the chosen frequency range for the SMOS was the L-band (1400 to 1427 MHz). This frequency corresponds to a protected band for exploration and research, being prohibited any other type of emissions in this band. Throughout the SMOS mission the presence of RFI has been proven to affect the recovery of the maps, making the SMOS very vulnerable by these illegal man-made emissions or by the operating stations in adjacent bands with both out-of-band and spurious emissions. A successful strategy to clean up RFI in its operating band was developed by the SMOS team, consisting of monitoring and reporting illegal transmissions, since the SMOS has no RFI protection on board like other satellites [8] [9].

2.3. FRA and VTEC

The FRA consists of a rotation in the components of the electromagnetic field as it propagates through the ionosphere. The ionosphere is the ionized part of the upper atmosphere of the Earth, that extends from 50 km to more than 600 km of altitude. It is ionized by the solar radiation.

The FRA can by defined as [11]:

$$\Omega_f = 1.355 * 10^4 \, f^{-2} B_0 \cos \Theta_B \sec \theta \; VTEC \tag{2.6}$$

The FRA corresponds to Ω_f in degrees; the f corresponds to the frequency in GHz; the B_0 to the magnitude of the geomagnetic field in Teslas; the Θ_B to the angle between the wave propagation direction and the magnetic field; the θ to the incidence angle; and the $VTEC$ to the Vertical Total Electron Content. The VTEC is the content of electrons in a vertical column of 1 m^2 expressed in TEC units, where a TEC unit ≈ 10^{16} electrons/m^2 [18].

The relationship between the FRA and VTEC is directly proportional. Therefore, the FRA is also determined by the diurnal and seasonal variation of the VTEC in local time (LT). The surviving amount of VTEC generated by sunlight during the previous hours is higher in the afternoon LT than in the morning LT.

2.3.1. FRA and VTEC Fundamentals

The FRA has a significant temporal and geophysical variability. The geophysical variability of the FRA does not have a defined pattern, apart from the change of sign that happens at the equatorial crossing, caused by the corresponding change of sign of the dip angle of the magnetic field. It is observed that the difference between the FRA magnitude in the descending orbits and ascending orbits is significant, the scale must be considered.

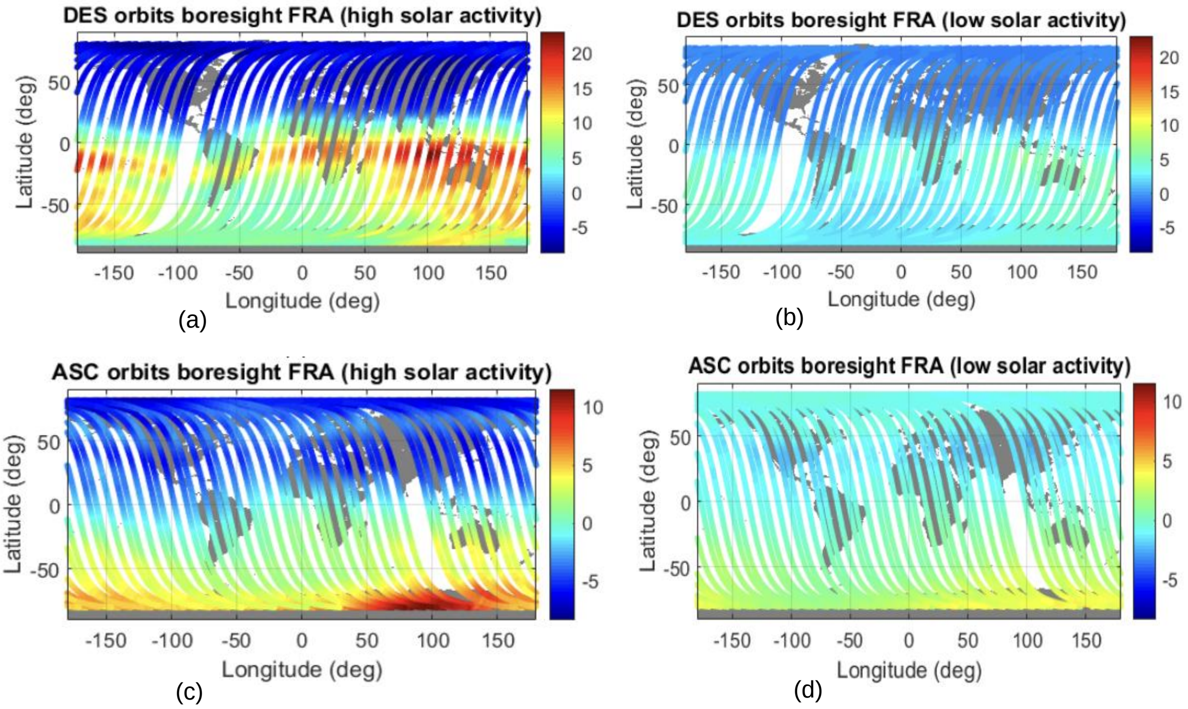

(a) (b) (c) (d)

Figure 2.5. FRA in the boresight coordinates of the SMOS for 3 consecutive days in different periods. (a) Descending orbit in March 2014, (b) Descending orbit January 2011, (c) Ascending orbit March 2014, (d) Ascending orbit January 2011. [19].

The solar activity is higher in the evening LT than in the morning, and given that the SMOS is a sun-synchronous orbit (between 6 a.m. and 6 p.m.), the descending orbits take place in the evening LT, and the ascending orbit in the morning LT. This means that the descending orbits have a much higher FRA and dynamic ranges than ascending orbits. There is also an important difference of the FRA magnitude through the years since each year has different solar activity. For example, the year 2014 has the highest solar activity during the whole period of the SMOS mission. In order to avoid the presence of RFI and to maximize the coverage of the measurements over the ocean, the orbits were chosen over the eastern Pacific Ocean.

A significant rotation of several degrees in the polarization of the electromagnetic field is introduced by the FR. If this is not considered, the measured TB is affected. Therefore, the FRA has to be compensated for obtaining more accurate SM and OS retrievals. To do so, FRA external data sources, VTEC datasets, and the Eq. (2.6) can be used.

2.3.1.1. Data Sources

There are datasets of FRA or VTEC coming from different satellites, the ones of interest are:

2.3.1.1.1. International GNSS Service (IGS) VTEC

The Ionosphere Working Group from the International GNSS (Global Navigation Satellite Systems) Service (IGS), has worked to have a product with the ionosphere vertical total electron content maps with a temporal resolution of 2 hours and a spatial resolution of 5ºx2.5º (longitude x latitude) in the IONosphere map Exchange format (IONEX), calculated at 20000 km of altitude. This group provides three products: the predicted solution (available both one and two days in advance), the rapid solution (available with a latency of less than 24 hours), and the final product (available about 11 days later) [13].

2.3.1.1.2. SMOS

In order to correct the FRA, the theoretical formulation (2.6) has been used to calculate the FRA with external sources: the International Geomagnetic Reference Field (IGRF) and the L1 VTEC.

The L1 VTEC data comes from the IGS VTEC but is used in the SMOS mission by applying a correction to eliminate the residual TEC that is above the SMOS altitude. So, the L1 VTEC is always below the IGS VTEC, because it considers the vertical electron content of fewer layers of the atmosphere.

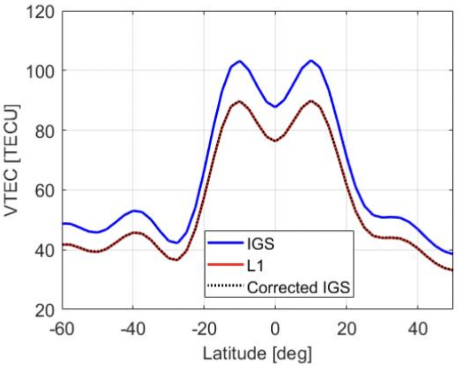

Figure 2.6. VTEC vs latitude of the middle pixel of a descending orbit of March 2014.

Different methodologies have been tried to extract the FRA and VTEC from SMOS radiometric data:

- A3TEC (Total Electron Content from Third Strokes Parameter at Antenna Level) [14]: A methodology was developed by the L2 team to calculate the VTEC from the SMOS radiometric data. It consists of a first-order Taylor approximation based on the use of the L1 VTEC. It has a parameter called OTT (Ocean Target Transformation) that compensates the systematic biases that are present in SMOS that are caused by imperfections in the instrument calibrations, the image reconstruction, the TB forward model, and external sources such as the Sun and galaxy [15]. This calculation is made in the area of the FoV that has the highest VTEC sensibility with respect to the T_3 over the antenna frame. This area corresponds to the 60º incidence angle circle.

- FRA from TB [3]: a methodology capable of retrieving the FRA from SMOS radiometric data has been developed. It comes from Eq. (2.5), where the FRA can be expressed as:

$$\Omega_f = -\varphi - \frac{1}{2}\arctan\left(\frac{2\Re e(T_B^{xy})}{T_B^{xx} - T_B^{yy}}\right) \tag{2.7}$$

  From where the FRA can be calculated from the TB, but this is going to be explained in detail later on in section 3.3.1.
  There are spatial errors in SMOS images due to calibration inaccuracy, image reconstruction artifacts, antenna pattern uncertainty, and are degraded by thermal noise [16]. Consequently, this methodology cannot be used to get instantaneous values of FRA at each pixel of the FoV, because of all the limitations in the quality of the retrieval. In order to reduce this effects, temporal and spatial techniques can be applied. Therefore, the retrieval is done only in a reference area of the FoV where

there is lowest thermal noise and minimum image reconstruction artifacts. [17]. A circle of radius 0.3 around the boresight has been chosen, it includes only part of the AF-FoV, avoiding pixels with 45º rotation [3].
Although this methodology is able to reproduce the natural variation of FR, it was found that assigning a single FRA value for the entire FoV is not representative due to the significant variation of the FRA in the SMOS FoV.

2.3.1.2. FRA End-to-End Simulator

There exists a simulator that was used as a starting point for choosing between the different approaches to derive the SMOS-VTEC maps and for the calculation of various parameters, such as the sizes of the temporal and spatial filter. It consists of emulating the TB in the antenna frame, and then extracting the FRA from them [18].

It is worth mentioning that, for simulated data, the error in the retrieval can be calculated, as the FRA used to generate the TB at the antenna frame (calculated from L1 VTEC) is known. However, for real SMOS data, the retrieval is compared to L1 VTEC only for reference, which means that these are differences and not errors.

2.3.2. FRA and VTEC from SMOS Radiometric Data

The Faraday Rotation measurement from radiometric data makes it possible to estimate the ionosphere's total electron content for each SMOS overpass by means of an inverse procedure. Therefore, a VTEC product can be derived from the SMOS data. Retrieving VTEC maps is more difficult for ascending orbits than for descending orbits, as the effect of noise masks the geophysical variation of VTEC to a larger extent, given that its variability range is much smaller [20].

The effect of noise masks the FRA and VTEC retrievals. When processing the SMOS radiometric data, both the effect of noise and the image reconstruction artifacts degrade the quality of the recovery.

The methodology, from which this project will be based on, will be explained below. It consists of mitigating the effect of noise by using spatial-temporal filtering techniques and correcting the systematic error pattern when estimating the FRA and VTEC from SMOS measurements [20].

2.3.2.1. Methodology to recover VTEC Maps [20]

1. Rejecting pixels with $|\cos\Theta_B| < 0.05$ over the TB snapshots to avoid the indetermination (when the geomagnetic field is orthogonal to the direction of the wave propagation, $\cos\Theta_B \approx 0$, mostly in the zones close to the equator) of:

$$VTEC = \frac{f^2\,\Omega_f \cos\theta}{1.355 * 10^4\, B_0 \cos\Theta_B} \tag{2.8}$$

2. A temporal filter is applied with a window size of 43 TB snapshots. This value was obtained with the simulator that considers the effect of noise.
   The temporal filter consists of an averaging triangular window that considers the current snapshot with the highest weight. The impact of applying the temporal filter

is that the FRA physical variation is not masked by the effect of noise, and the STD (standard derivation) improves.

3. The calculus of the measured FRA is done by using Eq. (2.7), repeated here:

$$\Omega_f^m = -\varphi - \frac{1}{2}\arctan\left(\frac{2\Re e\left(T_B^{xy}\right)}{T_B^{xx} - T_B^{yy}}\right)$$

4. In order to avoid the indetermination of Eq. (2.7), pixels with an incidence angle lower than 25º are rejected. This indetermination happens when both numerator and denominator tend to 0, $T_B^{xx} \approx T_B^{yy}$ and $T_3 \approx 0$. Low-incidence angles are rejected as they are the most affected part of the snapshot.

5. The estimated FRA is actually the sum of two components, the actual FRA (Ω_f) and the systematic error pattern (Δ). The error Δ is subtracted to Ω_f^m to obtain the actual FRA by using Eq. (2.9). Δ had been previously calculated for the entire mission using three consecutive days from years 2010 to 2019.

$$\Omega_f = \Omega_f^m - \Delta \tag{2.9}$$

   It mitigates the pattern in the swath of VTEC that does not corresponds to a geophysical variation, and also the STD has an important improvement.

6. The calculus of the VTEC is done by using Eq. (2.8).

7. A spatial filter with a radius of 0.189 is applied over the VTEC snapshots, at the antenna frame. This value was also obtained with the simulator that considers the effect of noise.
   When applying this filter, the STD of the error in the recovery of VTEC snapshots is very significant. The effect of the filter may be more noticeable in the ascending orbits, since the VTEC retrieval is highly affected by the effect of noise due to the small range of VTEC.

8. The VTEC AF-FoV value is extended to the EAF-FoV. This is done in order to mitigate the effects on swath lateral lines that occur during the VTEC recovery.
   An important statement is that the VTEC is a parameter that is always positive. As a result of the error in the recovery, some negative values appear in the snapshot.

9. The geolocation is done over an ETOPO-5 grid (resolution of 5 minutes of latitude and longitude), at 450 km of altitude. The measurements acquired at the same point on the grid are averaged.

It is important to mention that VTEC pixels with values lower that 0 TECU and higher than 120 TECU (in descending orbits) or higher than 40 TECU (in ascending orbits), are rejected because they correspond to error in the retrieval since the VTEC cannot have negative values.

In the plots, the pixels with negative VTEC are rejected. There are much more pixels rejected in ascending orbits than descending orbits, as said before, due to the effect of noise and its small range of VTEC variability [20].

The final plots were reproduced for descending orbits (figures at the left) and ascending orbits (figures at the right):

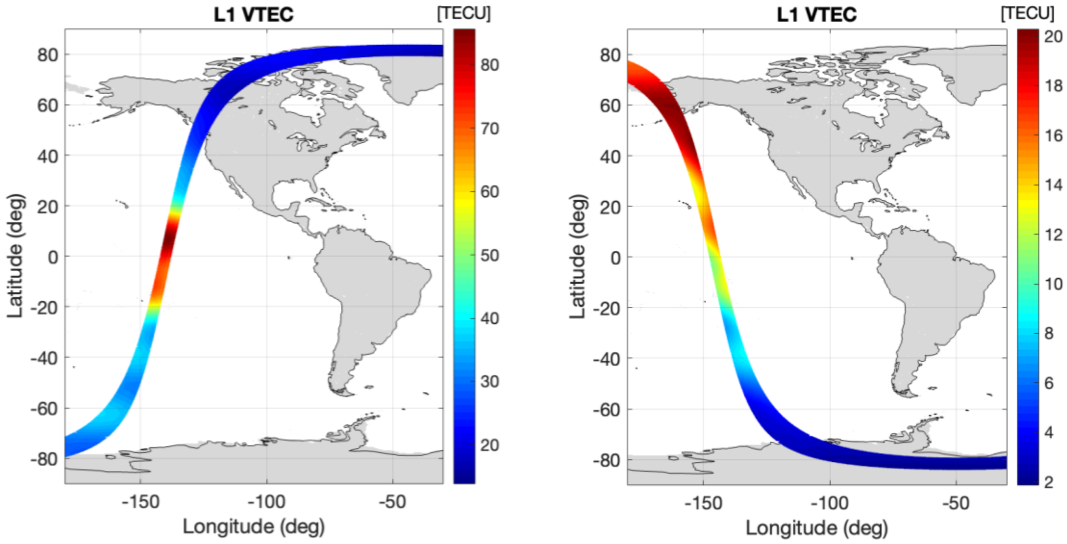

(a) (b)

Figure 2.8. L1 VTEC maps for: (a) Descending orbits, (b) Ascending orbits.

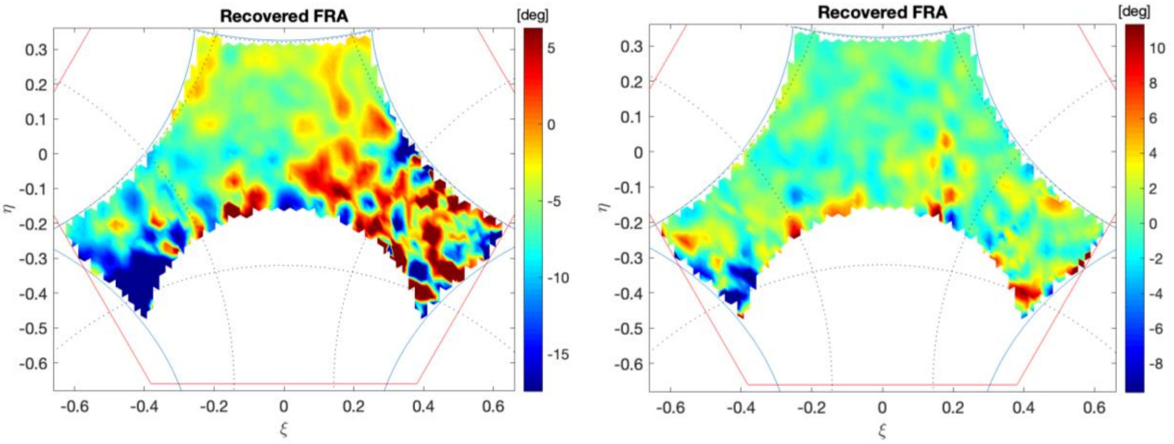

(a) (b)

Figure 2.7. Recovered FRA snapshoots of: (a) Descending orbits, (b) Ascending orbits.

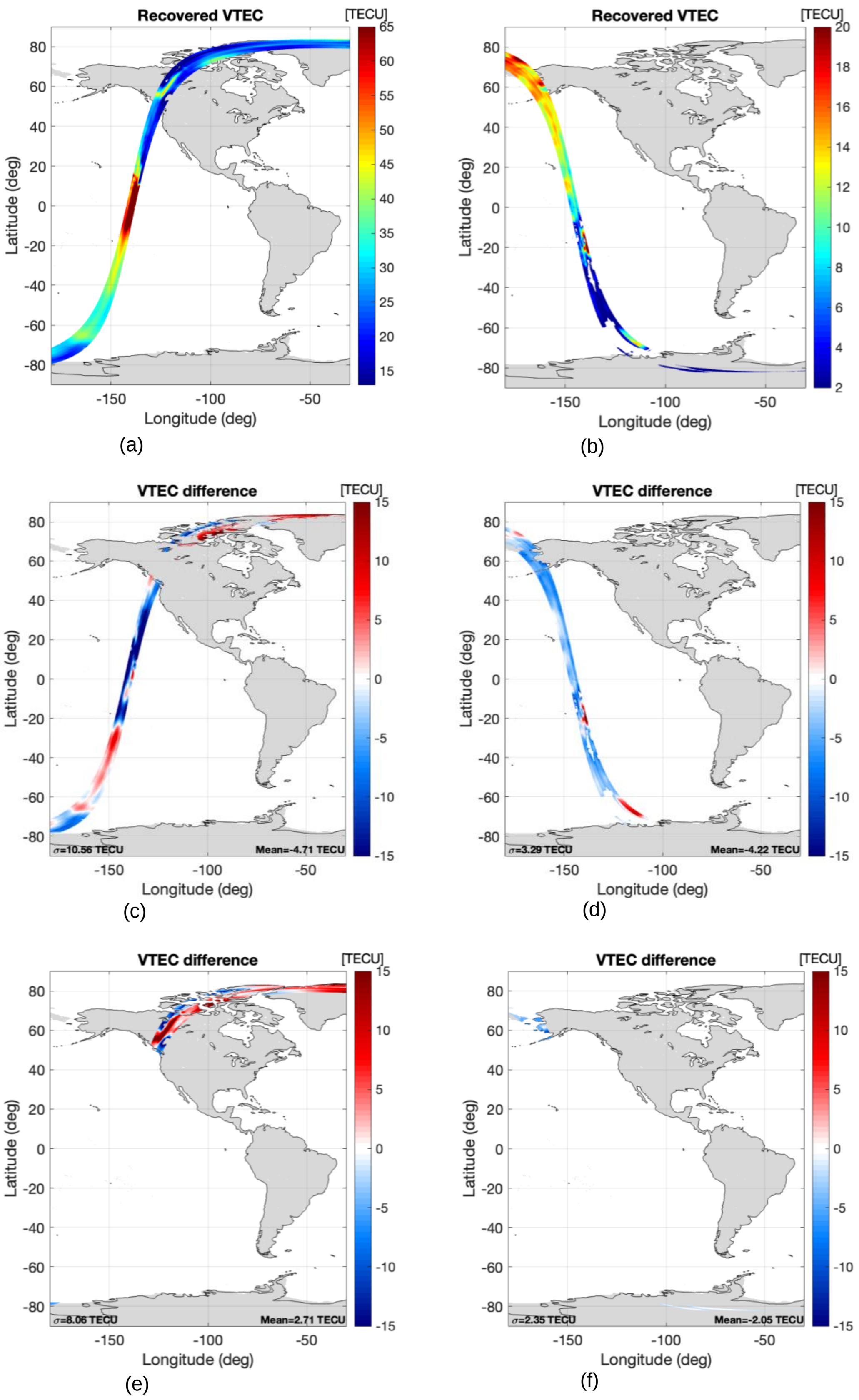

(a) (b)

(c) (d)

(e) (f)

*Figure 2.9. Maps of VTEC: <u>TOP</u>: Recovered VTEC (a) descending orbit, (b) ascending orbit. <u>MIDDLE</u>: Difference between recovered VTEC and L1 VTEC over **ocean** (c) descending orbit, (d) ascending orbit. <u>BOTTOM</u>: Difference between recovered VTEC and L1 VTEC over **land** (e) descending orbit, (f) ascending orbit.*

Then, the comparison of the FRA recovery from the retrieved VTEC from SMOS radiometric data is shown. Where the Figure 2.10. shows the plots of the descending orbit (left) and ascending orbit (right) of a pixel in the center of the swath with respect to the latitude: the red line refers to L1 FRA, the green line refers to when the Δ is eliminated, the blue line is when not correcting the Δ.

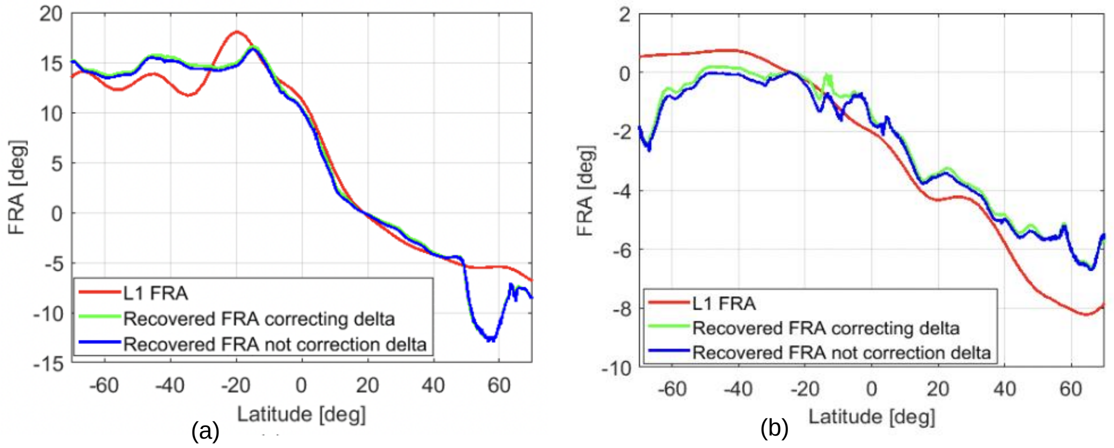

(a)

(b)

Figure 2.10. Plots of the FRA vs latitude of a pixel in the center of the swath of the: (a) descending orbit, (b) ascending orbit.

And then, the comparison of the retrieved VTEC from SMOS with other VTEC sources is shown. Figure 2.11. shows the plots of descending orbit (left) and ascending orbit (right) of a pixel in the center of the swath. Where the red line refers to the L1 VTEC, the green line refers to when the Δ is eliminated, the blue line when not correcting the Δ, the black line refers to the IGS VTEC, and the pink line to the A3TEC.

The IGS VTEC considers a higher total electron content, that is why is above the other sources. The recovered VTEC has less ripples, being smoother than the A3TEC [20].

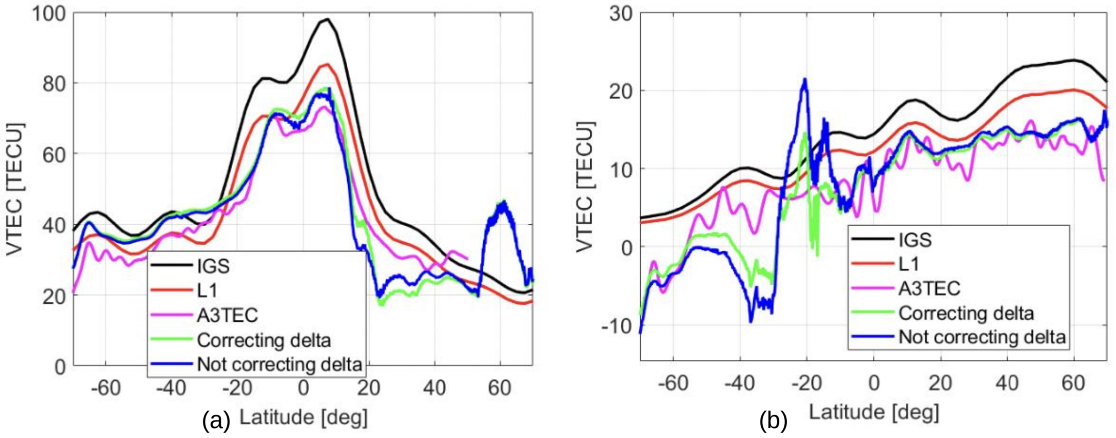

(a)

(b)

Figure 2.11. Comparison of the VTEC with different sources of: (a) descending orbit, (b) ascending orbit.

3. Methodology / project development:

Having explained the background and the basic knowledge to understand this project, which would correspond to the research stage at the beginning of the project, the following analysis has been carried out in order to improve the FRA and VTEC acquisition and the finding of more suitable noise thresholds to consider.

3.1. MIRAS Testing Software (MTS)

This software is an independent processor developed at the UPC to analyze and process SMOS data in near real time. It reads the raw data sent by MIRAS transmitter and it automatically computes a series of data products which includes the levels: L1A (calibrated visibilities), L1B (brightness temperature maps in the antenna frame) and L1C (geolocated brightness temperatures) [6].

It was important to become familiar with the software and to understand how it is structured so as to then be able to modify it as necessary. Having understood how the software is made with its respective functions and the procedures applied, the methodology used in order to analyze the ascending and descending orbits and to obtain the final results is going to be explained.

3.2. Analyzing the orbits for interferences

As mentioned before, there are two orbits that are going to be analyzed during all the project, a descending orbit (from March 2014) and an ascending orbit (from July 2014) both over the eastern Pacific Ocean.

The Brightness Temperature (TB) maps will be reproduced at the antenna frame, obtaining T_x, T_y, T_3, and T_4 in order to observe both orbits to see if any RFI are found. This is done by using the function *L1Bviewer* of the MTS software, which processes the input data of the L1B files of the orbits.

This function provides different ways of observing the TB, the plots shown here will be the average of the entire sequence of the swath of each TB. However, there is also an option to see the entire sequence of the TB, this was used to analyze them better.

In the plots of the descending orbit, Figure 3.1.a. and Figure 3.1.b., a red dot can be seen at the bottom of the plots. This dot was observed during the entire path of the orbit, so it can be concluded that this dot represents an alias of the sun. At the beginning it was thought to be an interference, but these are not constant along the entire path and would appear glowing in very bright red colors, which this dot has not done.

The same happens to the ascending orbit, Figure 3.2, but in a smaller extent.

3.2.1. Descending Orbits

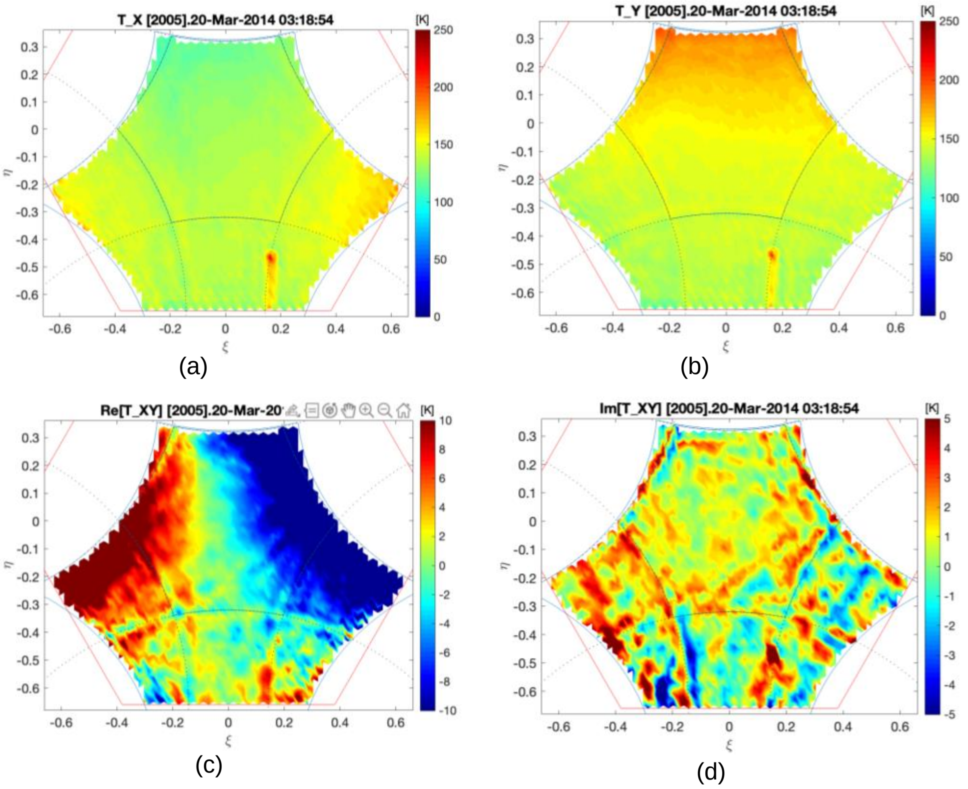

(a) (b)

(c) (d)

Figure 3.1. Maps of brightness temperature in the descending orbit: (a) Txx polarization, (b) Tyy polarization, (c)Txy polarization, (d) Tyx polarization.

3.2.2. Ascending Orbits

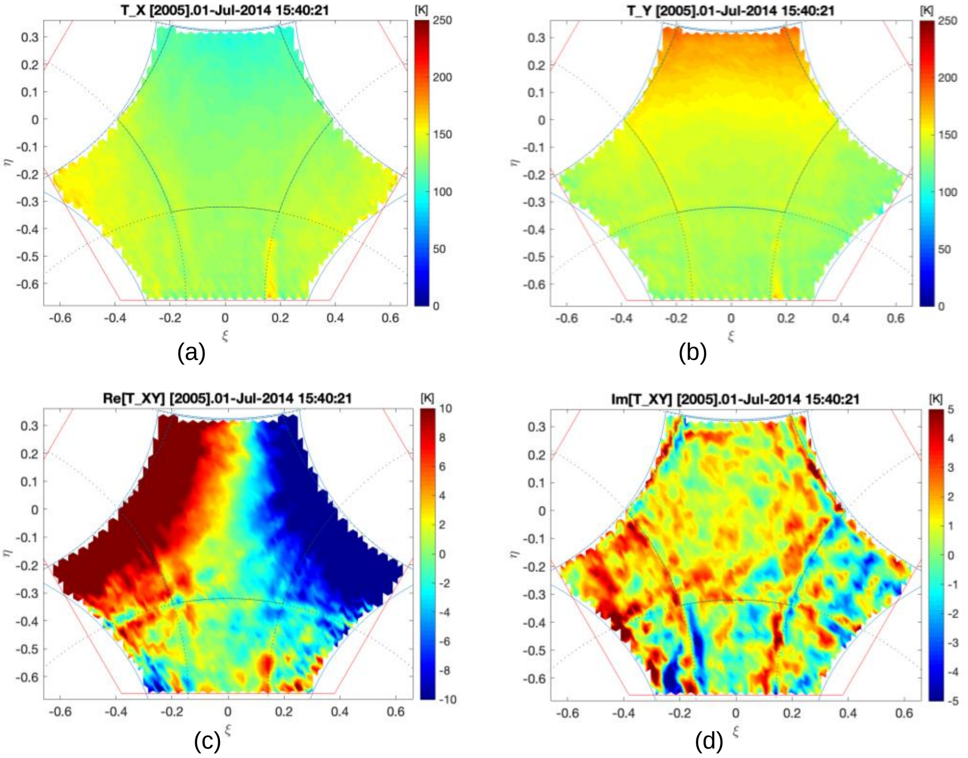

(a) (b)

(c) (d)

Figure 3.2. Maps of brightness temperatures in ascending orbit: (a) Txx polarization, (b) Tyy polarization, (c) Txy polarization, (d) Tyx polarization.

3.3. Singularities of FRA

Looking at the map of all the SMOS orbits, both descending and ascending, from March 1st to 9th of 2014, Figure 3.3, it can be noticed that there are particular zones where the recovery of the FRA is not possible due to the singularities of the FRA equation.

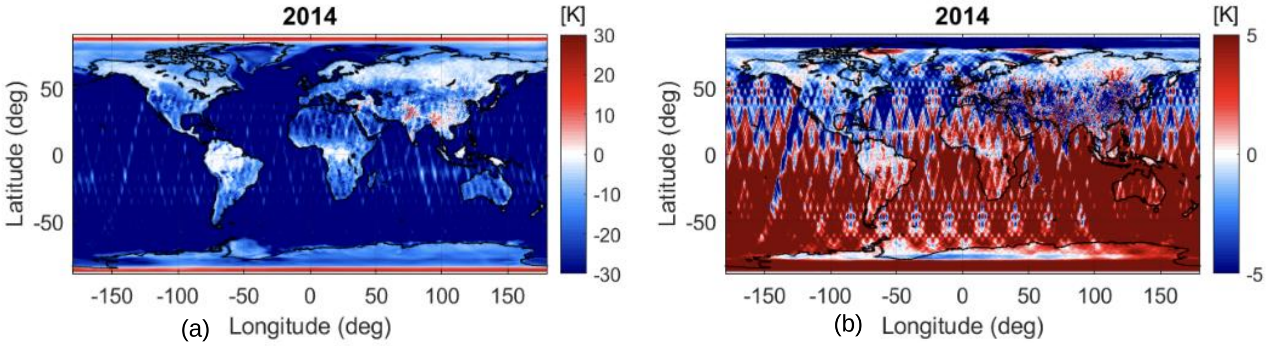

(a) (b)

Figure 3.3. TB maps of 9 consecutive days of March 2014: (a) Difference between T_B^{xx} and T_B^{yy}, (b) T3. [20].

These zones are in the Amazon, Russia, and Canada, which are dense forest zones (white zones shown in the map). The singularities of the FRA equation will be analyzed in order to determine what is happening in these particular zones and the reason why the FRA cannot be recovered.

3.3.1. Analysis of the FRA formula [3]

Using the Eq. (2.4), that is going to be shown again in Eq. (3.1) for an easier reading:

$$\begin{bmatrix} T_B^{xx} \\ 2\Re e(T_B^{xy}) \\ T_B^{yy} \end{bmatrix} = \begin{bmatrix} cos^2(\varphi+\Omega_f) & sin^2(\varphi+\Omega_f) \\ -sin2(\varphi+\Omega_f) & sin2(\varphi+\Omega_f) \\ sin^2(\varphi+\Omega_f) & cos^2(\varphi+\Omega_f) \end{bmatrix} \begin{bmatrix} T_B^{hh} \\ T_B^{vv} \end{bmatrix}$$

(3.1)

So, if the second row of the system is divided by the sum of the first and third rows, we obtain an equation used to calculate an instantaneous value of FRA for the entire FoV. For later be able to obtain the T_B^{hh} and T_B^{vv} rotation over ground, Eq. (2.6), mentioned again:

$$\Omega_f = -\varphi - \frac{1}{2}\arctan\left(\frac{2\Re e(T_B^{xy})}{T_B^{xx} - T_B^{yy}}\right)$$

(3.2)

This equation presents some singularities, two different cases can be identified:

1. If $T_B^{hh} = T_B^{vv}$ and $2\Re e\left(T_B^{xy}\right) = 0$ → Rewriting equations from Eq. (3.1)

$$T_B^{xx} = T_B^{hh} * [cos^2\left(\varphi+\Omega_f\right) + sin^2(\varphi+\Omega_f)] \rightarrow T_B^{xx} = T_B^{hh}$$

(3.3)

$$T_B^{yy} = T_B^{vv} * [\, sin^2\left(\varphi+\Omega_f\right) + cos^2\left(\varphi+\Omega_f\right)\,] \rightarrow T_B^{yy} = T_B^{vv}$$

(3.4)

$$2\Re e\left[T_B^{xy}\right] = 0$$

(3.5)

This causes $T_B^{xx} = T_B^{yy}$. If we go back to Eq. (3.2), the arctangent argument would be $\frac{0}{0}$ and this means that the FRA (Ω_f) cannot be recovered. However, T_B^{hh} and T_B^{vv} can be retrieved, since $T_B^{xx} = T_B^{hh}$ and $T_B^{yy} = T_B^{vv}$ despite the value of the Ω_f.

2. If $T_B^{xx} = T_B^{yy}$ → Equating equations 1 and 3 from Eq. (3.1) and working it out:

$$T_B^{hh} * \left[cos^2\left(\varphi + \Omega_f\right) - sin^2\left(\varphi + \Omega_f\right)\right] = T_B^{vv} * \left[cos^2\left(\varphi + \Omega_f\right) - sin^2\left(\varphi + \Omega_f\right)\right]$$

(3.6)

Two possible solutions:

2.1. If $cos^2\left(\varphi + \Omega_f\right) - sin^2\left(\varphi + \Omega_f\right) \neq 0$ → the term in the expression cancels out, and case 1 applies.

2.2. If $cos^2\left(\varphi + \Omega_f\right) - sin^2\left(\varphi + \Omega_f\right) = 0$ → the term cannot be cancelled out. So, $cos^2\left(\varphi + \Omega_f\right) = sin^2\left(\varphi + \Omega_f\right)$, which means that $\varphi + \Omega_f = \pm\frac{\pi}{4}$. Working out equations 1, 2, and 3 from Eq. (3.1), it is obtained:

$$T_B^{xx} = \frac{1}{2} * \left(T_B^{hh} + T_B^{vv}\right)$$

(3.7)

$$T_B^{yy} = \frac{1}{2} * \left(T_B^{hh} + T_B^{vv}\right)$$

(3.8)

$$2\Re e\left[T_B^{xy}\right] = \left(T_B^{hh} - T_B^{vv}\right) * sin2\left(\varphi + \Omega_f\right) = \left(T_B^{hh} - T_B^{vv}\right)$$

(3.9)

Multiplying Eq. (3.7) by 2 and adding to it Eq. (3.9), and the same for Eq.(3.8):

$$T_B^{vv} = T_B^{xx} + \frac{1}{2} 2\Re e\left[T_B^{xy}\right]$$

(3.10)

$$T_B^{vv} = T_B^{xx} + \frac{1}{2} 2\Re e\left[T_B^{xy}\right]$$

(3.11)

Therefore, both T_B^{hh} and T_B^{vv} can be calculated (as they are different) from T_B^{xx} and T_B^{yy}.

So, in this case it would be $\frac{something}{0}$, and the FRA could be recovered.

3.3.2. Canada

The Canada zone is the one that will be studied in more detail. To do so, the maps of the brightness temperatures at antenna frame ($T_B^{xx} - T_B^{yy}$ and T_3) and at ground frame ($T_B^{hh} - T_B^{vv}$ and T_3) will be reproduced using the function *L1Claunch* of the MTS software, which processes the input data of the L1B files of the orbits. The objective is to analyze these maps in order to see if the FRA can or cannot be recovered, and also at which case of the formula analyzed above this zone corresponds.

3.3.2.1. Descending orbits

First, the maps of the descending orbit were reproduced. As the focus is where the orbit passes through Canada, all the maps will be zoomed in that zone to be able to see them better. The complete graphs will be shown in the appendix section A.A.1.

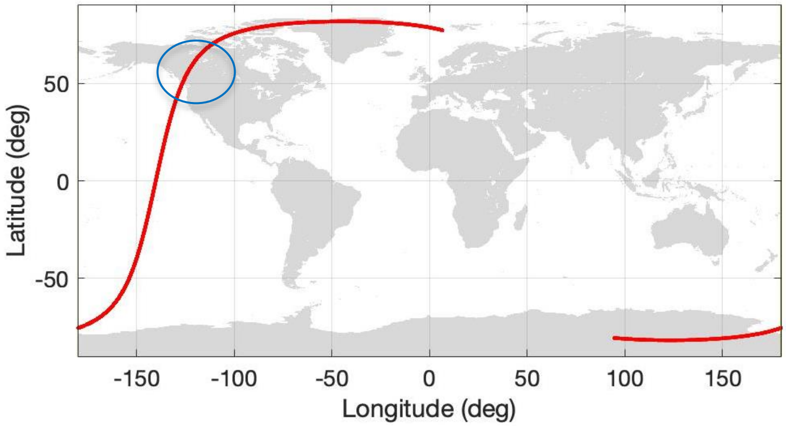

Figure 3.4. Descending orbit, March 2014.

The purpose of reproducing these maps is to see if $T_B^{xx} = T_B^{yy}$ or if $T_B^{hh} = T_B^{vv}$ in order to then calculate the FRA. In other words, to see if in this zone the Eq. (3.2) is in case 1 (having a $\frac{0}{0}$) or in the case 2.2 (having $\frac{something}{0}$).

3.3.2.1.1. Antenna Frame

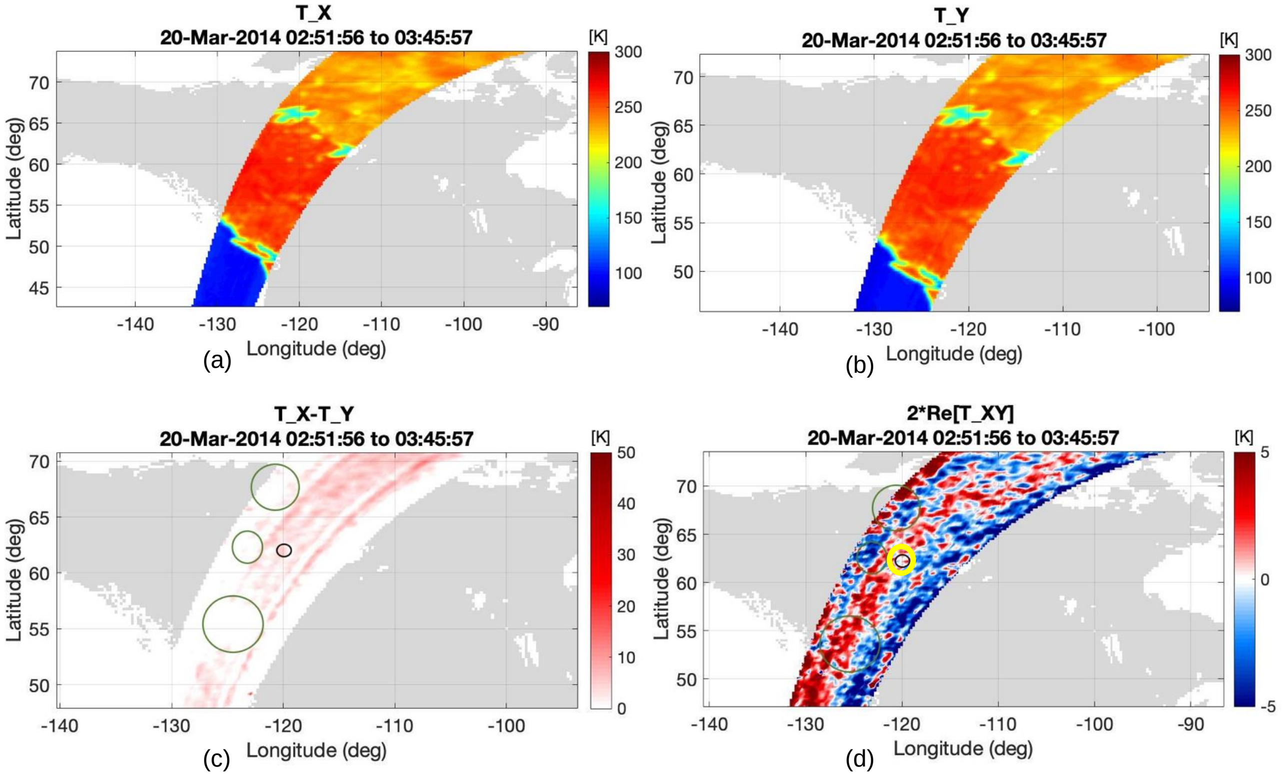

Figure 3.5. Zoomed maps at Antenna Frame of: (a) T_B^{xx}, (b) T_B^{yy}, (c) Difference between T_B^{xx} and T_B^{yy}, (d) T_3.

The areas where the brightness temperatures are found to be zero are marked with a circle, since that is where the singularities occur. In each figure the scale must be taken into account. The result of the analysis of these maps will be presented in the results section 4.1.1.

3.3.2.1.2. Ground Frame

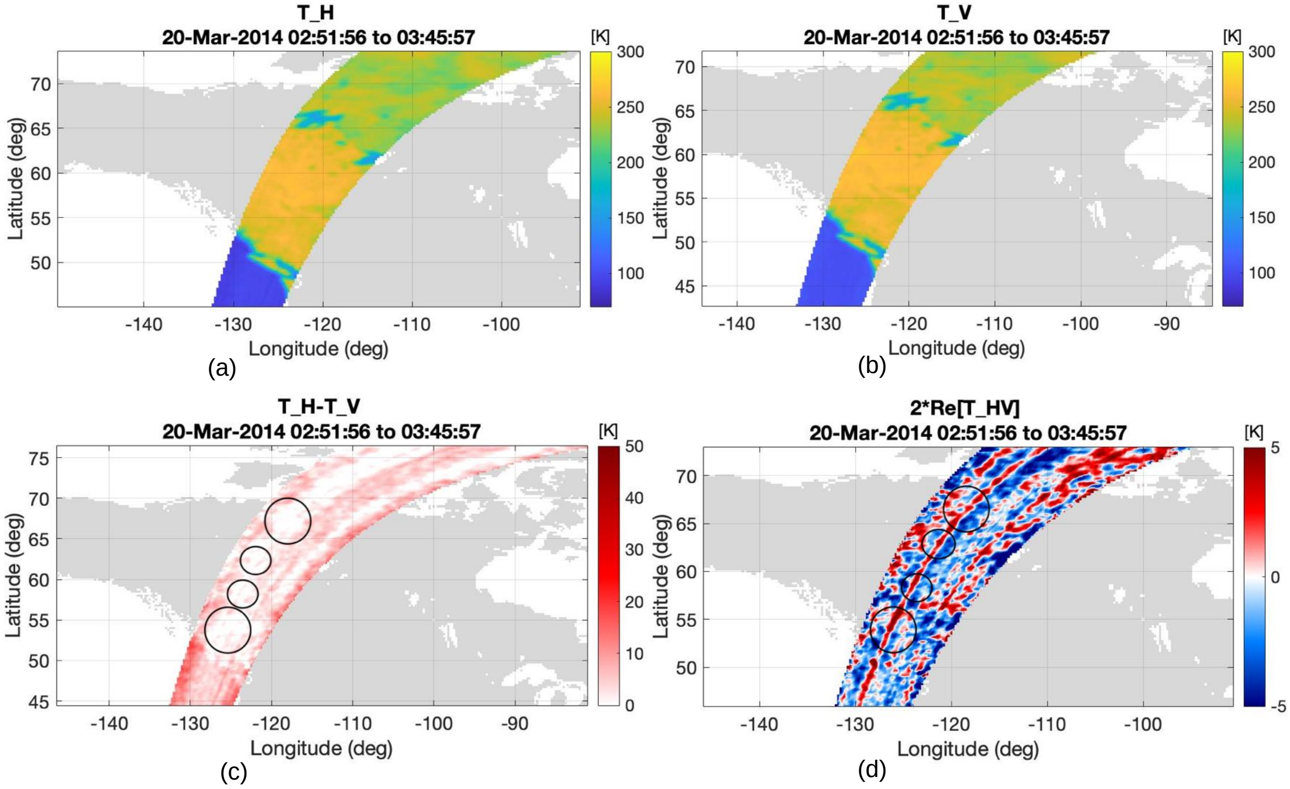

Figure 3.6. Zoomed maps at Ground Frame of: (a) T_B^{hh}, (b) T_B^{vv}, (c) Difference between T_B^{hh} and T_B^{vv}, (d)T_3.

The areas where the brightness temperatures are found to be zero are marked with a circle, since that is where the singularities occur. In each figure the scale must be considered. The result of the analysis of these maps will be presented in the results section 4.1.2.

3.3.2.2. Ascending Orbits

The maps of the brightness temperatures of the ascending orbit were also reproduced, even though the orbit does not pass-through Canada. These maps of the brightness temperatures in antenna and ground frame are going to be shown in the appendix section A.A.2.

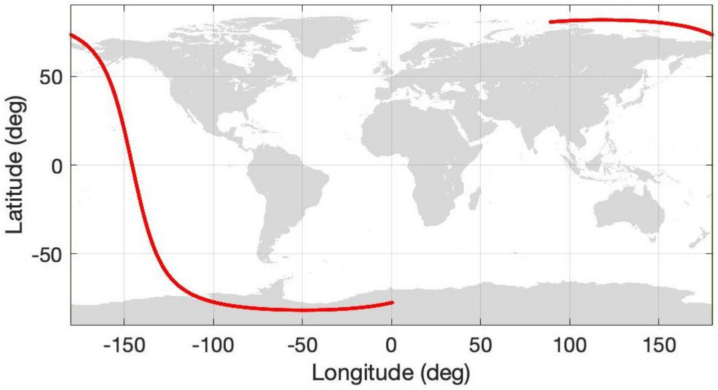

Figure 3.7. Ascending orbit, March 2014.

3.4. Improving the Recovered VTEC

As mentioned before, VTEC cannot have negative values. As it can be seen in Figure 2.9.a. and Figure 2.9.b. (repeated here as Figure 3.8) there are values that have been rejected when plotting them on the map, since they correspond to VTEC values that have not been correctly recovered. There are much more pixels rejected in ascending orbits than descending orbits, as previously mentioned, due to the effect of noise and its small range of VTEC variability.

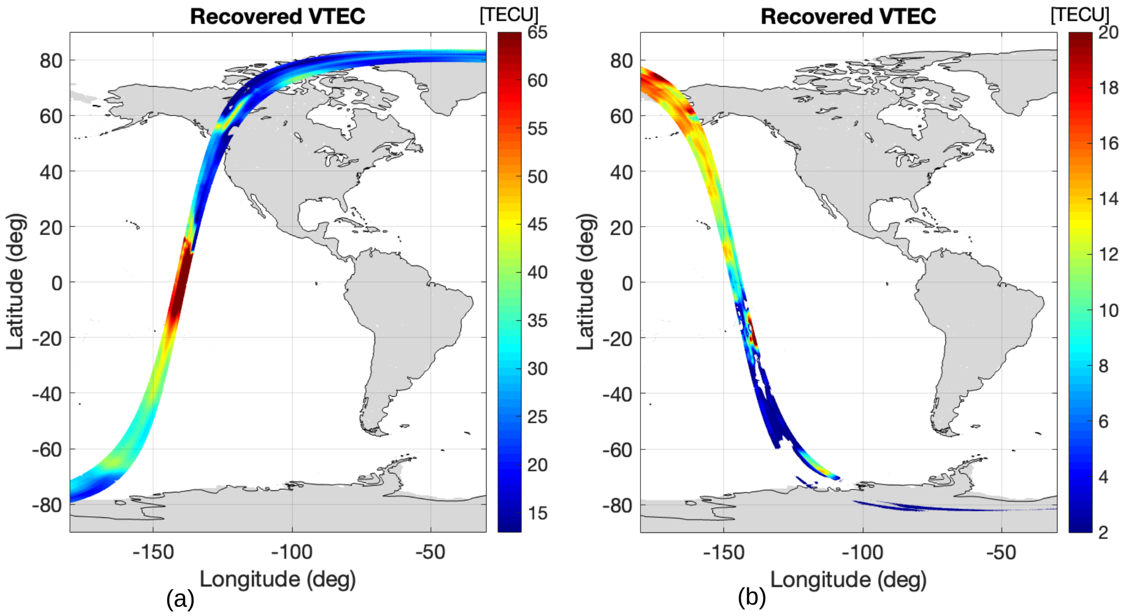

Figure 3.8. Recovered VTEC snapshoots of the methodology: (a) Descending orbit, (b) Ascending orbit. [20].

The aim is to modify the above-mentioned methodology (in section 2.3.2.1) in order to improve the recovered VTEC to avoid negative values as they do not make any sense, observing that the ascending orbit is the most damaged one. This is going to be done by modifying the functions *FRA_processor* and *fra_calc2* in the MTS software.

The problem is that at some point during the calculation, the VTEC comes out with negative values. Several approaches were applied until the results wanted were achieved:

3.4.1. Changing the order of the core Methodology

The first approach was to change the order of some steps of the methodology. Instead of first removing the pixels with a $|\cos \Theta_B| < 0.05$ over TB snapshots (step 1), the temporal filter is applied with a window size of 43 snapshots (step 2), and for later when calculating the VTEC (step 6) with the Eq. (3.12) removing the pixels with $|\cos \Theta_B| < 0.05$ over the VTEC snapshots. Eq. (3.12) is mentioned here again to have an easier reading:

$$VTEC = \frac{f^2 \, \Omega_f \cos\theta}{1.355 * 10^4 \, B_0 \cos\Theta_B} \tag{3.12}$$

This was done by modifying the function *FRA_processor* in the MTS software. This modified methodology would be structured as:

1. Applying a temporal filter with a window size of 43 TB snapshots.

2. The calculus of the measured FRA is done by using Eq. (3.2).

3. In order to avoid the indetermination of Eq. (3.2), pixels with an incidence angle lower than 25º are rejected.

4. The error Δ is subtracted to Ω_f^m to obtain the actual FRA.

5. The calculus of the VTEC is done by using Eq. (3.12).

6. The spatial filter is applied with a radius of 0.189 over the VTEC snapshots.

7. Pixels with $|\cos\Theta_B| < 0.05$ over VTEC snapshots are rejected to avoid the indetermination of Eq. (3.12).

8. The VTEC AF-FoV value is extended to the EAF-FoV.

9. The geolocation is done over an ETOPO-5 grid (resolution of 5 minutes of latitude and longitude), at 450 km of altitude. The measurements acquired at the same point on the grid are averaged.

At the beginning, it was thought that by rejecting first the pixels with $|\cos\Theta_B| < 0.05$ over TB snapshots, some values that could have an influence in the final result were left out simply because the cosine gives a value of 0. Therefore, by applying first the temporal filter, it would consider all the values of the TB snapshots to then reject the pixels with a $|\cos\Theta_B| < 0.05$ over the VTEC snapshots.

The descending orbits were the starting point since they are the least affected, so applying this new method the result should be the same as before or with a slight improvement. Then the ascending orbits were reproduced, they were expected to have an important improvement. Here are shown only the ones of interest, the rest will be shown and analyzed in the results section 4.2.1.

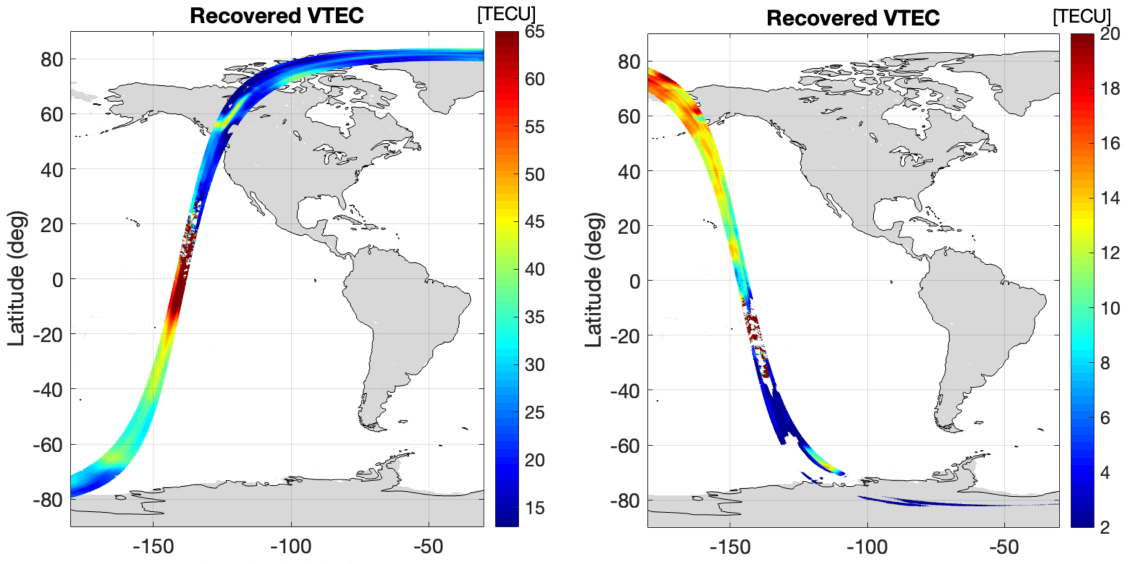

(a) (b)

Figure 3.9. Recovered VTEC snapshoots applying the first approach: (a) descending orbit, (b) ascending orbit.

3.4.2. Reproducing CosthB

The $\cos\Theta_B$ plots were reproduced with the aim of knowing when its value was 0, and its sign at each moment of the swath. This was done without modifying the methodology.

It can be seen that the sign of the cosine is positive at the upper part and negative at the bottom. This happens due to the geomagnetic equator.

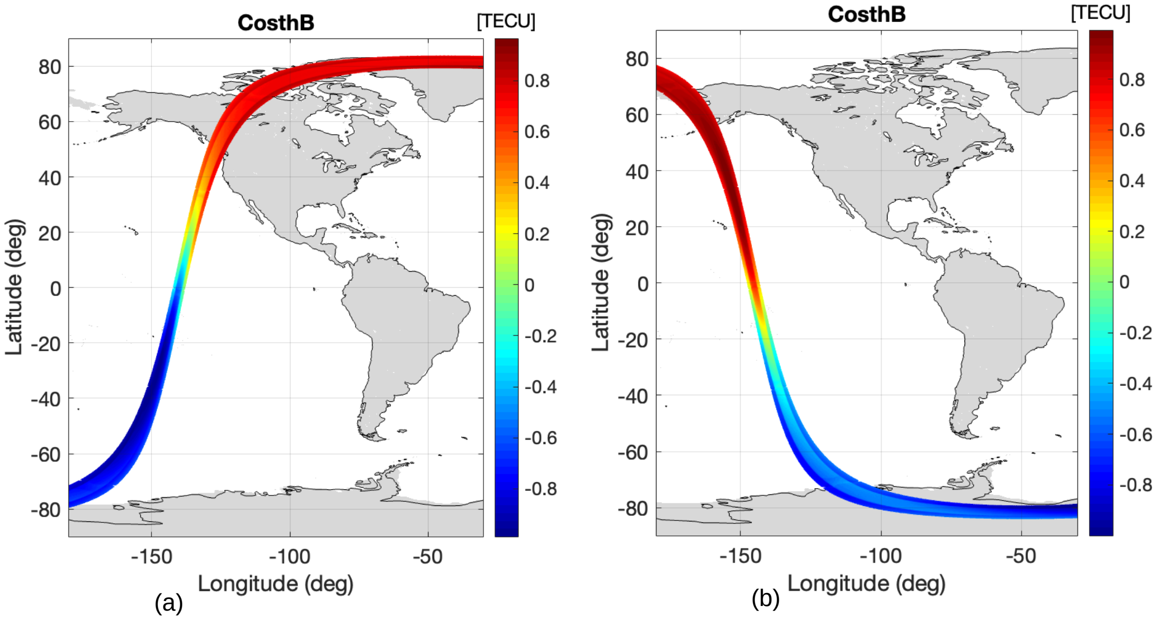

Figure 3.10. Snapshoots of the $\cos\Theta_B$: (a) Descending orbits, (b) Ascending orbits.

3.4.3. Forcing the sign of the FRA and the CosthB to be equal

The second approach, instead of changing the order of the steps of the methodology, was to analyze more deeply how the VTEC and FRA are calculated. The VTEC is calculated from the Eq. (3.12) where the two main parameters are the FRA and $\cos\Theta_B$. In the Eq. (3.12) can be noticed that the FRA is in the numerator and the $\cos\Theta_B$ in the denominator, to simplify the explanation a bit the equation can be shown with only the mentioned parameters:

$$VTEC = \frac{\Omega_f \ldots}{\cos\Theta_B \ldots} \tag{3.13}$$

As known, the VTEC must always be positive, for this to happen, the sign of the FRA and the cosine must be equal. What may be happening is that the FRA has some noise, and as a value is very close to 0, the noise causes it to change its sign. Making the FRA and the cosine different in sign, leading to a negative value of VTEC.

All the verifications were done by modifying the function *fra_calc2* of the MTS software. This function calculates the four possible solutions of the FRA and keeps the minimum one. It was forced to return not only the minimum solution but also the one that has the same sign as the $\cos\Theta_B$. For this reason, all the solutions that do not have the same sign as the cosine are rejected and then the minimum solution is chosen. This would correspond to a modification in the step 3 of the core methodology (section 2.3.2.1).

The plots for descending and ascending orbits were reproduced but are going to be analyzed at the results section 4.2.2.

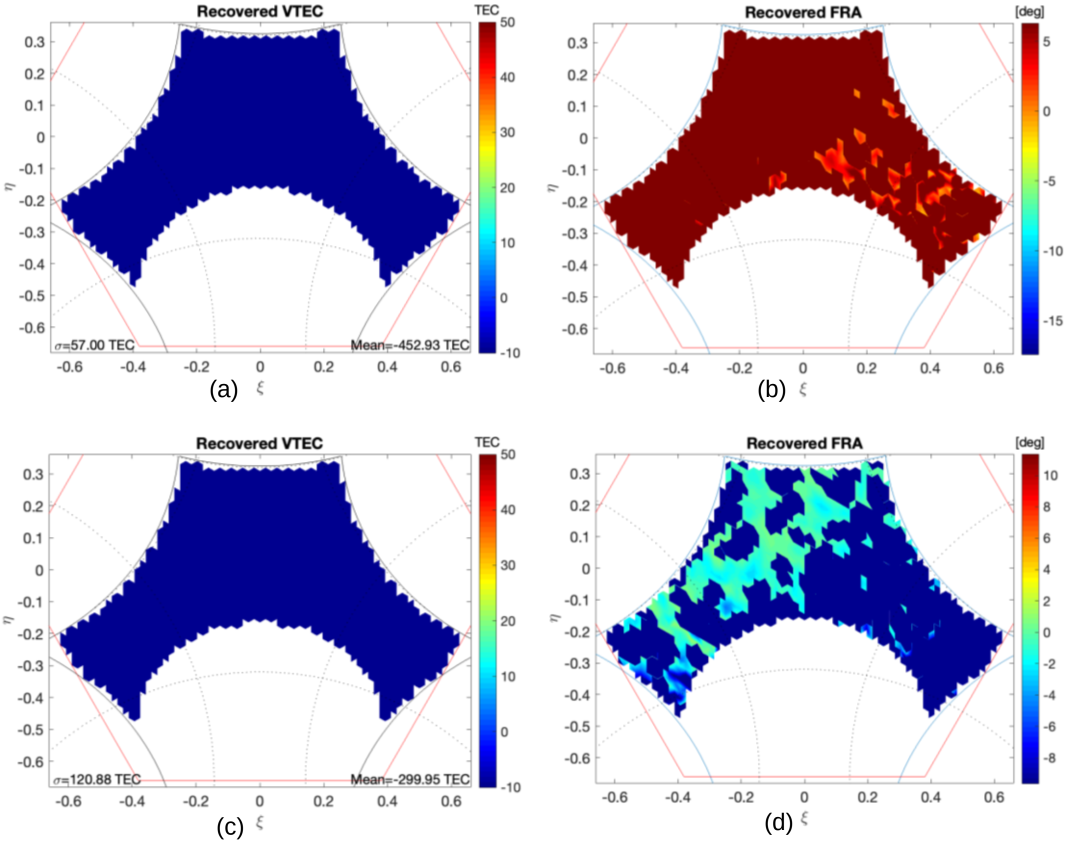

(a) (b) (c) (d)

Figure 3.11. Snapshoots of the second approach: TOP: Descending orbits of (a) recovered VTEC, (b) recovered FRA, BOTTOM: ascending orbits of (c) recovered VTEC, (d) recovered FRA.

3.4.4. Rejecting the negative VTEC values directly

The last approach was to directly reject the negative values of the VTEC right after calculating it with Eq. (3.12) and before applying the spatial filter. This way the negative values of the VTEC would have been taken out before averaging. So, at the moment of applying the spatial filter it would be considering more positive values of VTEC. This was done by modifying the function *FRA_processor* in the MTS software, corresponding to adding a step in the core methodology, the step 7. Now structured as:

1. Rejecting pixels with $|\cos\Theta_B| < 0.05$ over the TB snapshots to avoid the indetermination of Eq. (3.12).

2. Applying a temporal filter with a window size of 43 TB snapshots.

3. The calculus of the measured FRA is done by using Eq. (3.2).

4. In order to avoid the indetermination of Eq. (3.2), pixels with an incidence angle lower than 25º are rejected.

5. The error Δ is subtracted to Ω_f^m to obtain the actual FRA.

6. The calculus of the VTEC is done by using Eq. (3.12).
7. Reject the negative values of the VTEC.
8. The spatial filter is applied with a radius of 0.189 over the VTEC snapshots.
9. The VTEC AF-FoV value is extended to the EAF-FoV.
10. The geolocation is done over an ETOPO-5 grid (resolution of 5 minutes of latitude and longitude), at 450 km of altitude. The measurements acquired at the same point on the grid are averaged.

The descending and ascending orbits are going to be shown, but here are shown only the ones of interest, the rest will be shown and analyzed in the results section 4.2.3.

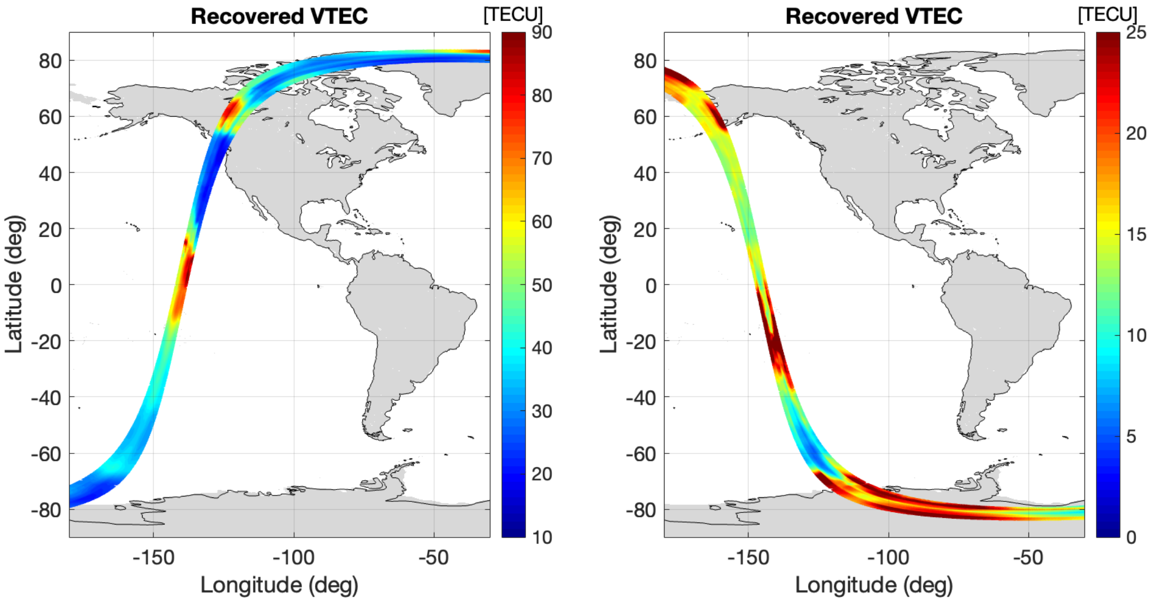

(a) (b)

Figure 3.12. Recovered VTEC snapshoots applying the third approach: (a) descending orbits, (b) ascending orbits.

3.5. Thresholds

The thresholds used in the core methodology were obtained from the simulator. In this section the thresholds will be tested one by one with real SMOS radiometric data, in order to find the optimal value for each one of them. The purpose is to improve the error acquisition of the FRA and the VTEC by finding the most suitable thresholds in each case.

First, the thresholds of the core methodology are going to be analyzed in order to find the most suitable one to improve the statistics. Then, the same will be done but applying the third approach.

The thresholds to analyze are:

- **Threshold1**: this threshold is used in the calculation of the FRA using the Eq. (3.2), calculated with the function *fra_calc2* in the MTS software. The calculus of the FRA has 4 possible solutions (the typical solution, the one where the value of $T_B^{xx} - T_B^{yy}$ is small, the one where the value of T_3 is small, and the one where both values are small). This Threshold1 is used when the value of $T_B^{xx} - T_B^{yy}$ (the denominator) is small.

- **Threshold2**: this threshold is also used in the calculation of the FRA using the Eq. (3.2), calculated with the function *fra_calc2* in the MTS software. The calculus of the FRA has 4 possible solutions (the typical solution, the one where the value of $T_B^{xx} - T_B^{yy}$ is small, the one where the value of T_3 is small, and the one where both values are small). This Threshold2 is used when the value of T_3 (the numerator) is small.

- **Size of the Temporal filter**: this threshold is used when applying the temporal filter over the TB snapshoots, used in the function *FRA_processor* in the MTS software. The temporal filter consists of an averaging triangular window that considers the current snapshoot with the highest weight. This threshold is the number of snapshoots that corresponds to the temporal window size used.

- **Size of the Spatial filter**: this threshold is used when applying the spatial filter over the VTEC snapshoots at antenna frame, used in the function *FRA_processor* in the MTS software. This threshold consists of the size of the radius applied.

- **Incidence angle**: this threshold is used in order to avoid an indetermination of the Eq. (3.2), by rejecting pixels with a low incidence angle since they are the most affected part of the snapshoot, used in the function *FRA_processor* in the MTS software. This indetermination happens when both numerator and denominator tend to 0, $T_B^{xx} \approx T_B^{yy}$ and $T_3 \approx 0$. This threshold consists of low angles of incidence.

3.5.1. Core Methodology

The core methodology uses the following thresholds:

Table 3.1. Values of the original thresholds used.

Threshold1	Threshold2	Size Temporal Filter	Size Spatial Filter	Incidence Angle
4	0.9	43	0.189	25º

3.5.1.1. New Thresholds

The thresholds will be tested one by one for descending and ascending orbits, in order to find the optimal value for each one of them. The same values were tested for the two orbits and the following values were tested for each of the thresholds:

- **Threshold1**: 2, 3, and 5 (Kelvin).
- **Threshold2**: 0.5, 0.8, 1, and 1.3 (Kelvin).
- **Size Temporal Filter**: 41 and 45 (snapshoots).
- **Size Spatial Filter**: 0.18, 0,195, 0.2, and 0.25 (d/λ).
- **Incidence Angle**: 23º and 24º (degrees).

Table 3.2. Values of the Thresholds for the Core Methodology.

Threshold1			Threshold2				Size Temporal Filter		Size Spatial Filter				Incidence Angle	
4			0.9				43		0.189				25	
2	3	5	0.5	0.8	1	1.3	41	45	0.18	0.195	0.2	0.25	23	24

All the plots obtained will be shown in the appendix section B.1.1, and the analysis of which one has been the most optimal in the results section 4.3.1.

3.5.2. Applying the Third Approach

This approach was reproduced with the same values as the core methodology, Table 3.1.

First, the plots were reproduced with the same new thresholds chosen above, but it was realized that perhaps more optimal values could be found by repeating the same procedure as before. The thresholds will be tested one by one for descending and ascending orbits, in order to find the optimal value for each one of them. The same values were tested for the two orbits and the following values were tested for each of the thresholds:

- **Threshold1**: 2, 3, and 5 (Kelvin).
- **Threshold2**: 0.5, 0.8, 1, and 1.3 (Kelvin).
- **Size Temporal Filter**: 41 and 45 (snapshoots).
- **Size Spatial Filter**: 0.175, 0.18, 0,195, and 0.2 (d/λ).
- **Incidence Angle**: 23º and 24º (degrees).

Table 3.3. Values of the Thresholds for the Third Approach.

Threshold1			Threshold2				Size Temporal Filter		Size Spatial Filter				Incidence Angle	
4			0.9				43		0.189				25	
2	3	5	0.5	0.8	1	1.3	41	45	0.175	0.18	0.195	0.2	23	24

All the plots obtained will be shown in the appendix section B.B.2, and the analysis of which one has been the most optimal in the results section 4.3.2.2.

4. Results

In the previous section we have tested and analyzed several things, the three most important results are: the FRA retrieval in the zone of Canada, the explanation of three approaches in order to find the improvement of the recovered VTEC, and the thresholds found to improve the statistics.

4.1. Canada FRA retrieval

The Eq. (3.2) of the FRA is going to be shown again as Eq. (4.1) in order to have an easier reading:

$$\Omega_f = -\varphi - \frac{1}{2}\arctan\left(\frac{2\Re e(T_B^{xy})}{T_B^{xx} - T_B^{yy}}\right) \tag{ 4.1}$$

4.1.1. Antenna Frame

The Figure 3.5.c. and Figure 3.5.d. are going to be shown again in order to make the analysis of the results easier.

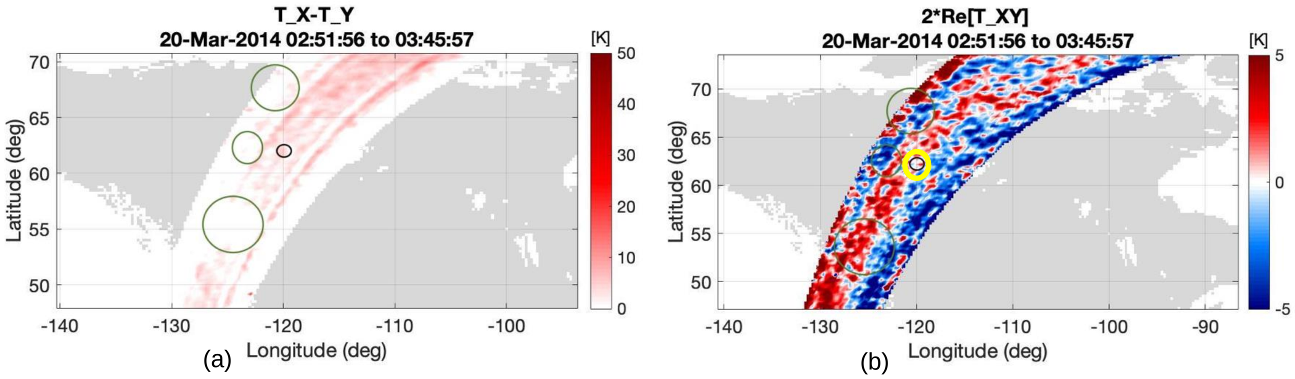

(a) (b)

Figure 4.1. Zoomed maps of descending orbits at antenna frame: (a) Difference between T_B^{xx} and T_B^{yy}, (b) T_3.

The Figure 4.1.a. corresponds to $T_B^{xx} - T_B^{yy}$ which is the value of the denominator of the arctangent of the FRA (Eq. (4.1)). In this case, it is useful to see when the T_B^{xx} is equal to T_B^{yy}, so the values that tend to 0 K can be identified, corresponding to a singularity.

The Figure 4.1.b. corresponds to T_3 which is the value of the numerator of the arctangent of the FRA (Eq. (4.1)). It can be observed that the white areas tend to 0 K in this zone, even though there are not as many white areas as in Figure 4.1.b., it must be considered that the scale is very low (going from -5 K to 5 K). So, these values can be 0 or very close to 0 due to the presence of signal noise.

Therefore, it can be considered that $T_B^{xx} = T_B^{yy}$. To see if the FRA can or cannot be recovered, the ground frame must be analyzed as well.

4.1.2. Ground Frame

Figure 3.6.c. and Figure 3.6.d. are going to be shown again in order to make the analysis of the results easier.

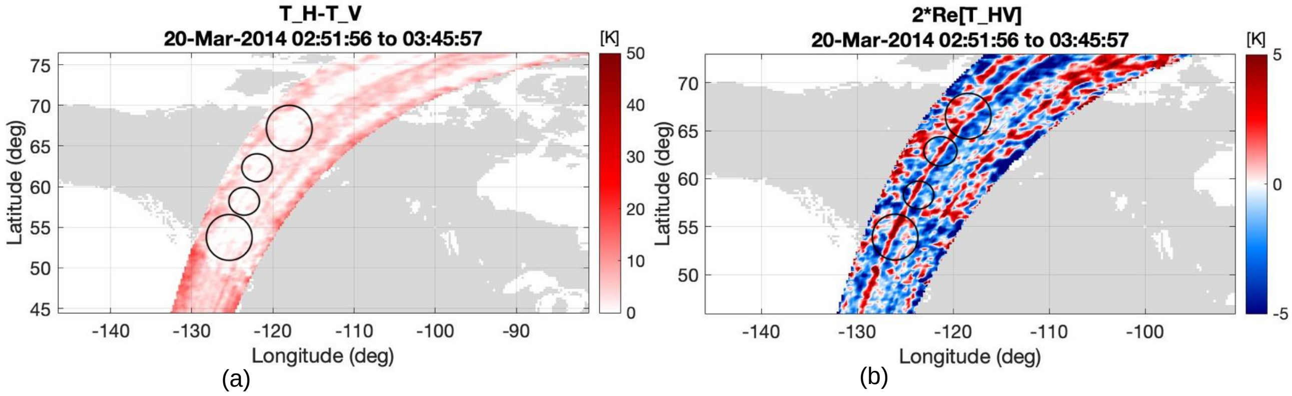

(a) (b)

Figure 4.2. Zoomed maps of descending orbits at ground frame: (a) Difference between T_B^{hh} and T_B^{vv}, (b) T3.

Similar to the previous figure, the Figure 4.2.a. and Figure 4.2.b. corresponds to $T_B^{hh} - T_B^{vv}$ and to T_3 respectively.

In the first one, the values that tend to 0 K are easier to identify. While in the second one happens the same as in the antenna frame, in which the scale is very low, so these values can be 0 or very close to 0 due to the presence of signal noise.

Therefore, it can be considered that $T_B^{hh} = T_B^{vv}$.

4.1.3. Summary

To sum up, this zone of Canada ends up having $T_B^{xx} = T_B^{yy}$, $T_B^{hh} = T_B^{vv}$, and $T_3 = 0$, which corresponds to case 1 of the analysis of the FRA. This means that the FRA (Ω_f) cannot be recovered. However, T_B^{hh} and T_B^{vv} can be retrieved, since $T_B^{xx} = T_B^{hh}$ and $T_B^{yy} = T_B^{vv}$ despite the value of the Ω_f.

4.2. Different approaches to improve the recovered VTEC

The results of the three different approaches will be analysed to conclude whether the expected results were achieved.

4.2.1. First Approach: Changing the order of the core methodology

Figure 2.9 and Figure 3.9 are going to be shown again in order to make the analysis of the results easier. Also, the Figures of the differences between the recovered VTEC and the L1 VTEC are going to be shown.

The results were expected to be better than the ones obtained with the core methodology. In the descending orbits, by obtaining the same results or even getting a slight improvement, and in ascending orbits by obtaining an important improvement.

First, the plots of the methodology (from section 2.3.2.1) and those obtained by applying the first approach of the descending orbits are going to be shown, to compare them. And then the plots of the ascending orbit.

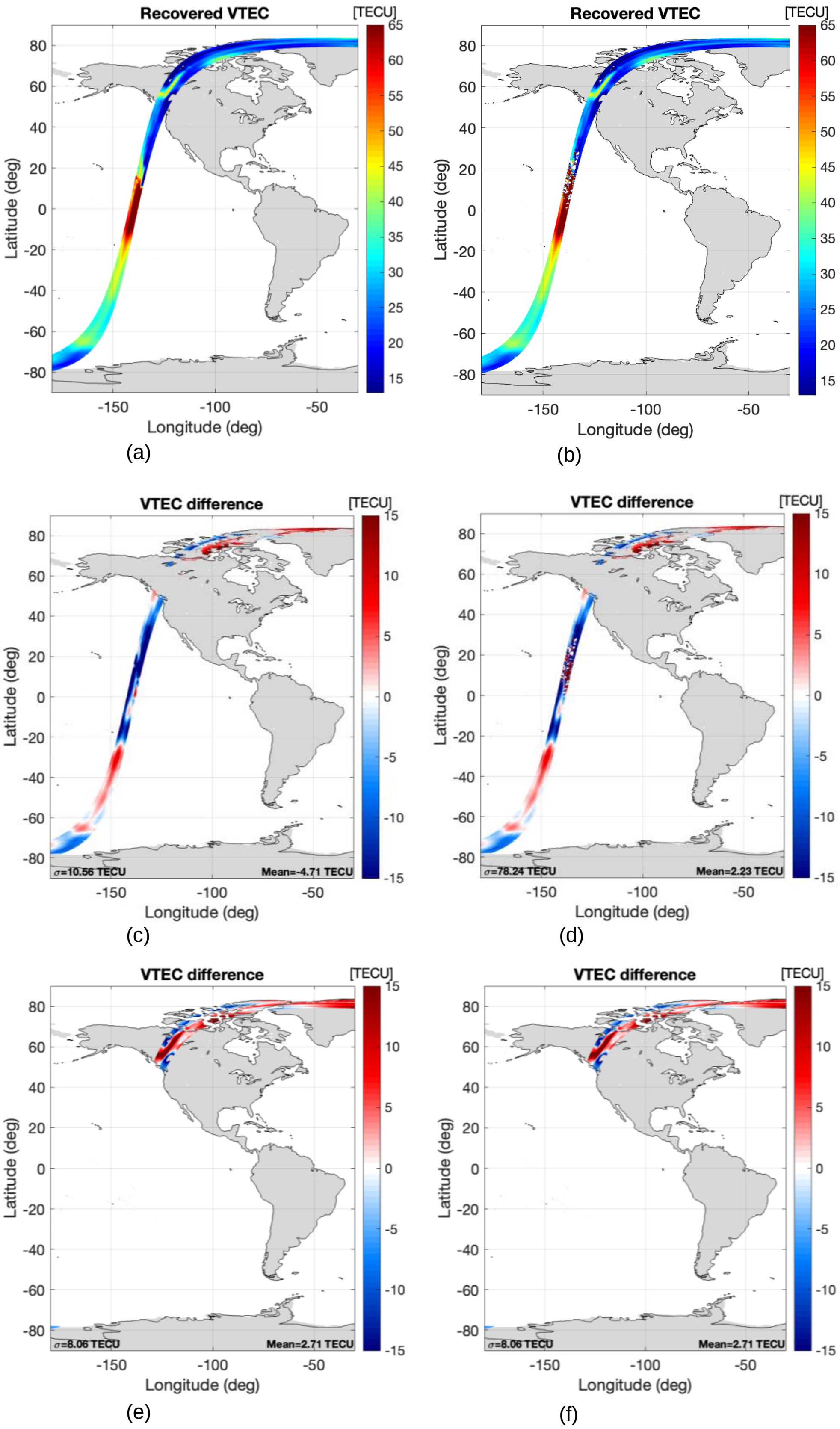

(a) (b)

(c) (d)

(e) (f)

Figure 4.3. Maps of VTEC of the ***descending*** *orbit:* *TOP**: Recovered VTEC (a) of the core methodology, (b) applying the first approach.* *MIDDLE**: Difference between recovered VTEC and L1 VTEC over* ***ocean*** *(c) of the core methodology, (d) applying the first approach.* *BOTTOM**: Difference between recovered VTEC and L1 VTEC over* ***land*** *(e) of the core methodology, (f) applying the first approach.*

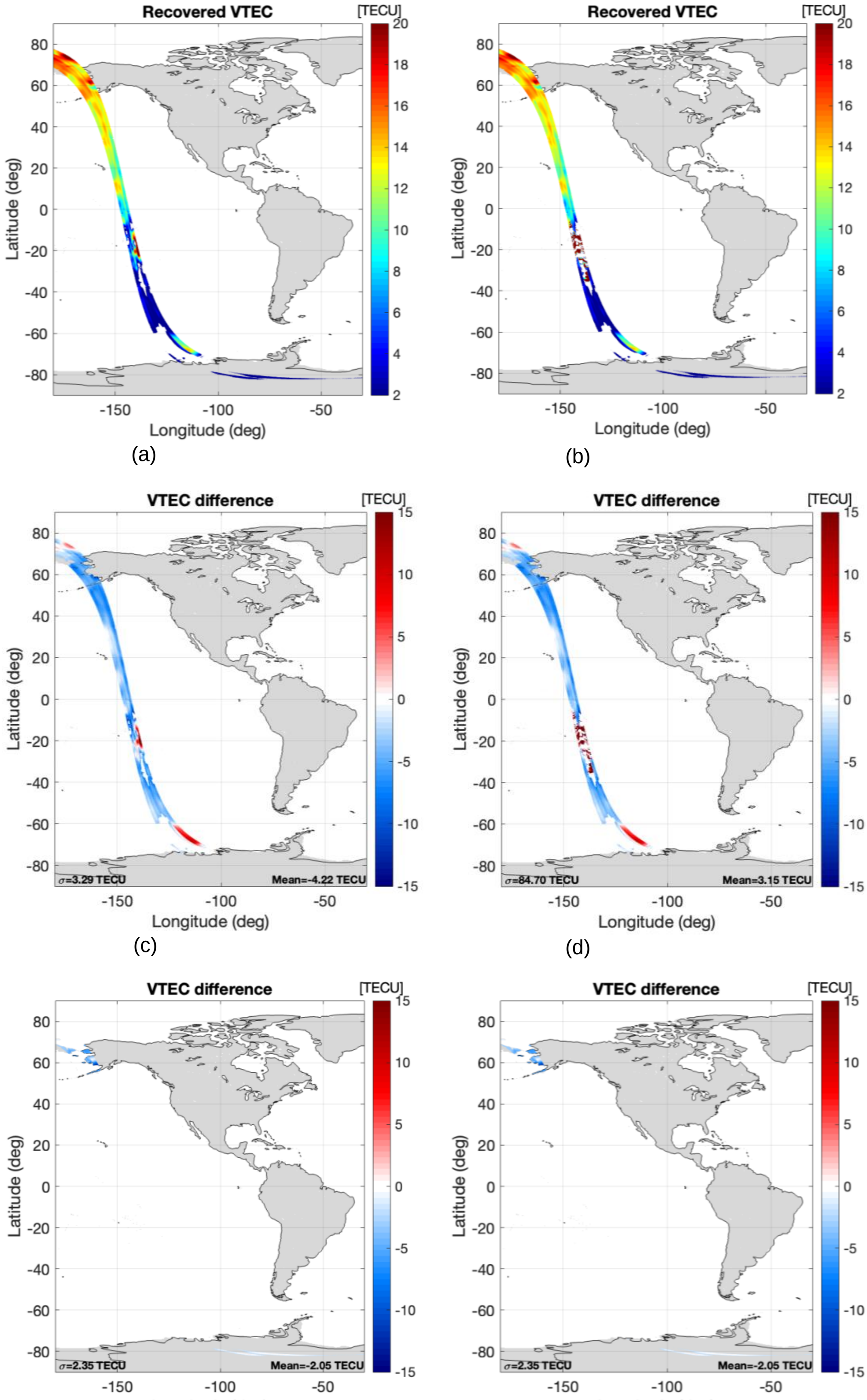

(a) (b) (c) (d) (e) (f)

Figure 4.4. Maps of VTEC of the ***ascending*** *orbit:* *TOP: Recovered VTEC (a) of the core methodology, (b) applying the first approach. MIDDLE: Difference between recovered VTEC and L1 VTEC over* ***ocean*** *(c) of the core methodology, (d) applying the first approach. BOTTOM: Difference between recovered VTEC and L1 VTEC over* ***land*** *(e) of the core methodology, (f) applying the first approach.*

As we can see, the plots have gotten worse, not only the maps but also the statistics. This may be due to the fact that if the pixels with $|\cos\Theta_B| < 0.05$ over TB snapshoots are not rejected at the moment of applying the temporal filter, it may be considering values that are not right from the beginning. That is, these pixels are rejected to avoid an indetermination of Eq. (3.12) when the geomagnetic field is orthogonal to the direction of the wave propagation, $\cos\Theta_B \approx 0$, (repeated here as Eq. (4.2) to make the reading easier):

$$VTEC = \frac{f^2\, \Omega_f \cos\theta}{1.355 * 10^4\, B_0 \cos\Theta_B} \tag{ 4.2}$$

So, at these values, the FRA would also be 0, since the cosine is multiplying in the numerator, the FRA (repeated here):

$$\Omega_f = 1.355 * 10^4\, f^{-2} B_0 \cos\Theta_B \sec\theta\ VTEC \tag{ 4.3}$$

If the FRA ≈ 0, it cannot be recovered. Therefore, if the pixels with a $|\cos\Theta_B| < 0.05$ are not rejected at the beginning, these values of the FRA that cannot be recovered would be considered, obtaining more negative values of VTEC leading to a worse result.

Comparing the statistics of the plots with the core methodology and those where the first approach was applied, it can be seen that the STD (standard derivation) has significantly gotten worse, both in descending and ascending orbits, especially in the ocean. The STD goes from 10.56 TECU (in Figure 4.3.c.) to 78.24 TECU (in Figure 4.3.d.) over ocean of the descending orbits, and in the ascending orbits the STD goes from 3.29 TECU (in Figure 4.4.c.) to 84.70 TECU (Figure 4.4.d.) over ocean.

It has been concluded that this modified methodology does not work.

4.2.2. Second Approach: Forcing the sign of the FRA and the CosthB to be equal

Figure 3.11 is going to be shown again in order to make the analysis of the results easier. First, the plots of the methodology (from section 2.3.2.1) and those obtained by applying the second approach of the descending orbits are going to be shown, to compare them. And then the plots of the ascending orbit.

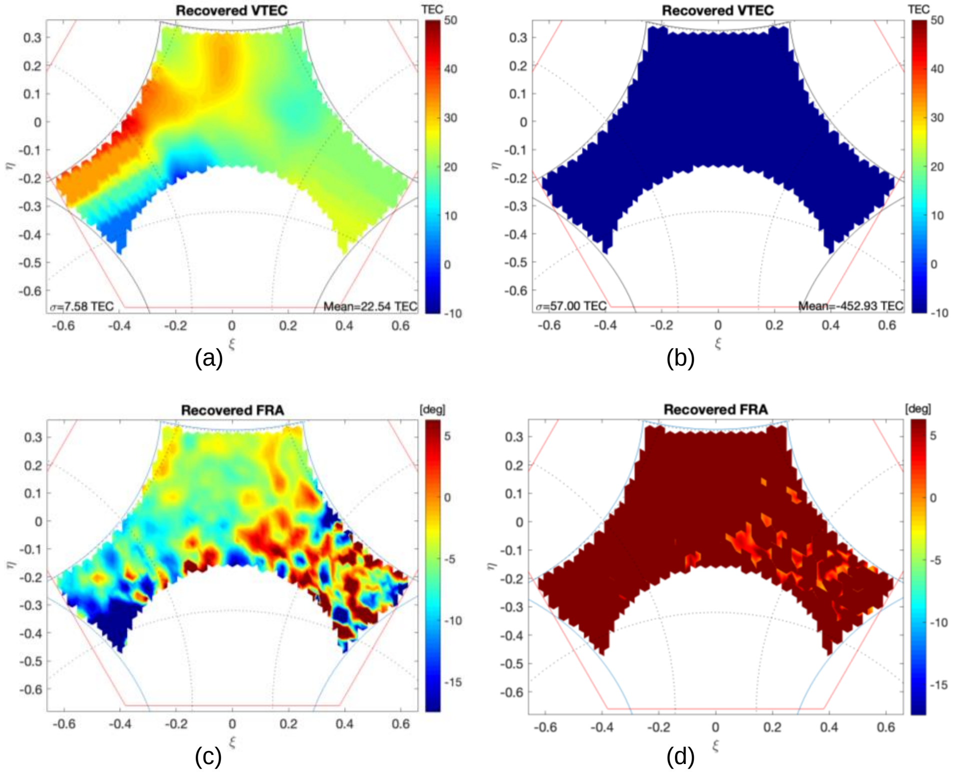

(a) (b) (c) (d)

*Figure 4.6. Snapshoots of **descending** orbits: (a) recovered VTEC of the core methodology, (b) recovered VTEC applying the second approach, (c) recovered FRA of the core methodology, (d) recovered FRA applying the second approach.*

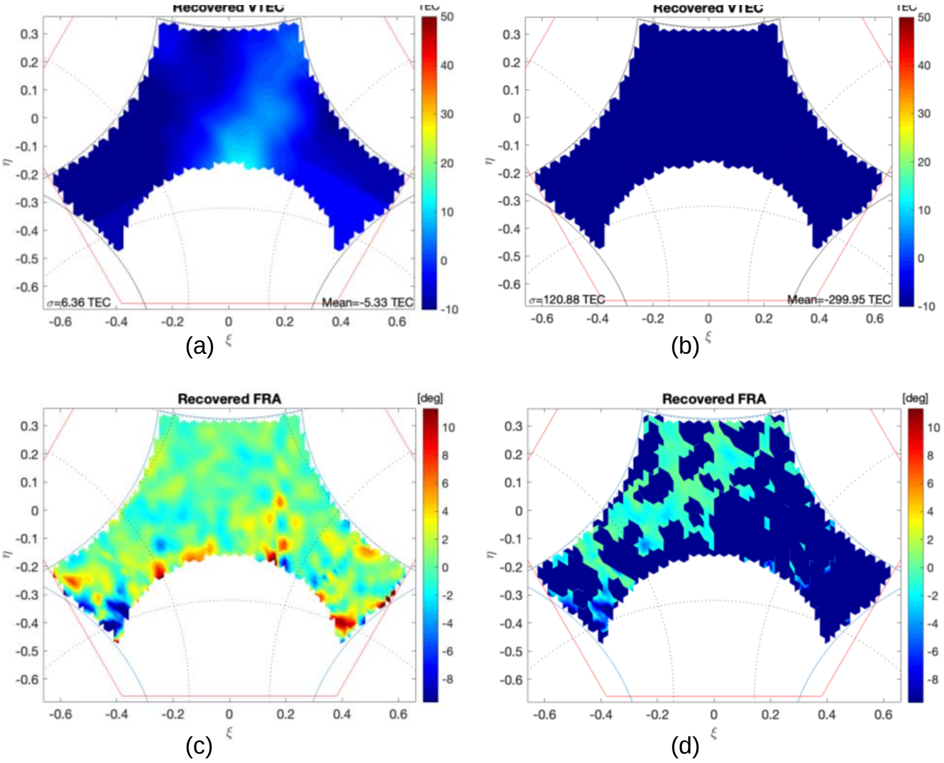

(a) (b) (c) (d)

*Figure 4.5. Snapshoots of **ascending** orbits: (a) recovered VTEC of the core methodology, (b) recovered VTEC applying the second approach, (c) recovered FRA of the core methodology, (d) recovered FRA applying the second approach.*

The results obtained have not been as expected, the opposite has occurred to what was initially thought. The values of VTEC are all negative and out of range. The FRA values are also out of the normal ranges.

It is possible that by removing the values of the solutions of the FRA that do not have the same sign as the $\cos\Theta_B$, the function takes values of solutions as good ones, that indeed are very far from the good values.

In fact, if the FRA has changed its sign, it may be due because this value is close to the geomagnetic equator and $\cos\Theta_B \approx 0$, which could easily have changed the sign with a litter noise. But it could also be because there is an indetermination and a change of sign, so even if another solution is chosen, this one may also be incorrect.

Also, it can be considered that VTEC is negative due to other parameters (other than Ω_f the and the $\cos\Theta_B$) of the Eq. (4.2).

It has been concluded that this approach does not work either.

4.2.3. Third Approach: Rejecting the negative VTEC values directly

Figure 3.12 is going to be shown again, along with the figures that correspond to the difference between the recovered VTEC and the L1 VTEC, in order to see the statistics to have a point of comparison. First, the plots of the methodology (from section 2.3.2.1) and those obtained by applying the third approach of the descending orbits are going to be shown, to compare them. And then the plots of the ascending orbit.

The results were expected to be better than the ones obtained with the core methodology, as in this way there should be no negative VTEC values (since they were rejected from the beginning) so the map should have no holes.

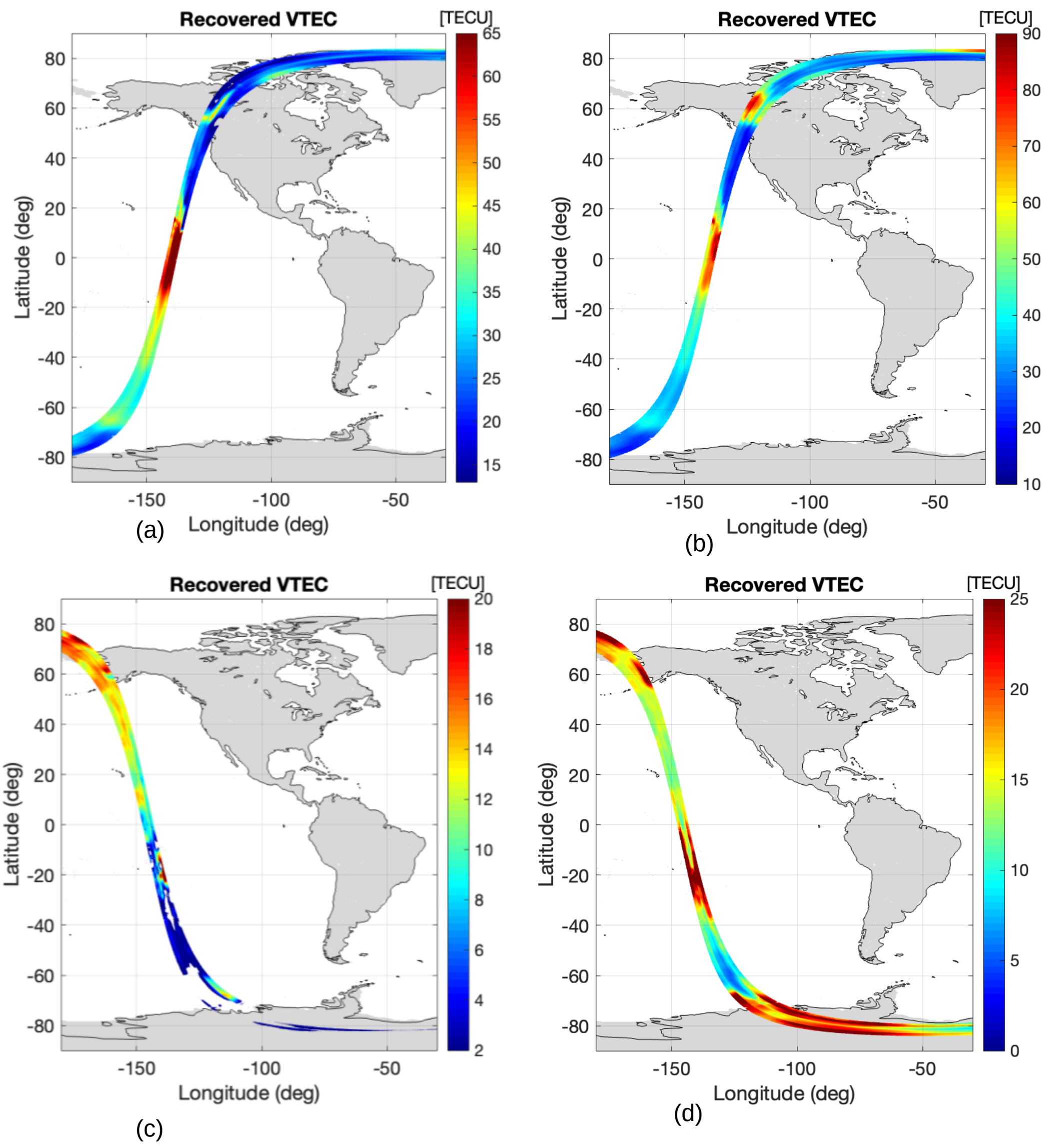

(a) (b) (c) (d)

*Figure 4.7. Recovered VTEC snapshoots of: <u>TOP</u>: **Descending** orbit (a) of the core methodology, (b) applying the third approach. <u>BOTTOM</u>: **Ascending** orbit (c) of the core methodology, (d) applying the third approach.*

It can be observed that there are no holes in the maps, which means that now there are not negative values of VTEC. The wanted objectives were achieved, especially in the ascending orbit, where the most affected areas were able to be recovered. However, the VTEC values are now very high, making the maps more reddish.

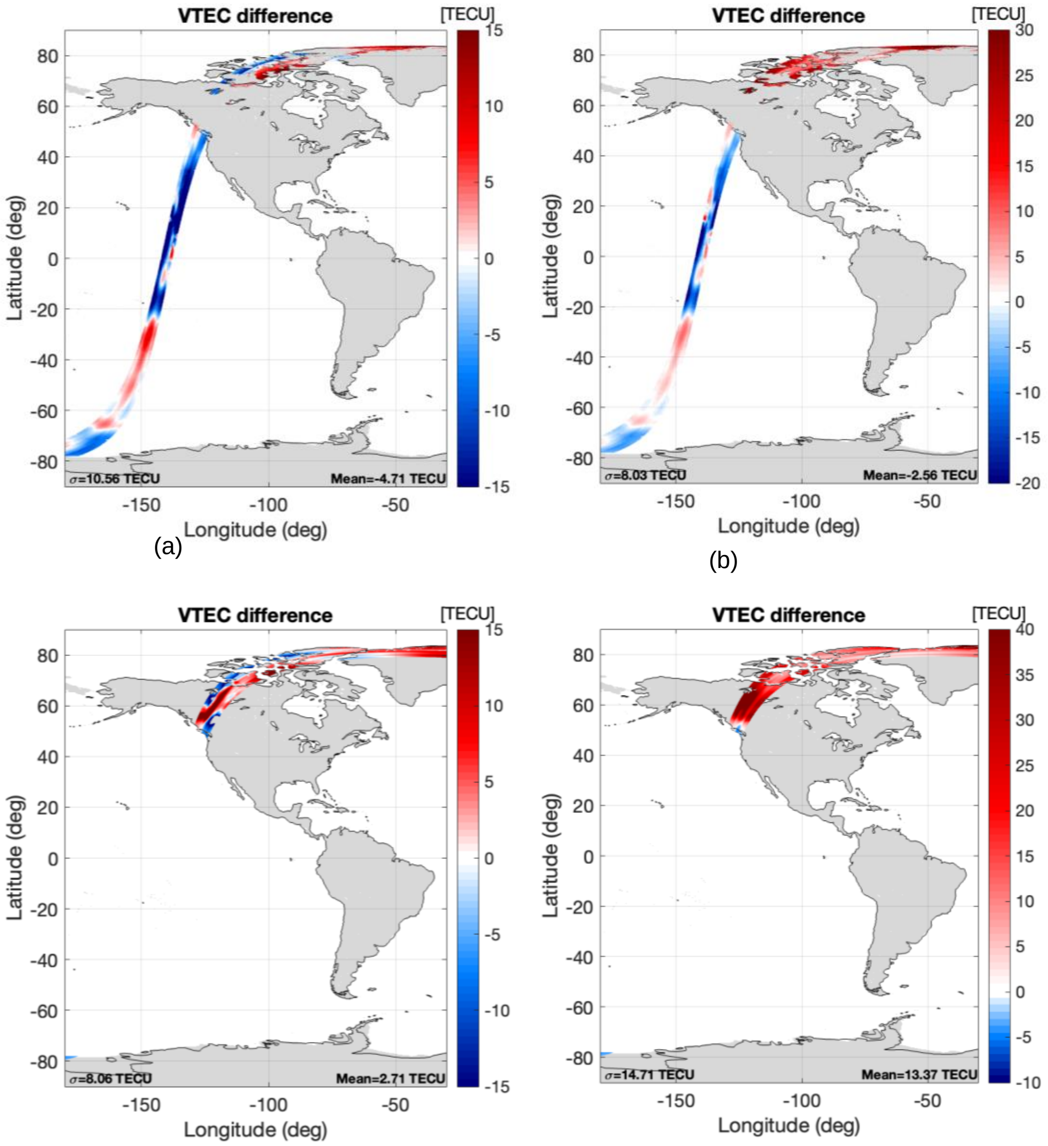

(a) (b)

(c) (d)

*Figure 4.8. Difference between the recovered VTEC and the L1 VTEC snapshoots of **descending** orbit: (a) of the core methodology over ocean, (b) applying the third approach over ocean, (c) of the core methodology over land, (d) applying the third approach over land.*

In the descending orbit it can be seen that the STD improves over ocean, going from 10.56 TECU (in Figure 4.8.a.) to 8.03 TECU (in Figure 4.8.b.), but gets a lot worse over land, going from 8.06 TECU (in Figure 4.8.c.) to 14.71 TECU (in Figure 4.8.d.). With the mean difference happens the same as before, it improves over ocean, going from -4.71 TECU (in Figure 4.8.a.) to -2.56 TECU (in Figure 4.8.b.), but gets a lot worse over land, going from -2.71 TECU (in Figure 4.8.c.) to 13.37 TECU (in Figure 4.8.d.).

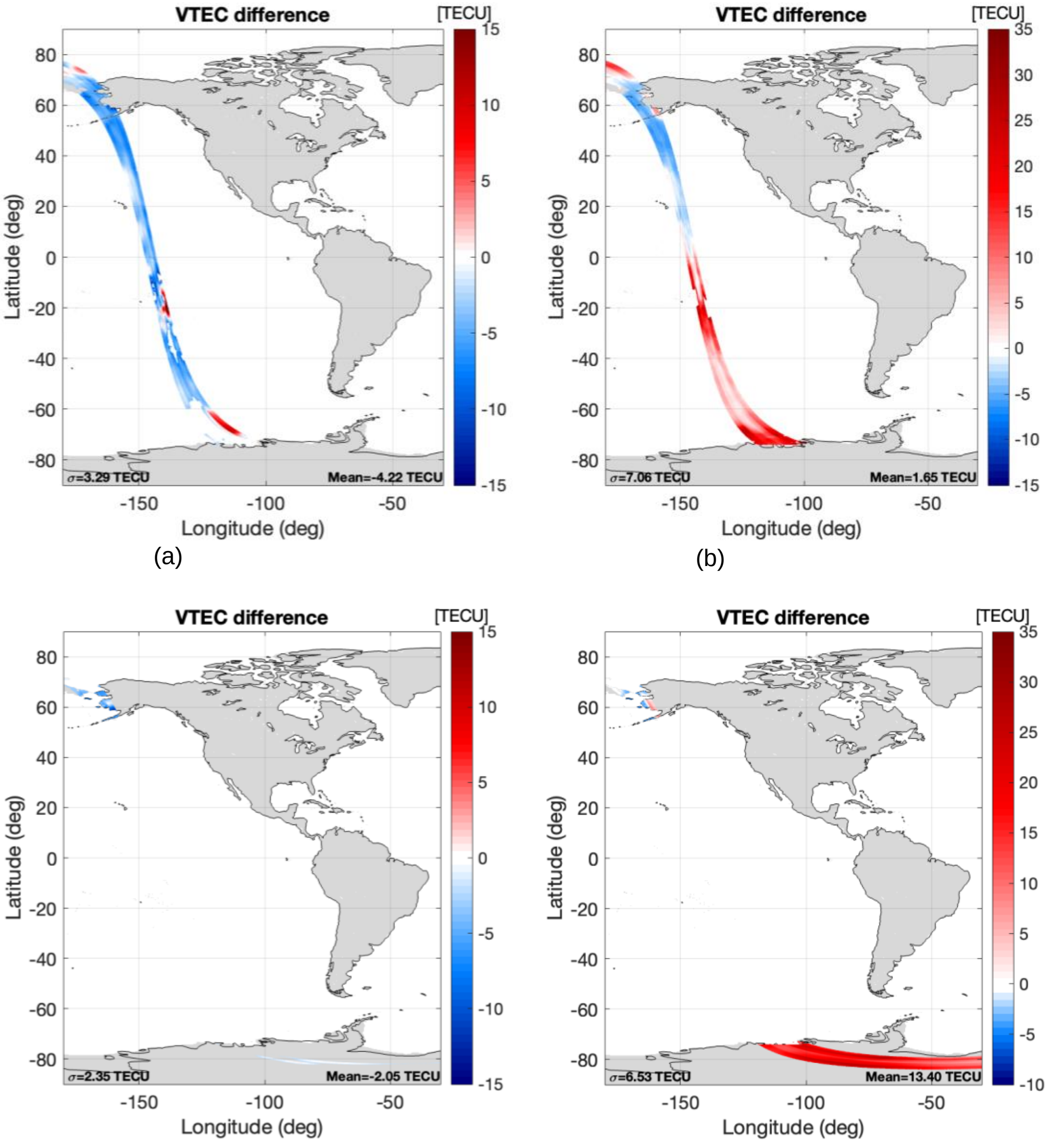

(a) (b)

(c) (d)

Figure 4.9. Difference between the recovered VTEC and the L1 VTEC snapshoots of ***ascending*** *orbit: (a) of the core methodology over ocean, (b) applying the third approach over ocean, (c) of the core methodology over land, (d) applying the third approach over land.*

In the ascending orbit it can be seen that the STD gets worse in both cases, over ocean going from 3.29 TECU (in Figure 4.9.a.) to 7.06 TECU (in Figure 4.9.b.), and over land going from 2.35 TECU (in Figure 4.9.c.) to 6.53 TECU (in Figure 4.9.d.). The mean difference improves over ocean, going from -4.22 TECU (in Figure 4.9.a.) to 1.65 TECU (in Figure 4.9.b.), but gets worse over land, going from -2.05 TECU (in Figure 4.9.c.) to 13.40 TECU (in Figure 4.9.d.).

It can be said that there has been an improvement with respect to the ones obtained applying the core methodology (Figure 4.7.b. and Figure 4.7.d.), since now it does not remove values and there are not holes. However, the statistics over land have worsened, this is due to the fact that a bias is being applied by only considering the positive values of VTEC.

It can be concluded that by applying this third approach the objective was achieved in the sense that the negative values of VTEC were rejected and VTEC could be recovered correctly.

4.2.3.1. Comparison of FRA and VTEC with other sources

The plots of the comparison between different FRA sources were reproduced. It shows the plots of the descending orbit (top) and ascending orbit (bottom) of a pixel in the center of the swath with respect to the latitude: the red line refers to L1 FRA, the green line refers to the third approach, and the blue line to the core methodology.

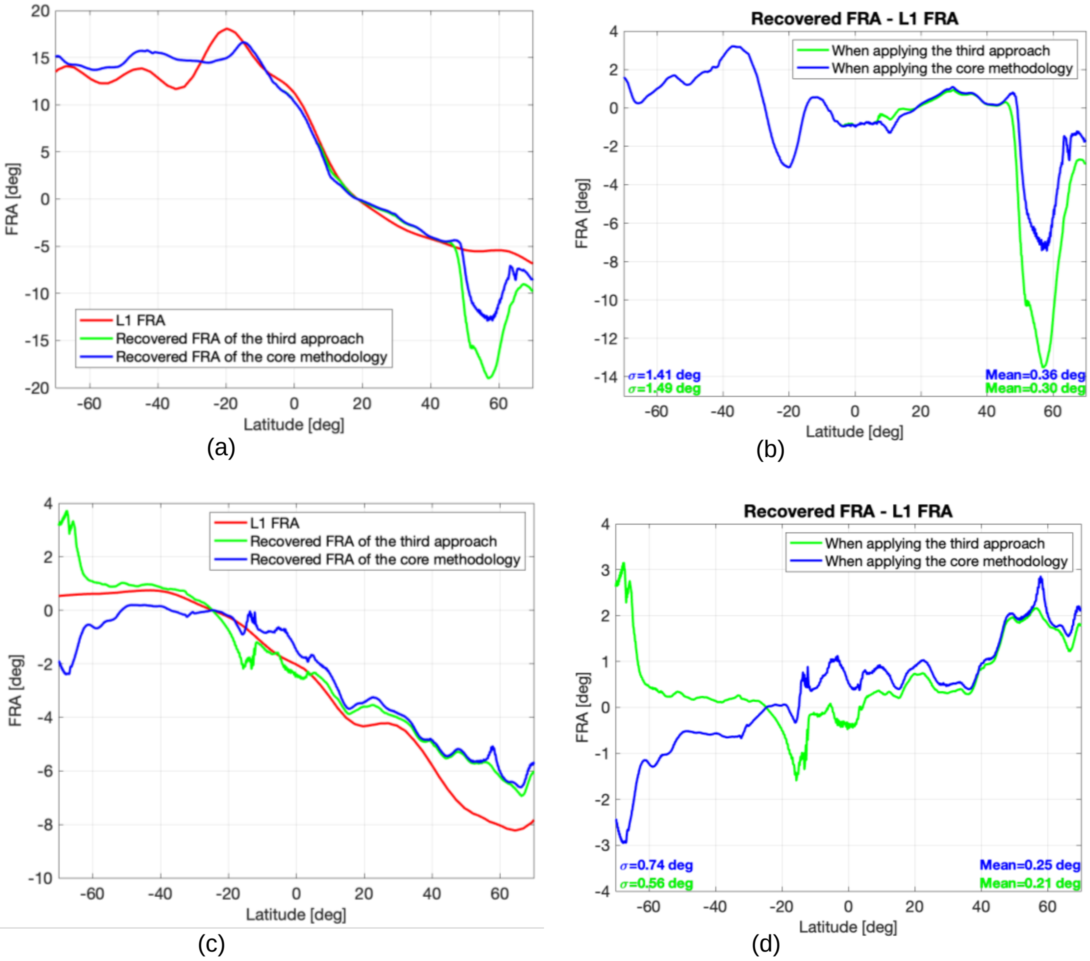

(a) (b)

(c) (d)

*Figure 4.10. Plots of the FRA vs latitude of a pixel in the center of the swath of the: TOP: **descending** orbit (a) and, (b) difference between the recovered FRA of the third approach and the L1 FRA (green), and the recovered FRA of the core methodology and the L1 FRA (blue). BOTTOM: **ascending** orbit (c) and, (d) difference between the recovered FRA of the third approach and the L1 FRA (green), and the recovered FRA of the core methodology and the L1 FRA (blue).*

It can be seen that applying the third approach has an important impact. Around 50ºN the values decrease a bit more (green line) than by applying the core methodology (blue line) in the descending orbit. And also, the mean difference improves. In the ascending orbit, in latitudes below 0ºN, there is a drastic change in the values of the FRA. And in Figure 4.10.d. shows that the statistics have improve.

Now, it will be shown the comparison of the retrieved VTEC from SMOS with other VTEC sources. It shows the plots of the descending orbit (left) and ascending orbit (right) of a pixel in the center of the swath. Where the red line refers to the L1 VTEC, the green line refers to the third approach, the blue line to the core methodology, the black line refers to the IGS VTEC, and the pink line to the A3TEC.

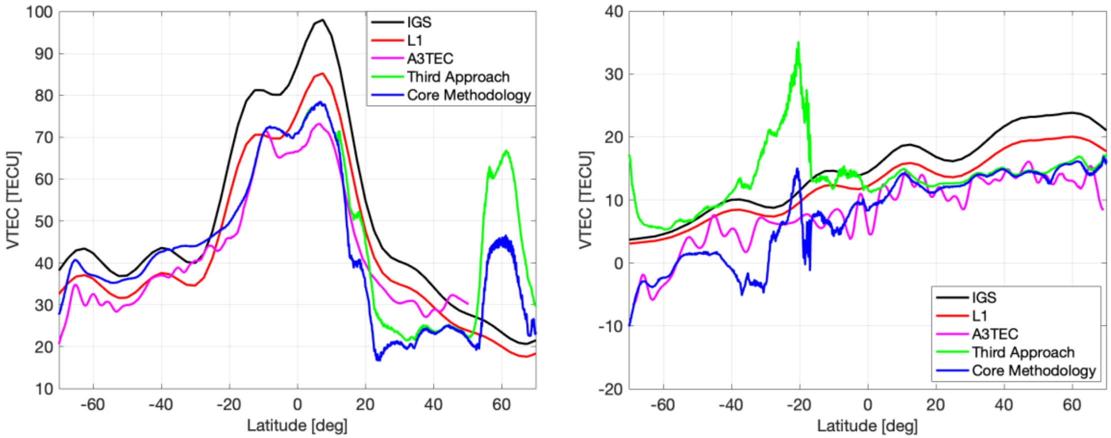

(a) (b)

Figure 4.11. Comparison of the VTEC with different sources of: (a) descending orbit, (b) ascending orbit.

It can be seen in these plots the impact of applying the third approach, mostly in the ascending orbits, where now there are not negative values of VTEC. The green line always stays above the zero. Also, for both orbits the recovery of VTEC presents less ripples than the A3TEC.

4.2.4. Summary

The first approach was to change the order of the core methodology. It did not work because when changing the order of some steps of the core methodology, at the moment of applying the temporal filter, it considers values that cause indetermination in the calculation of the FRA since the beginning. Where more negative values of the VTEC were obtained, leading to a worse result. The STD has significantly gotten worse, both in descending and ascending orbits, especially in the ocean.

The second approach was to force the sign of the FRA and the $\cos\Theta_B$ to be equal. It did not work either because by removing the values of the solutions of the FRA that do not have the same sign as the $\cos\Theta_B$, the function takes values of solutions as good ones, that indeed are very far from the good values, obtaining values of VTEC that are all negative and out of range.

The third approach was to directly reject the negative VTEC values. With this approach the objective was achieved in the sense that the negative values of VTEC were rejected and the VTEC could be recovered correctly, since now it does not remove values and there are not holes in the map. Also, the statistics of the descending orbit over ocean have an improvement. However, the statistics over land for both orbits have worsened, this is due to the fact that a bias is being applied by only considering the positive values of VTEC.

To sum up, the third approach is the one that meets the expectations, while the first two do not achieve the desired results. It is worth mentioning that the retrieval is compared to L1 VTEC only for reference, which means that these are differences and not errors.

4.3. Thresholds

Each value of each threshold will be analyzed in order to find the most optimum. As mentioned before, in this section will only be shown the final plots with the final results (one plot with all the modified thresholds), and in the appendix section B all the plots for each value of each threshold will be shown.

4.3.1. Core Methodology

All the results are going to be shown in Table 4.1, to see if the values of the statistics improve ("YES" in green), stays the same ("SAME" in yellow), or worsens ("NO" in red) with respect to the original values, this was done by reproducing the plots for each value of each threshold:

Table 4.1. Results of all the Thresholds applied to the Core Methodology.

Core Methodology																		
Thresholds			**Threshold1**			**Threshold2**				**Size Temporal Filter**		**Size Spatial Filter**				**Incidence Angle**	
Original Value			4			0.9				43		0.189				25	
New Value			2	**3**	5	0.5	0.8	**1**	1.3	41	**45**	0.18	0.195	**0.2**	0.25	23	**24**
Descending Orbit	**Over Ocean**	**Sigma**	NO	**YES**	YES	YES	SAME	**SAME**	NO	NO	**YES**	NO	SAME	**YES**	YES	YES	**YES**
		Mean difference	NO	**YES**	NO	YES	YES	**YES**	NO	SAME	**SAME**	YES	SAME	**YES**	YES	YES	**YES**
	Over Land	**Sigma**	NO	**YES**	YES	NO	NO	**YES**	YES	NO	**YES**	NO	SAME	**YES**	YES	NO	**NO**
		Mean difference	NO	**NO**	YES	NO	NO	**YES**	YES	NO	**YES**	NO	SAME	**YES**	NO	YES	**YES**
Ascending Orbit	**Over Ocean**	**Sigma**	NO	**YES**	NO	SAME	SAME	**SAME**	SAME	NO	**YES**	NO	SAME	**SAME**	YES	YES	**YES**
		Mean difference	NO	**YES**	NO	SAME	SAME	**YES**	NO	SAME	**SAME**	YES	SAME	**YES**	NO	NO	**NO**
	Over Land	**Sigma**	YES	**YES**	NO	YES	SAME	**SAME**	SAME	NO	**YES**	NO	SAME	**YES**	NO	NO	**NO**
		Mean difference	NO	**YES**	NO	NO	SAME	**NO**	YES	YES	**NO**	YES	SAME	**NO**	NO	YES	**YES**
Chosen Values			**3**			**1**				**45**		**0.2**				**24**	

By showing all the results in this table, it was much easier to identify which threshold made an improvement in the statistics. The chosen value was underlined, in bold and highlighted in blue at the bottom of the table:

- **Threshold1**: 3 Kelvin
- **Threshold2**: 1 Kelvin.
- **Size Temporal Filter**: 45 snapshoots.
- **Size Spatial Filter**: 0.2 (d/λ).
- **Incidence Angle**: 24º.

The main objective was to improve the statistics over the ocean, since over land is more challenging due to the presence of some interferences.

The chosen thresholds were put together and the plots of the descending orbit were reproduced and compared with the original thresholds:

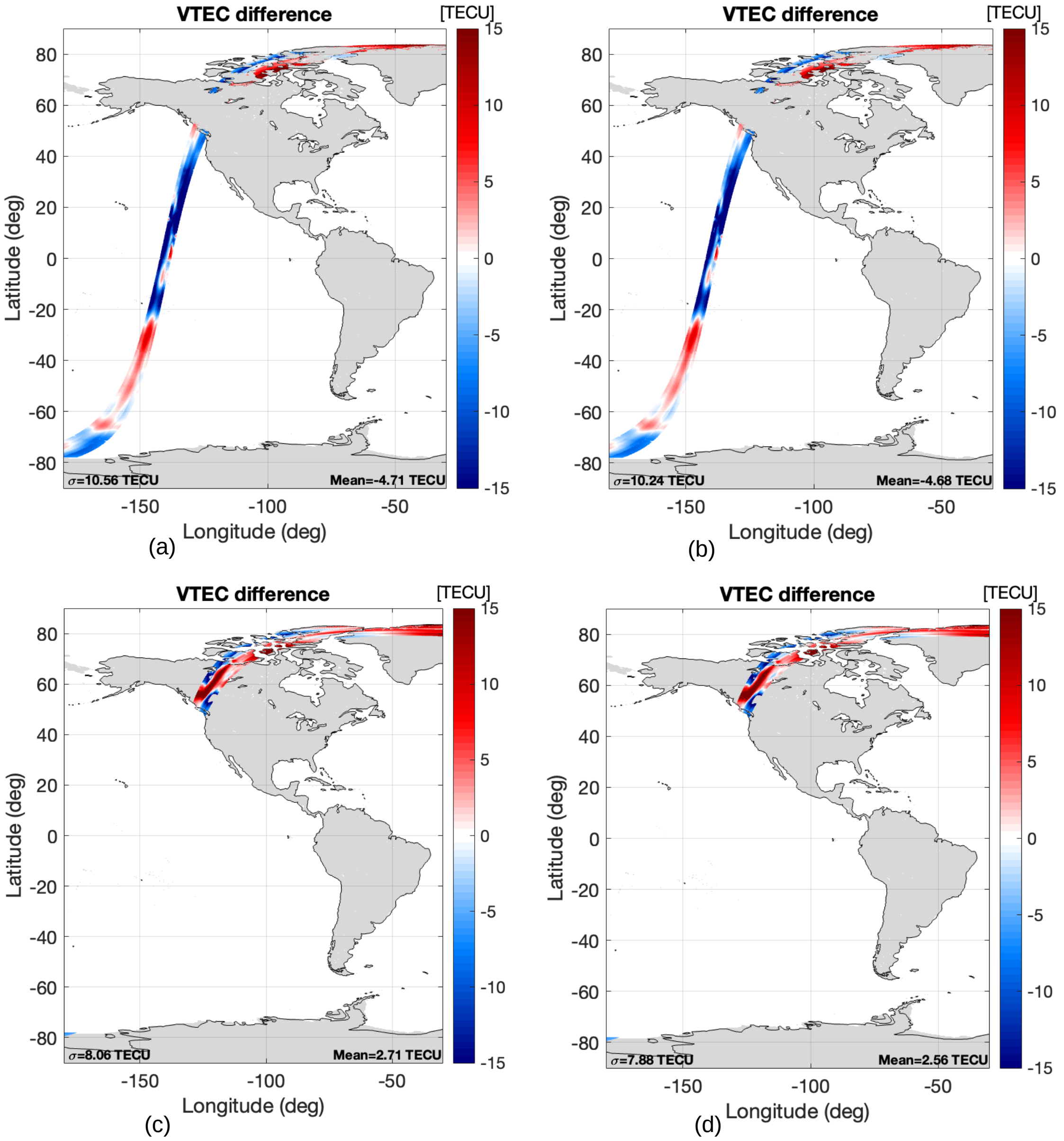

(a) (b) (c) (d)

*Figure 4.12. VTEC maps of **descending orbit** of the Core Methodology: (a) difference between the recovered VTEC and the L1 VTEC with the original thresholds over **ocean**, (b) the same but with the new thresholds, (c) difference between the recovered VTEC and the L1 VTEC with the original thresholds over **land**, (d) the same but with the new thresholds.*

It can be observed that in the descending orbit the STD improves in both cases, over ocean going from 10.56 TECU (in Figure 4.12.a.) to 10.24 TECU (in Figure 4.12.b.), and over land going from 8.06 TECU (in Figure 4.12.c.) to 7.88 TECU (in Figure 4.12.d.). The mean difference improves over ocean going from -4.71 TECU (in Figure 4.12.a.) to -4.68 TECU (in Figure 4.12.b.), and also over land going from 2.71 TECU (in Figure 4.12.c.) to 2.56 TECU (in Figure 4.12.d.). Therefore, it can be noticed that the overall statistics have improved in the descending orbits.

Then, the plots of the ascending orbit with the new thresholds were reproduced and compared with the original thresholds of the core methodology:

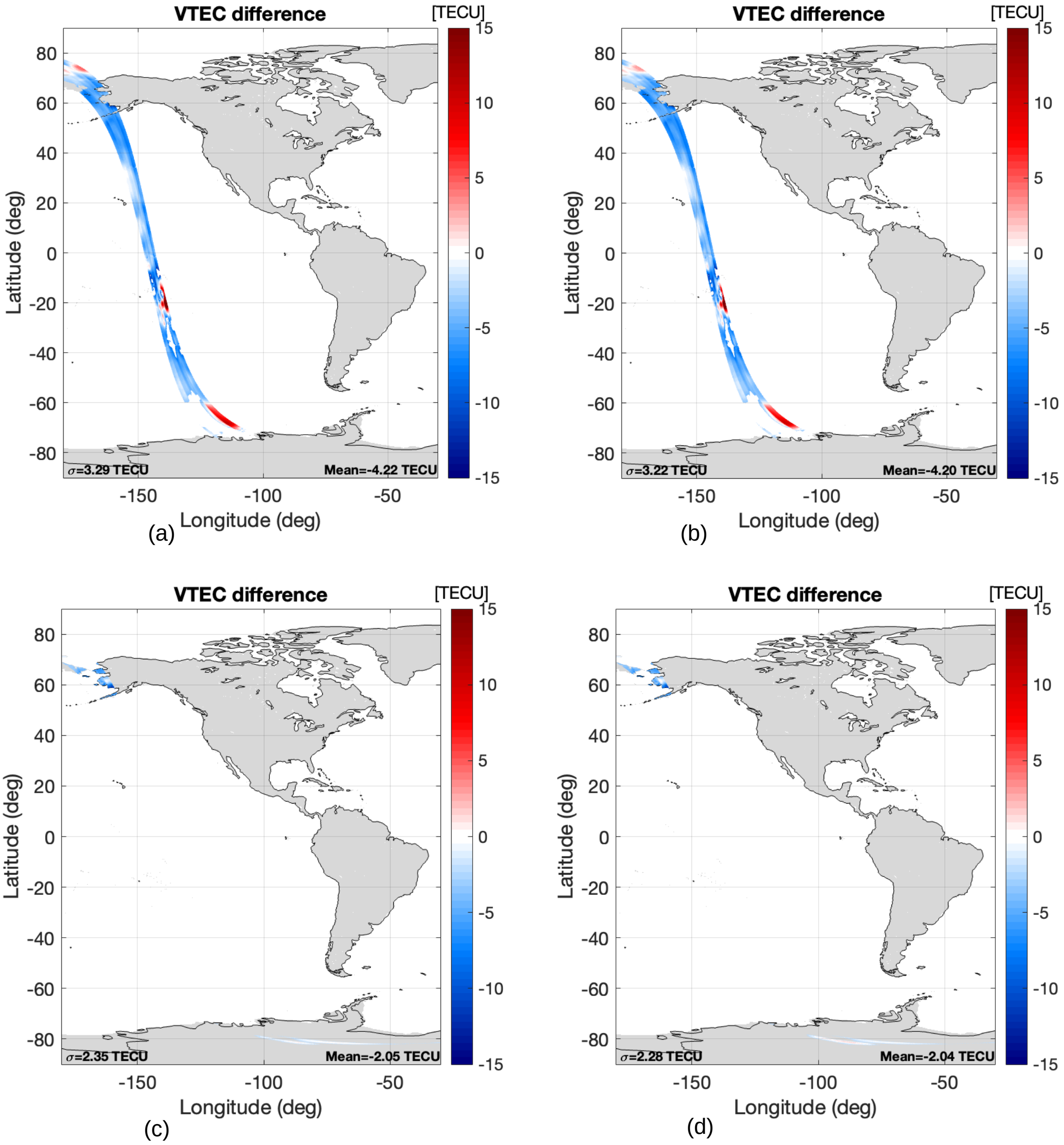

*Figure 4.13. VTEC maps of **ascending orbit** of the Core Methodology: (a) difference between the recovered VTEC and the L1 VTEC with the <u>original thresholds</u> over **ocean**, (b) the same but with the <u>new thresholds</u>, (c) difference between the recovered VTEC and the L1 VTEC with the <u>original thresholds</u> over **land**, (d) the same but with the <u>new thresholds</u>.*

It can be observed that in the ascending orbit the STD improves in both cases, over ocean going from 3.29 TECU (in Figure 4.13.a.) to 3.22 TECU (in Figure 4.13.b.), and over land going from 2.35 TECU (in Figure 4.13.c.) to 2.28 TECU (in Figure 4.13.d.). The mean difference also improves a little in both cases, over ocean going from -4.22 TECU (in Figure 4.13.a.) to -4.20 TECU (in Figure 4.13.b.), and over land going from -2.05 TECU (in Figure 4.13.c.) to -2.04 TECU (in Figure 4.13.d.). Therefore, it can be noticed that the statistics have improved a bit in the ascending orbit.

It can be concluded that by applying the new thresholds the statistics have improved with respect to the original thresholds.

4.3.1.1. Comparison of FRA and VTEC with other sources

The plots of the comparison between different FRA sources were reproduced. It shows the plots of the descending orbit (top) and ascending orbit (bottom) of a pixel in the center of the swath with respect to the latitude: the red line refers to L1 FRA, the green line refers to the core methodology with the new thresholds, and the blue line to the core methodology with the original thresholds.

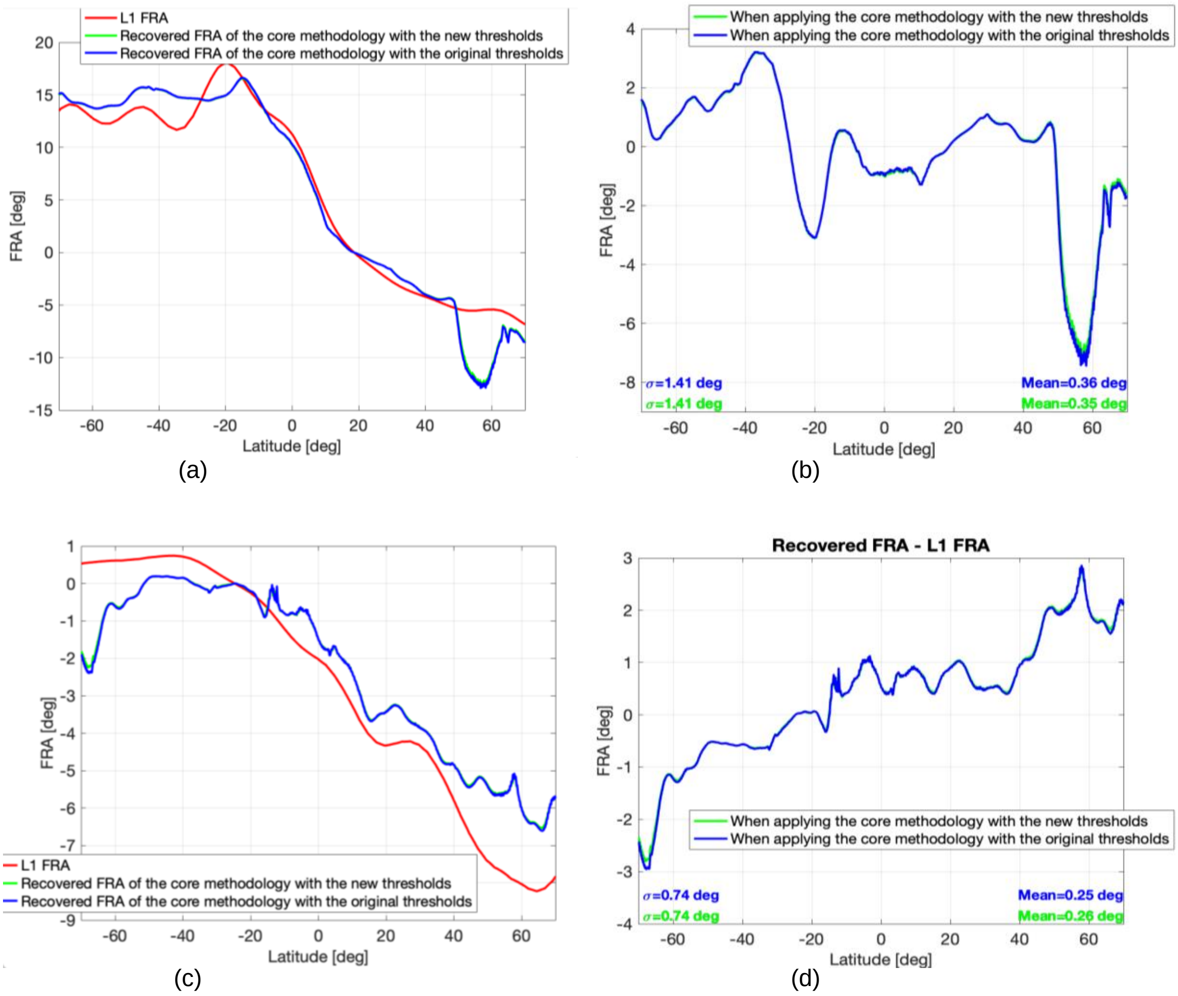

(a) (b)

(c) (d)

*Figure 4.14. Plots of the FRA vs latitude of a pixel in the center of the swath of the: TOP: **descending** orbit (a) and, (b) difference between the recovered FRA of the core methodology with the new thresholds and the L1 FRA (green), and the recovered FRA of the core methodology with the original thresholds and the L1 FRA (blue). BOTTOM: **ascending** orbit (c) and, (d) difference between the recovered FRA of the core methodology with the new thresholds and the L1 FRA (green), and the recovered FRA of the core methodology with the original thresholds and the L1 FRA (blue).*

It can be seen that there has not been a significant impact. For both orbits, in Figure 4.14.b. and Figure 4.14.d., the mean difference has improved.

Now, it will be shown the comparison of the retrieved VTEC from SMOS with other VTEC sources. It shows the plots of the descending orbit (left) and ascending orbit (right) of a pixel in the center of the swath. Where the red line refers to the L1 VTEC, the green line refers to the core methodology with the new thresholds, the blue line to the core methodology with the original thresholds, the black line refers to the IGS VTEC, and the pink line to the A3TEC.

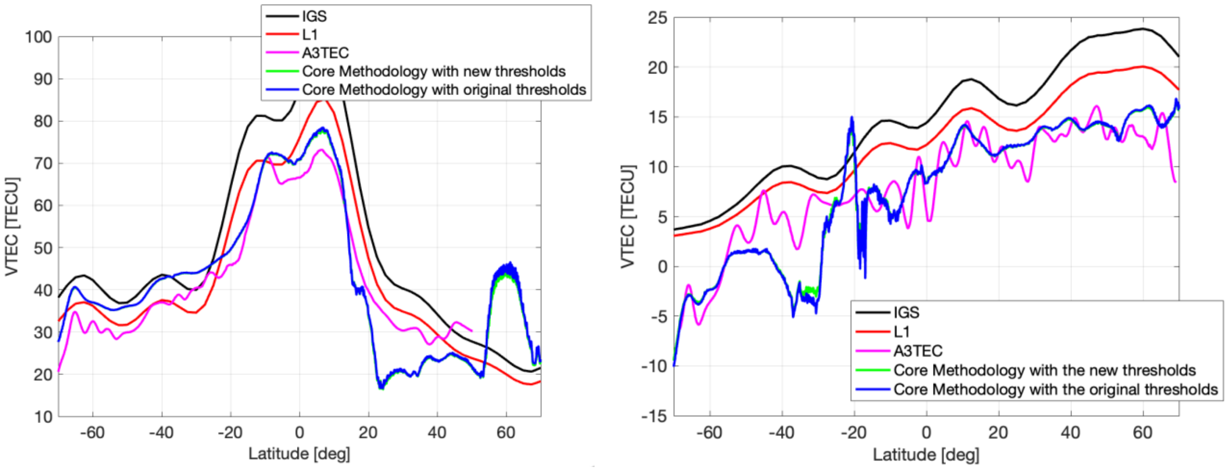

(a) (b)

Figure 4.15. Comparison of the VTEC with different sources of: (a) descending orbit, (b) ascending orbit.

In this plots, no significant changes can be seen either, except that the recovery of VTEC has less ripples.

4.3.2. Applying the Third Approach

Now, the statistics of the plots obtained by applying the third approach are attempted to be improved. As mentioned before, by applying this third approach the statistics of the descending orbit over ocean improves. But for both orbits over land worsens because a bias is being applied by only considering the positive values of VTEC.

4.3.2.1. Same Thresholds as before

As in the core methodology the statistics have improved with the thresholds mentioned above, these same thresholds are going to be applied in this case to see if the same results can be achieved, an improvement of the statistics.

- **Threshold1**: 3 Kelvin
- **Threshold2**: 1 Kelvin.
- **Size Temporal Filter**: 45 snapshoots.
- **Size Spatial Filter**: 0.2 (d/λ).
- **Incidence Angle**: 24º.

The plots for the descending orbit were reproduced and compared with the plots with the original thresholds:

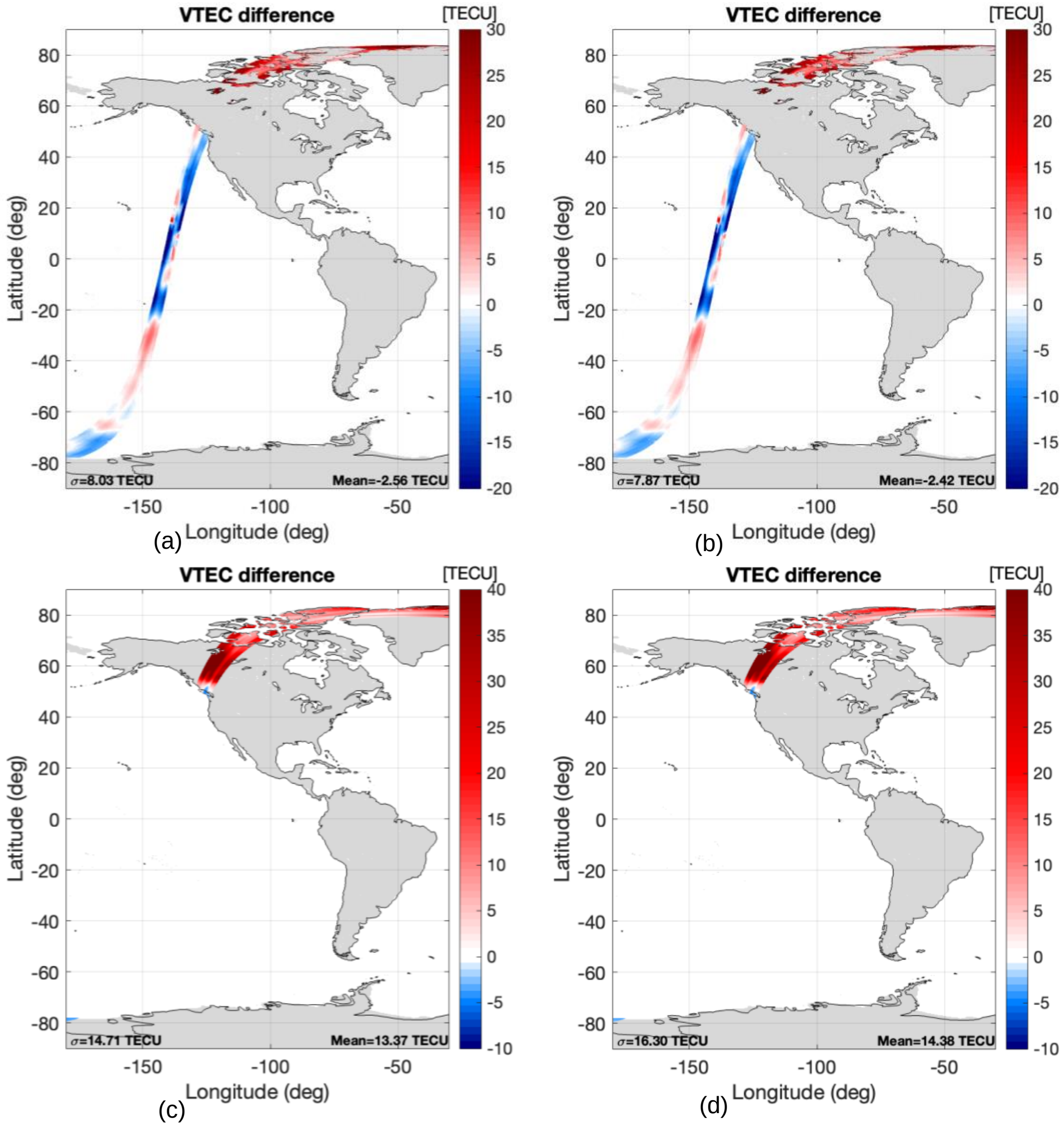

Figure 4.16. VTEC maps of ***descending orbit*** *of the Third Approach: (a) difference between the recovered VTEC and the L1 VTEC with the original thresholds over* ***ocean****, (b) the same but with the same thresholds tried before, (c) difference between the recovered VTEC and the L1 VTEC with the original thresholds over* ***land****, (d) the same but with the same thresholds tried before.*

It can be observed that in the descending orbit the STD improves over ocean going from 8.03 TECU (in Figure 4.16.a.) to 7.87 TECU (in Figure 4.16.b.) but gets worse over land going from 14.71 TECU (in Figure 4.16.c.) to 16.30 TECU (in Figure 4.16.d.). With the mean difference happens the same as before, it improves over ocean going from -2.56 TECU (in Figure 4.16.a.) to -2.42 TECU (in Figure 4.16.b.) but gets worse over land going from 13.37 TECU (in Figure 4.16.c.) to 14.38 TECU (in Figure 4.16.d.). Therefore, it can be noticed that applying the same thresholds as before, the statistics improves over ocean but worsens over land in the descending orbits.

Then, the plots of the ascending orbit with the same thresholds as before were reproduced and compared with the original thresholds:

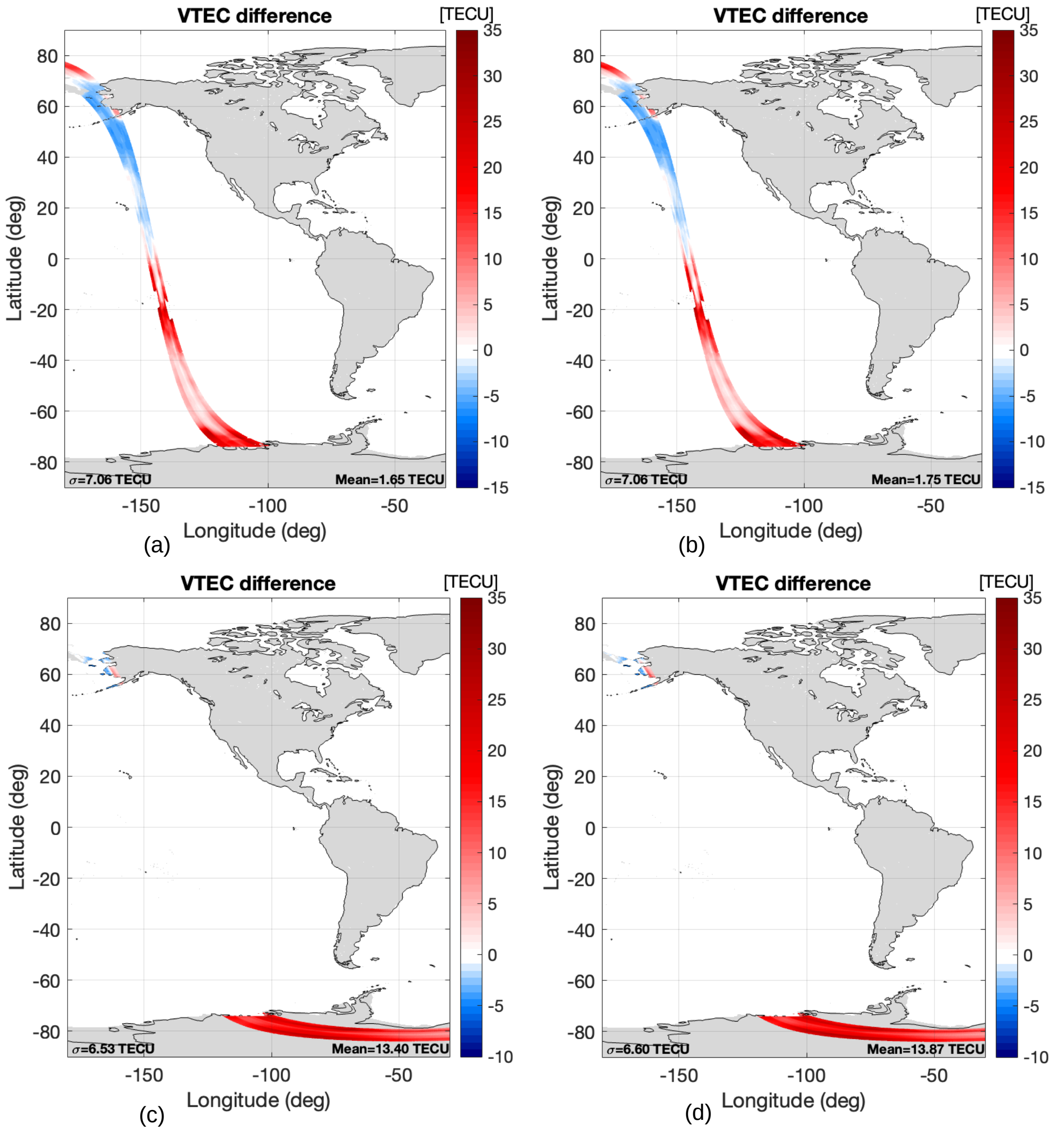

(a) (b)

(c) (d)

Figure 4.17. VTEC maps of ***ascending orbit*** *of the Third Approach: (a) difference between the recovered VTEC and the L1 VTEC with the original thresholds over* ***ocean****, (b) the same but with the same thresholds tried before, (c) difference between the recovered VTEC and the L1 VTEC with the original thresholds over* ***land****, (d) the same but with the same thresholds tried before.*

It can be seen that in ascending orbits the STD remains the same over ocean staying at 7.06 TECU (in Figure 4.17.a. and Figure 4.17.b.) but worsens a bit over land going from 6.53 TECU (in Figure 4.17.c.) to 6.60 TECU (in Figure 4.17.d.). The mean difference worsens in both cases, over ocean going from 1.65 TECU (in Figure 4.17.a.) to 1.75 TECU (in Figure 4.17.b.), and over land going from 13.40 TECU (in Figure 4.17.c.) to 13.87 TECU (in Figure 4.17.d.). Therefore, it can be noticed that the overall statistics worsens a bit in the ascending orbits.

It can be concluded that the statistics improves over ocean but worsens over land in the descending orbits, and the overall statistics worsens a bit in the ascending orbits.

4.3.2.2. New Thresholds

The procedure done in the section 4.3.1 was repeated to see if the statistics could be improved more since the other thresholds were expected to give better results than they did.

All the results are going to be shown in Table 4.2, to see if the values of the statistics improve (“YES” in green), stays the same (“SAME” in yellow), or worsens (“NO” in red) with respect to the original values, this was done by reproducing the plots for each value of each threshold:

Table 4.2. Results of all the Thresholds applied to the Third Approach.

Third Approach																	
Thresholds			**Threshold1**			**Threshold2**				**Size Temporal Filter**		**Size Spatial Filter**				**Incidence Angle**	
Original Value			4			0.9				43		0.189				**25**	
New Value			2	3	**5**	0.5	0.8	**1**	1.3	41	**45**	**0.175**	0.18	0.195	0.2	23	24
Descending Orbit	**Over Ocean**	**Sigma**	NO	NO	**YES**	YES	YES	**SAME**	SAME	YES	**SAME**	**NO**	NO	SAME	YES	YES	YES
		Mean difference	YES	YES	**NO**	YES	SAME	**SAME**	NO	YES	**NO**	**NO**	NO	SAME	YES	YES	YES
	Over Land	**Sigma**	NO	NO	**YES**	NO	NO	**YES**	YES	NO	**YES**	**YES**	YES	SAME	NO	NO	NO
		Mean difference	NO	NO	**YES**	NO	NO	**YES**	YES	NO	**YES**	**YES**	YES	SAME	NO	NO	NO
Ascending Orbit	**Over Ocean**	**Sigma**	NO	SAME	**SAME**	SAME	SAME	**SAME**	SAME	NO	**YES**	**SAME**	SAME	SAME	SAME	NO	NO
		Mean difference	NO	NO	**YES**	SAME	SAME	**SAME**	SAME	NO	**YES**	**YES**	SAME	SAME	NO	NO	NO
	Over Land	**Sigma**	YES	YES	**NO**	NO	SAME	**YES**	YES	NO	**SAME**	**YES**	YES	SAME	NO	NO	NO
		Mean difference	NO	SAME	**NO**	NO	SAME	**YES**	YES	NO	**YES**	**YES**	YES	SAME	NO	NO	NO
Chosen Values			**5**			**1**				**45**		**0.175**				**25**	

By showing all the results in this table, it was much easier to identify which threshold made an improvement in the statistics. The chosen value was underlined, in bold and highlighted in blue at the bottom of the table:

- **Threshold1**: 5 Kelvin
- **Threshold2**: 1 Kelvin.
- **Size Temporal Filter**: 45 snapshoots.
- **Size Spatial Filter**: 0.175 (d/λ).
- **Incidence Angle**: 25º.

The chosen thresholds were put together and the plots of the descending orbit were reproduced and compared with the original thresholds:

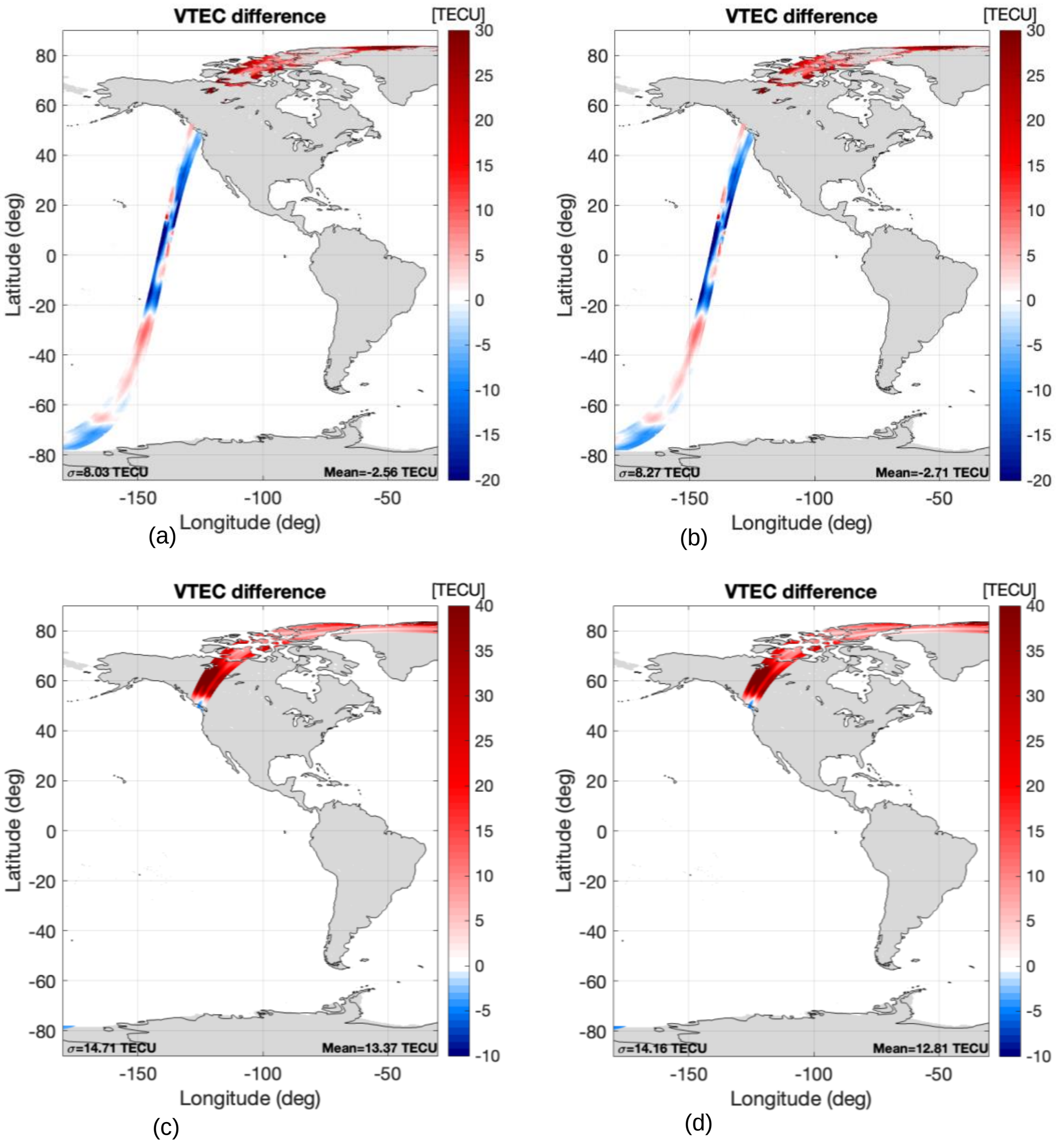

*Figure 4.18. VTEC maps of **descending orbit** of the Third Approach: (a) difference between the recovered VTEC and the L1 VTEC with the original thresholds over **ocean**, (b) the same but with different thresholds, (c) difference between the recovered VTEC and the L1 VTEC with the original thresholds over **land**, (d) the same but with different thresholds.*

It can be seen that in the descending orbits the STD gets worse over ocean going from 8.03 TECU (in Figure 4.18.a.) to 8.27 TECU (in Figure 4.18.b.) but improves over land going from 14.71 TECU (in Figure 4.18.c.) to 14.18 TECU (in Figure 4.18.d.). With the mean difference happens the same as before, it worsens over ocean going from -2.56 TECU (in Figure 4.18.a.) to -2.71 TECU (in Figure 4.18.b.), and it improves over land going from 13.37 TECU (in Figure 4.18.c.) to 12.81 TECU (in Figure 4.18.d.). Therefore, it can be noticed that the statistics get worse over ocean but improves over land in the descending orbit.

Then, the plots of the ascending orbit with the new thresholds were reproduced and compared with the original thresholds of the core methodology:

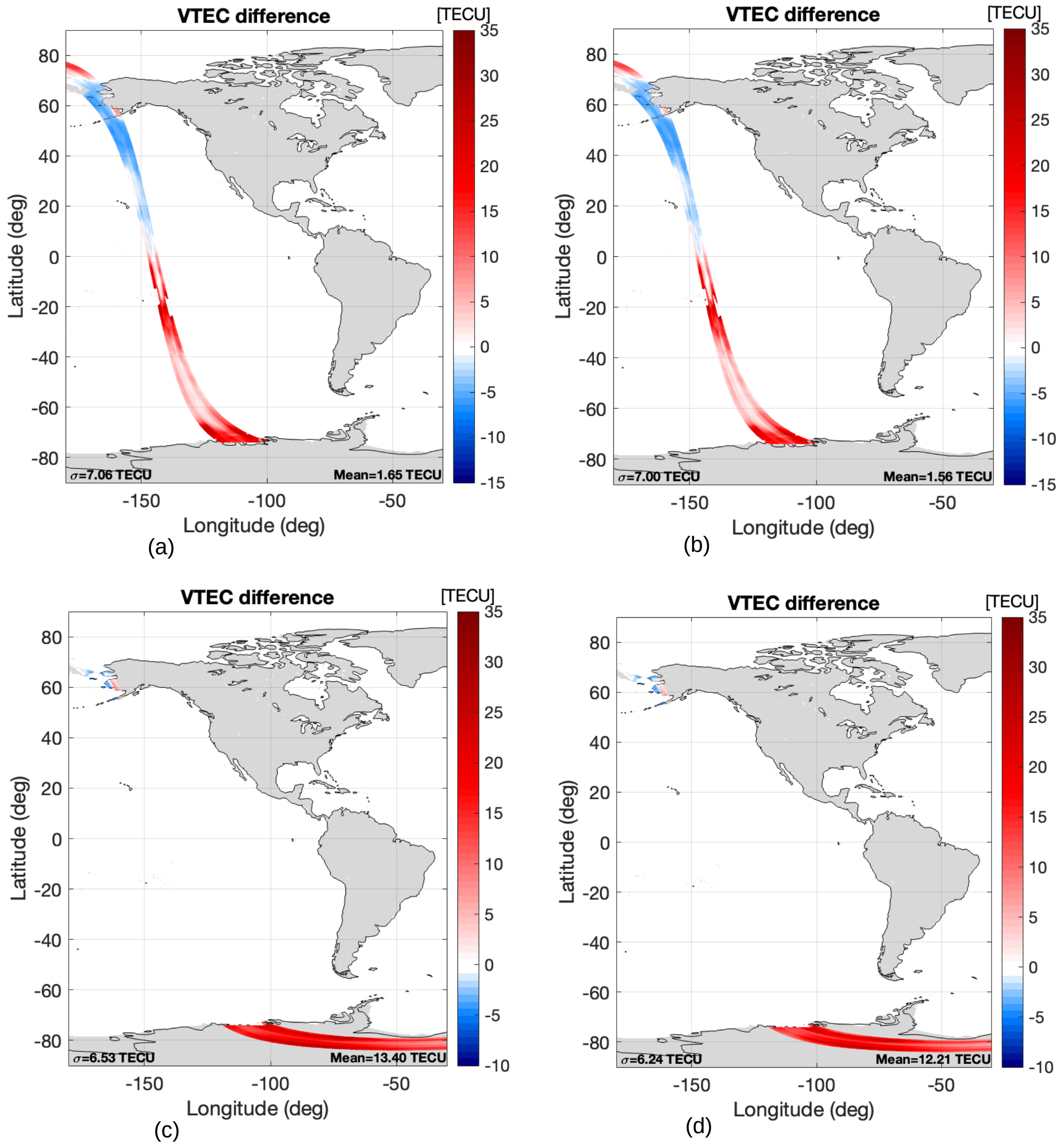

(a) (b) (c) (d)

Figure 4.19. VTEC maps of ***ascending orbit*** *of the Third Approach: (a) difference between the recovered VTEC and the L1 VTEC with the original thresholds over* ***ocean****, (b) the same but with different thresholds, (c) difference between the recovered VTEC and the L1 VTEC with the original thresholds over* ***land****, (d) the same but with different thresholds.*

It can be observed that in the ascending orbit the STD improves a little bit in both cases, over the ocean going from 7.06 TECU (in Figure 4.19.a.) to 7.00 TECU (in Figure 4.19.b.) and over land going from 6.53 TECU (in Figure 4.19.c.) to 6.24 TECU (in Figure 4.19.d.). The mean difference improves in both cases, over ocean going from 1.65 TECU (in Figure 4.19.a.) to 1.56 TECU (in Figure 4.19.b.) and over land going from 13.40 TECU (in Figure 4.19.c.) to 12.21 TECU (in Figure 4.19.d.). Therefore, the overall statistics have improved a little bit in the ascending orbit.

It can be concluded that the statistics get worse over ocean but improves over land in the descending orbit, and the overall statistics have improved a little bit in the ascending orbit.

4.3.2.3. Comparison of FRA and VTEC with other sources

The plots of the comparison between different FRA sources were reproduced. It shows the plots of the descending orbit (top) and ascending orbit (bottom) of a pixel in the center of the swath with respect to the latitude: the red line refers to L1 FRA, the green line refers to the third approach with the new thresholds, and the blue line to the core methodology with the original thresholds.

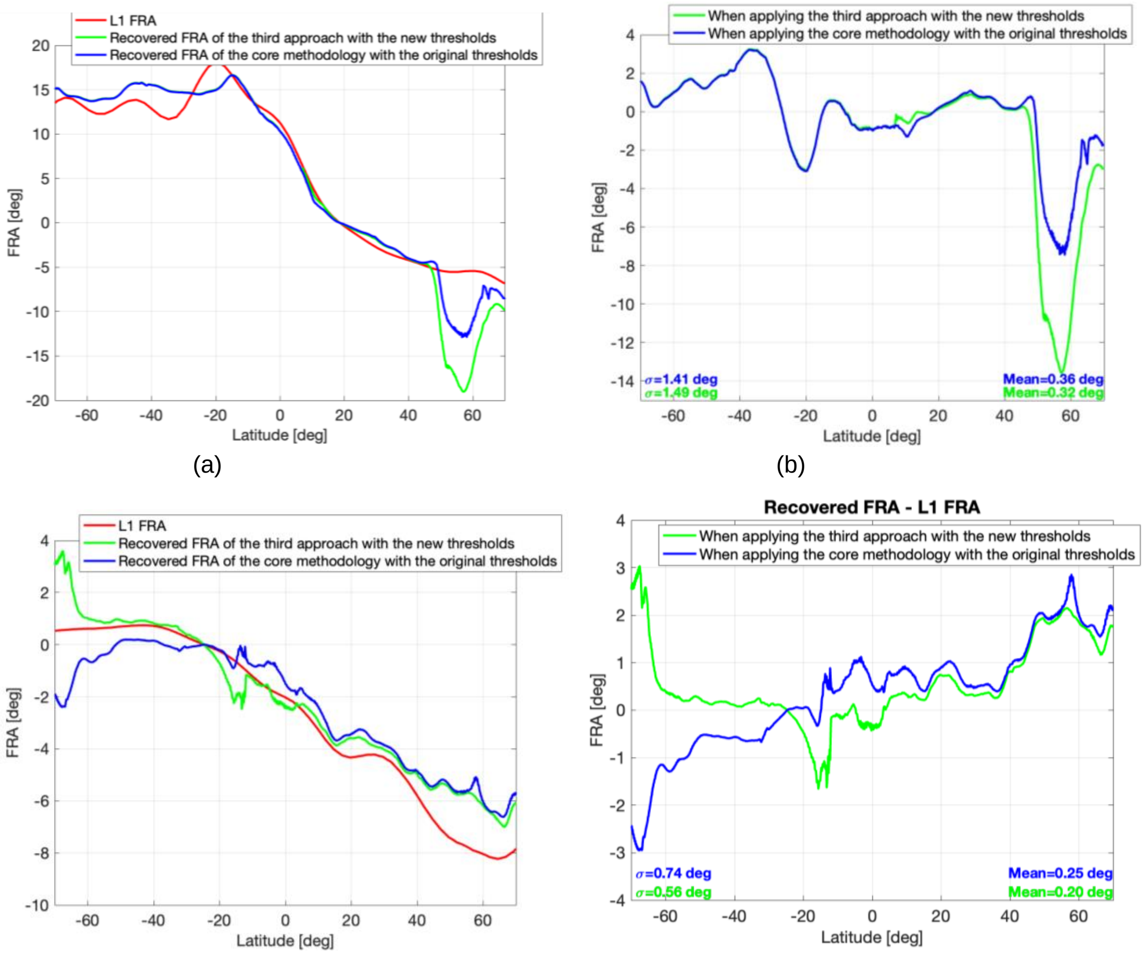

(a) (b)

(c) (d)

*Figure 4.20. Plots of the FRA vs latitude of a pixel in the center of the swath of the: TOP: **descending** orbit (a) and, (b) difference between the recovered FRA of the third approach with the new thresholds and the L1 FRA (green), and the recovered FRA of the core methodology with the original thresholds and the L1 FRA (blue). BOTTOM: **ascending** orbit (c) and, (d) difference between the recovered FRA of the third approach with the new thresholds and the L1 FRA (green), and the recovered FRA of the core methodology with the original thresholds and the L1 FRA (blue).*

As mentioned before, there is a significant impact by applying the third approach. Here it can be seen that the mean difference of the descending orbit improves, and for the ascending orbit both the STD and the mean difference improve.

Now, it will be shown the comparison of the retrieved VTEC from SMOS with other VTEC sources. It shows the plots of the descending orbit (left) and ascending orbit (right) of a pixel in the center of the swath. Where the red line refers to the L1 VTEC, the green line refers to the third approach with the new thresholds, the blue line to the core methodology with the original thresholds, the black line refers to the IGS VTEC, and the pink line to the A3TEC.

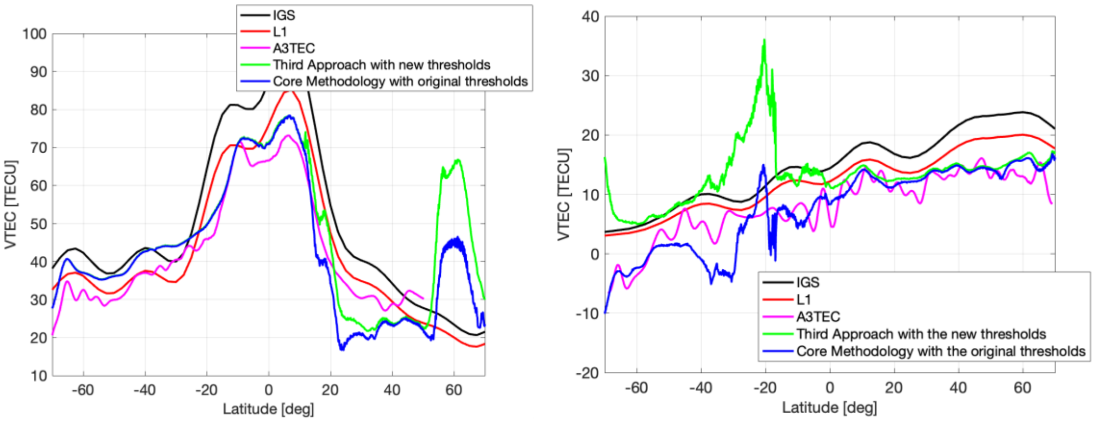

(a) (b)

Figure 4.21. Comparison of the VTEC with different sources of: (a) descending orbit, (b) ascending orbit.

As before, in Figure 4.11, it can be seen that in the ascending orbit there are no negative values of VTEC, and the recovery presents less ripples than the A3TEC. Also, it can be observed that at -20ºN there is a peak in the ascending plot, Figure 4.21.b., due to the indetermination of $\cos\Theta_B$.

4.3.3. Summary

First, an attempt was made to improve the statistics of the core methodology by trying different thresholds and comparing them with each other. An overall improvement of the statistics was obtained, accomplishing the objective. The Table 4.3 shows a summary of the new thresholds chosen for the core methodology; in the last column the result of the analysis is indicated.

Table 4.3. Summary of the new thresholds of the Core Methodology.

Core Methodology Summary								
Thresholds			**Threshold1**	**Threshold2**	**Size Temporal Filter**	**Size Spatial Filter**	**Incidence Angle**	**All Together**
Original Value			4	0.9	43	0.189	25	
New Value			**3**	**1**	**45**	**0.2**	**24**	
Descending Orbit	**Over Ocean**	**Sigma**	YES	SAME	YES	YES	YES	**YES**
		Mean difference	YES	YES	SAME	YES	YES	**YES**
	Over Land	**Sigma**	YES	YES	YES	YES	NO	**YES**
		Mean difference	NO	YES	YES	YES	YES	**YES**
Ascending Orbit	**Over Ocean**	**Sigma**	YES	SAME	YES	SAME	YES	**YES**
		Mean difference	YES	YES	SAME	YES	NO	**YES**
	Over Land	**Sigma**	YES	SAME	YES	YES	NO	**YES**
		Mean difference	YES	NO	NO	NO	YES	**YES**

Then, the statistics of the plots obtained by applying the third approach were also attempted to be improved. As mentioned before, by applying this third approach the statistics of the descending orbit over ocean improves. But for both, descending and ascending orbits, over land it worsens because a bias is being applied by only considering the positive values of VTEC. As in the core methodology the statistics have improved with the new thresholds chosen, they were applied to see if the statistics could be improved.

The Table 4.4 shows a summary of the results by having applied the same thresholds as before, in the last column the result of the analysis is indicated. It can be seen that the statistics improves over ocean but worsens over land in the descending orbits, and the overall statistics worsens a bit in the ascending orbits.

Table 4.4. Summary of the results of the Third Approach with the same Thresholds as before.

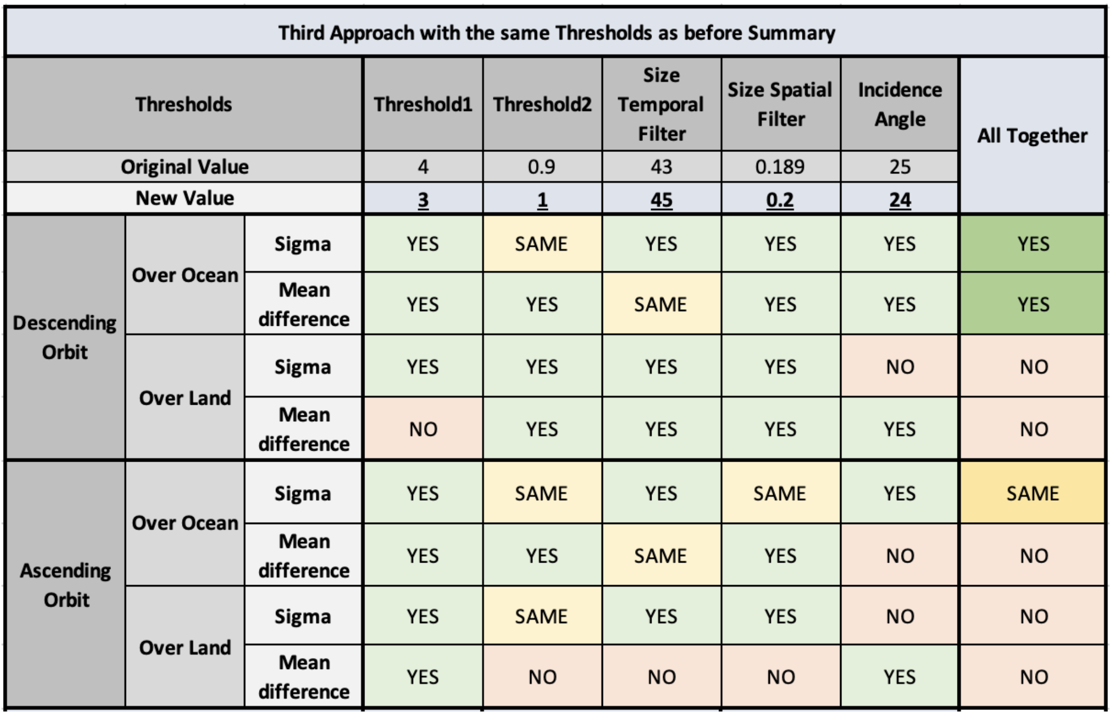

Third Approach with the same Thresholds as before Summary								
Thresholds			Threshold1	Threshold2	Size Temporal Filter	Size Spatial Filter	Incidence Angle	All Together
Original Value			4	0.9	43	0.189	25	
New Value			3	1	45	0.2	24	
Descending Orbit	Over Ocean	Sigma	YES	SAME	YES	YES	YES	YES
		Mean difference	YES	YES	SAME	YES	YES	YES
	Over Land	Sigma	YES	YES	YES	YES	NO	NO
		Mean difference	NO	YES	YES	YES	YES	NO
Ascending Orbit	Over Ocean	Sigma	YES	SAME	YES	SAME	YES	SAME
		Mean difference	YES	YES	SAME	YES	NO	NO
	Over Land	Sigma	YES	SAME	YES	YES	NO	NO
		Mean difference	YES	NO	NO	NO	YES	NO

And finally, the same procedure as the beginning was repeated to find more optimal thresholds for the third approach. By doing this, the statistics get worse over ocean but improves over land in the descending orbit, and the overall statistics have improved a little bit in the ascending orbit. The Table 4.5 shows a summary of the new thresholds chosen for the third approach; in the last column the result of the analysis is indicated.

Table 4.5. Summary of the results of the Third Approach with different Thresholds.

Third Approach with different Thresholds as before Summary								
Thresholds			Threshold1	Threshold2	Size Temporal Filter	Size Spatial Filter	Incidence Angle	All Together
Original Value			4	0.9	43	0.189	25	
New Value			5	1	45	0.175		
Descending Orbit	Over Ocean	Sigma	YES	SAME	SAME	NO	SAME	**NO**
		Mean difference	NO	SAME	NO	NO	SAME	**NO**
	Over Land	Sigma	YES	YES	YES	YES	SAME	**YES**
		Mean difference	YES	YES	YES	YES	SAME	**YES**
Ascending Orbit	Over Ocean	Sigma	SAME	SAME	YES	SAME	SAME	**YES**
		Mean difference	YES	SAME	YES	YES	SAME	**YES**
	Over Land	Sigma	NO	YES	SAME	YES	SAME	**YES**
		Mean difference	NO	YES	YES	YES	SAME	**YES**

5. Budget

The aim of this section is to describe the budget needed to carry out this project. This project has had a duration of 21 weeks, where the cost consisted of:

- A computer to be able to perform all the data processing tasks.
- The software used: a Matlab student license.
- The electricity and WiFi of the facilities used for 21 weeks (5 months).
- The worker's salary: where one person has worked 20 hours every week of the project, with a salary of 10€ per hour.

Table 5.1 Budget of the project.

Concept	**Cost**
Computer	1500 €
Matlab license	50 €
Electricity	10€ * 5 moths = 50 €
WiFi	20€ * 5 months = 100 €
Worker	4.200 €

Total Cost	**5.900 €**

6. Conclusions and future development:

This project is born from a methodology that consists of the estimation of the ionosphere VTEC of every SMOS overpass through an inversion procedure based on the measured FRA. It mitigates the effect of noise by using spatial-temporal filtering techniques and correcting the systematic error pattern when estimating the FRA and VTEC from SMOS measurements. However, there are some zones where the FRA and VTEC cannot be retrieved. This happens when the zone is contaminated by Radio Frequency Interferences (RFI), which degrade the quality of the brightness temperature. It also happens in zones of dense forest or ice because the electric field in both polarizations, horizontal and vertical, are practically equal, making the recovery of VTEC and FRA quite challenging [20].

The objective of this project is to retrieve the VTEC from SMOS Radiometric Data with the aim to better correct the FRA and to improve the quality of these maps. In order to do that, these zones where the FRA and VTEC cannot be recovered were analyzed.

First, the brightness temperature maps were reproduced to observe in detail where the FRA cannot be recovered, and the formula of the FRA was analyzed with its indeterminations. The focus was done in Canada, since it is one of those zones that cannot be recovered with the core methodology, as it is a dense forest area. It was verified that in this zone it is not possible to retrieve the FRA because it corresponds to an indetermination of the formula, having that $T_B^{xx} = T_B^{yy}$, $T_B^{hh} = T_B^{vv}$, and $T_3 = 0$.

Then, three approaches were proposed, each one with a different methodology with the aim of improving the recovered VTEC maps. The VTEC cannot have negative values, but in the core methodology some negative values appear which are then rejected when plotting them on the map, since they correspond to VTEC values that have not been correctly recovered.

- The first approach was to change the order of the core methodology. It did not work because when changing the order of some steps of the core methodology, at the moment of applying the temporal filter, it takes into account values that cause indetermination in the calculation of the FRA since the beginning. Where more negative values of the VTEC were obtained, leading to a worse result. The STD has significantly gotten worse, both in descending and ascending orbits, especially in the ocean.

- The second approach was to force the sign of the FRA and the $\cos\Theta_B$ to be equal. It did not work either because by removing the values of the solutions of the FRA that do not have the same sign as the $\cos\Theta_B$, the function takes values of solutions as good ones, that indeed are very far from the good values, obtaining values of VTEC that are all negative and out of range.

- The third approach was to directly reject the negative VTEC values. With this approach the objective was achieved in the sense that the negative values of VTEC were rejected and the VTEC could be recovered correctly, since now it does not remove values and there are not holes in the map. Also, the statistics of the descending orbit over ocean were improved. However, the statistics over land for both orbits have worsened, this is due to the fact that a bias is being applied by only considering the positive values of VTEC.

To sum up, the third approach is the one that meets the expectations, while the first two do not achieve the desired results. It is worth mentioning that the retrieval is compared to L1 VTEC only for reference, which means that these are differences and not errors.

Finally, more suitable and optimal thresholds were found in order to improve the statistics.

An attempt was made to improve the statistics of the core methodology by trying different thresholds and comparing them with each other. An overall improvement of the statistics was obtained, accomplishing the objective.

Then, the statistics of the plots obtained by applying the third approach were also attempted to be improved. As mentioned before, by applying this third approach the statistics of the descending orbit over ocean improves. But for both, descending and ascending orbits, over land it worsens because a bias is being applied by only considering the positive values of VTEC. As in the core methodology the statistics have improved with the new thresholds chosen, they were applied to see if the statistics could be improved. It was found that the statistics improved over ocean but worsened over land in the descending orbits, and the overall statistics worsened a bit in the ascending orbits.

And finally, the same procedure as the beginning was repeated to find more optimal thresholds for the third approach. By doing this, the statistics get worse over ocean but improves over land in the descending orbit, and the overall statistics have improved a little bit in the ascending orbit.

Therefore, for improving the statistics in the third approach it can be considered that there are two cases, one would be applying the same thresholds found for the core methodology and the other one would be applying the new thresholds found for the third methodology. Depending on which is the objective to be achieved, one case or the other would be applied. In other words, if what is wanted to improve is the land, it is worth applying the new thresholds found for the third approach. Because over land there are more problems with interferences and with the indeterminations of the formula (as mentioned before). But if what is wanted to improve is the ocean, it is better to keep the thresholds found for the core methodology.

For future research lines, the next steps would be to check the value of the brightness temperatures for both orbits, so if these values are small (which is what happens in the ascending orbits) it could be considered these new thresholds found for the third approach. But if the temperatures are high (which is what happens in descending orbits) it could be considered to keep the values found for the core methodology.

Bibliography:

[1] Drinkwater, M., Kerr, Y., Font, J., & Berger, M. (2009). *Exploring the Water Cycle of the "Blue Planet"* (ESA Bulletin No. 137; pp. 6–15).

[2] Silvestrin, P., Berger, M., Kerr, Y. H., & Font, J. (2001). ESA's Second Earth Explorer Opportunity Mission: The Soil Moisture and Ocean Salinity Mission – SMOS. *IEEE Geosci. Remote Sens. Lett.*, *118*, 5. https://doi.org/10.1016/j.rse.2015.12.025

[3] Corbella, I., Lin, W., Torres, F., Duffo, N., & Martín-Neira, M. (2015). Faraday Rotation Retrieval Using SMOS Radiometric Data. *IEEE Geoscience and Remote Sensing Letters*, *12*(3), 458–461. https://doi.org/10.1109/LGRS.2014.2345845

[4] Kerr, Y. H., Waldteufel, P., Wigneron, J.-P., Delwart, S., Cabot, F., Boutin, J., Escorihuela, M.- J., Font, J., Reul, N., Gruhier, C., Juglea, S. E., Drinkwater, M. R., Hahne, A., Martín-Neira, M., & Mecklenburg, S. (2010). The SMOS Mission: New Tool for Monitoring Key Elements ofthe Global Water Cycle. *Proceedings of the IEEE*, *98*(5), 666–687. https://doi.org/10.1109/JPROC.2010.2043032

[5] McMullan, K. D., Brown, M. A., Martin-Neira, M., Rits, W., Ekholm, S., Marti, J., & Lemanczyk, J. (2008). SMOS: The Payload. *IEEE Transactions on Geoscience and Remote Sensing*, *46*(3), 594–605. https://doi.org/10.1109/TGRS.2007.914809

[6] Corbella, I. (2008). ESTEC course. Interferometric Aperture Synthesis Radiometry for Earth observation.

[7] Colliander, A., Ruokokoski, L., Suomela, J., Veijola, K., Kettunen, J., Kangas, V., Aalto, A., Levander, M., Greus, H., Hallikainen, M. T., & Lahtinen, J. (2007). Development and Calibration of SMOS Reference Radiometer. *IEEE Transactions on Geoscience and Remote Sensing*, *45*(7), 1967–1977. https://doi.org/10.1109/TGRS.2007.894055

[8] Piepmeier, J. R., Johnson, J. T., Mohammed, P. N., Bradley, D., Ruf, C., Aksoy, M., Garcia, R., Hudson, D., Miles, L., & Wong, M. (2014). Radio-Frequency Interference Mitigation for the Soil Moisture Active Passive Microwave Radiometer. *IEEE Transactions on Geoscience and Remote Sensing*, *52*(1), 761–775. https://doi.org/10.1109/TGRS.2013.2281266

[9] Oliva, R., Gonzalez-Gambau, V., & Turiel, A. (2019). Assessment of SMOS RFI Mitigation by means of a Triple collocation technique. *IGARSS 2019 - 2019 IEEE International Geoscience and Remote Sensing Symposium*, 4543–4546. https://doi.org/10.1109/IGARSS.2019.8898639

[10] Martin-Neira, M., Ribo, S., & Martin-Polegre, A. J. (2002). Polarimetric mode of MIRAS. *IEEE Transactions on Geoscience and Remote Sensing*, *40*(8), 1755–1768. https://doi.org/10.1109/TGRS.2002.802489

[11] Yueh, S. H. (2000). Estimates of Faraday rotation with passive microwave polarimetry for microwave remote sensing of Earth surfaces. *IEEE Transactions on Geoscience and Remote Sensing*, *38*(5), 2434–2438. https://doi.org/10.1109/36.868900

[12] Le Vine, D. M., & Abraham, S. (2002). The effect of the ionosphere on remote sensing of sea surface salinity from space: Absorption and emission at L band. *IEEE Transactions on Geoscience and Remote Sensing*, *40*(4), 771–782. https://doi.org/10.1109/TGRS.2002.1006342

[13] Roma-Dollase, D., Hernández-Pajares, M., Krankowski, A., Kotulak, K., Ghoddousi-Fard, R., Yuan, Y., Li, Z., Zhang, H., Shi, C., Wang, C., Feltens, J., Vergados, P., Komjathy, A., Schaer, S., García-Rigo, A., & Gómez-Cama, J. M. (2018). Consistency of seven different GNSS global ionospheric mapping techniques during one solar cycle. *Journal of Geodesy*, *92*(6), 691–706. https://doi.org/10.1007/s00190-017-1088-9

[14] Vergely, J.-L., Waldteufel, P., Boutin, J., Yin, X., Spurgeon, P., & Delwart, S. (2014). New total electron content retrieval improves SMOS sea surface salinity. *Journal of Geophysical Research: Oceans*, *119*(10), 7295–7307. https://doi.org/10.1002/2014JC010150

[15] Yin, X., Boutin, J., & Spurgeon, P. (2013). Biases Between Measured and Simulated SMOS Brightness Temperatures Over Ocean: Influence of Sun. *IEEE Journal of Selected Topics in Applied Earth Observations and Remote Sensing*, *6*(3), 1341–1350. https://doi.org/10.1109/JSTARS.2013.2252602

[16] Corbella, I., Torres, F., Wu, L., Duffo, N., Duran, I., & Martín-Neira, M. (2013). Spatial biases analysis and mitigation methods in SMOS images. *2013 IEEE International Geoscience and Remote Sensing Symposium - IGARSS*, 3415–3418. https://doi.org/10.1109/IGARSS.2013.6723562

[17] Corbella, I., Torres, F., Duffo, N., González-Gambau, V., Pablos, M., Duran, I., & Martín- Neira, M. (2011). MIRAS Calibration and Performance: Results From the SMOS In-Orbit Commissioning Phase. *IEEE Transactions on Geoscience and Remote Sensing*, *49*(9), 3147–3155. https://doi.org/10.1109/TGRS.2010.2102769

[18] Rubino, R., Torres, F., Duffo, N., González-Gambau, V., Corbella, I., & Martin-Neira, M. (2017). Direct Faraday rotation angle retrieval in SMOS field of view. *2017 IEEE International Geoscience and Remote Sensing Symposium (IGARSS)*, 697–698. https://doi.org/10.1109/IGARSS.2017.8127047

[19] Rubino, R., Duffo, N., González-Gambau, V., Torres, F., Corbella, I., Durán, I., & Martín- Neira, M. (2020a). Deriving VTEC Maps from SMOS Radiometric Data. *Remote Sensing*, *12*(10), 1604. https://doi.org/10.3390/rs12101604

[20] Rubino, R., Duffo, N., & Verónica González-Gambau, U. (2022). *Program in Signal Theory and Communications*.

[21] Mecklenburg, S., Drusch, M., Kaleschke, L., Rodriguez-Fernandez, N., Reul, N., Kerr, Y., Font, J., Martin-Neira, M., Oliva, R., Daganzo-Eusebio, E., Grant, J. P., Sabia, R., Macelloni, G., Rautiainen, K., Fauste, J., de Rosnay, P., Munoz-Sabater, J., Verhoest, N., Lievens, H., Delwart, S., Crapolicchio, R., de la Fuente, A., & Kornberg, M. (2016). ESA's Soil Moisture and Ocean Salinity mission: From science to operational applications. *Remote Sensing of Environment*, *180*, 3–18. https://doi.org/10.1016/j.rse.2015.12.025

Appendices:

A. Canada

As mentioned in the section 3.3.2.1. and 3.3.2.2., the complete maps will be shown without zoom for both orbits at antenna frame and ground frame.

A.1. Complete maps of Descending orbit

A.1.1. Antenna Frame

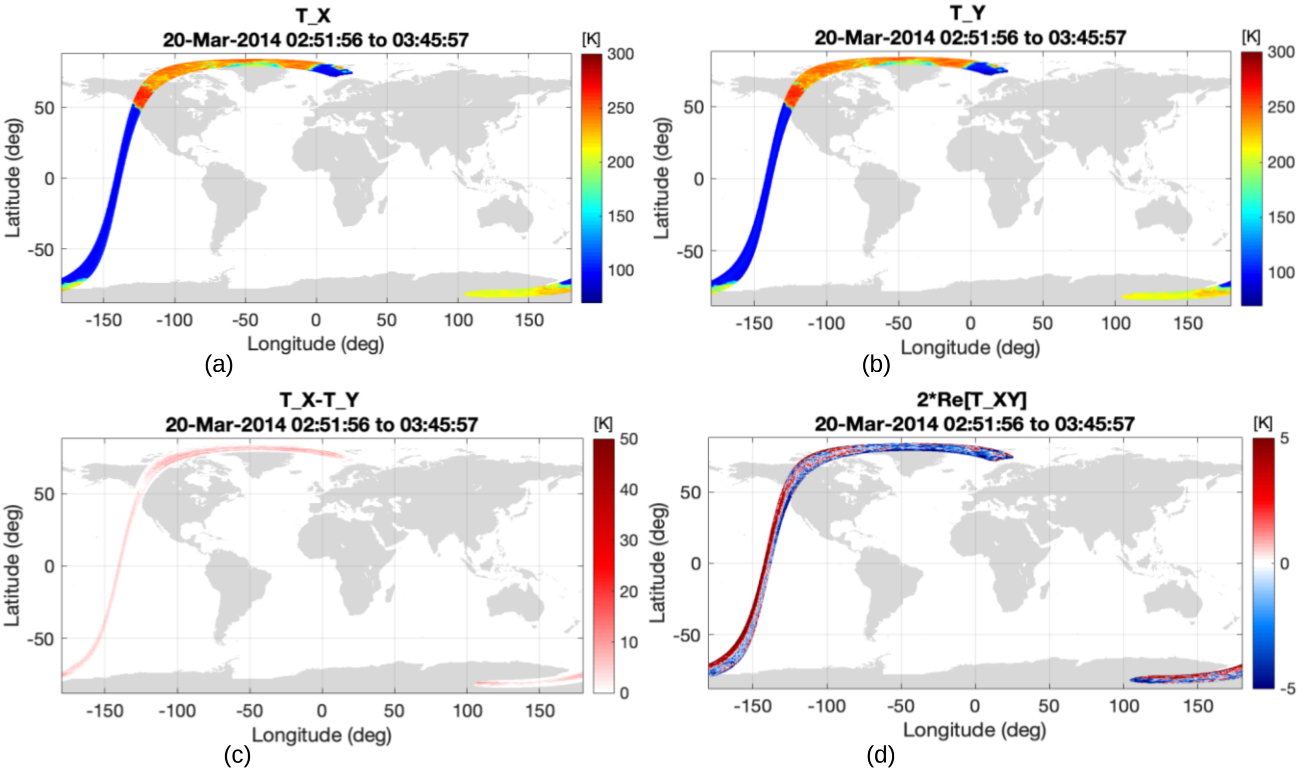

Figure A.1. Complete Brightness Temperature maps of the descending orbit at Antenna Frame of: (a) T_B^{xx}*, (b)* T_B^{yy}*, (c) Difference between* T_B^{xx} *and* T_B^{yy}*, (d)* T_3*.*

A.1.2. Ground Frame

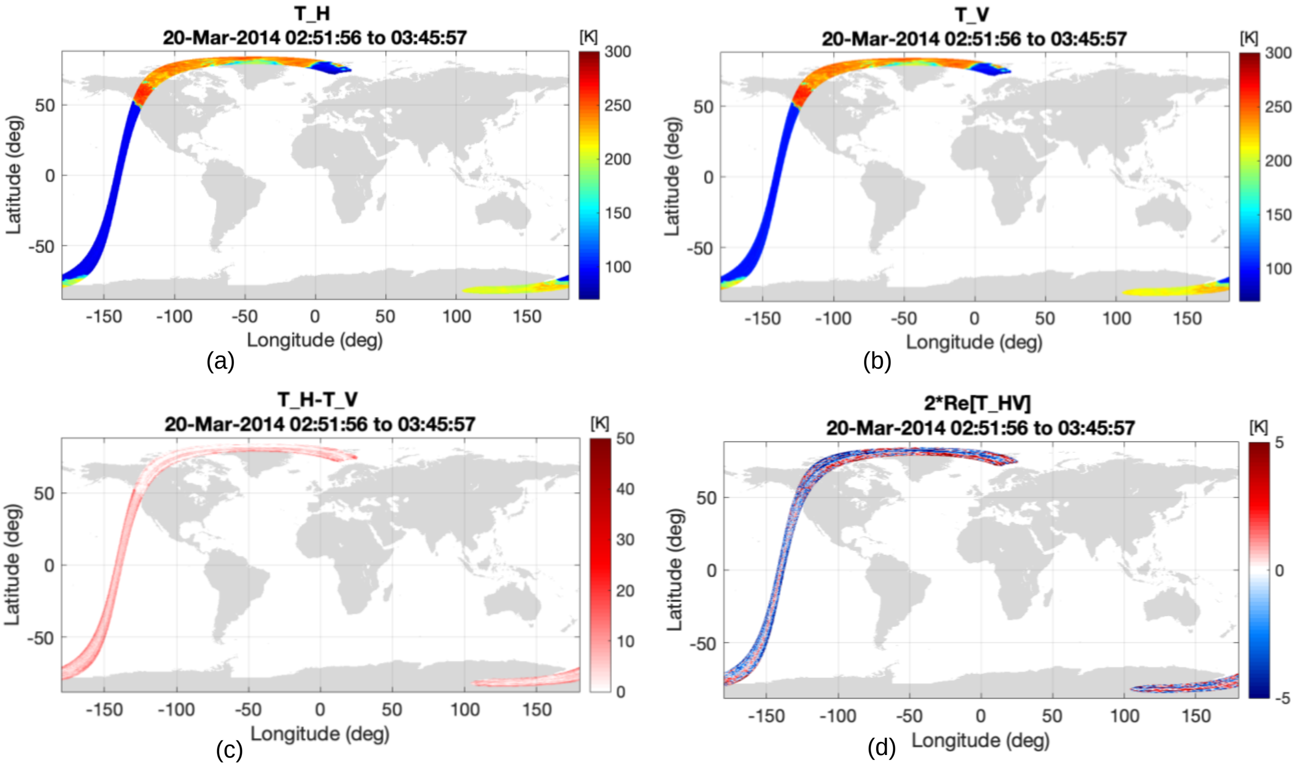

Figure A.2. Complete Brightness Temperature maps of the descending orbit at Ground Frame of: (a) T_B^{xx}, (b) T_B^{yy}, (c) Difference between T_B^{xx} and T_B^{yy}, (d) T3.

A.2. Complete maps of Ascending orbits

A.2.1. Antenna Frame

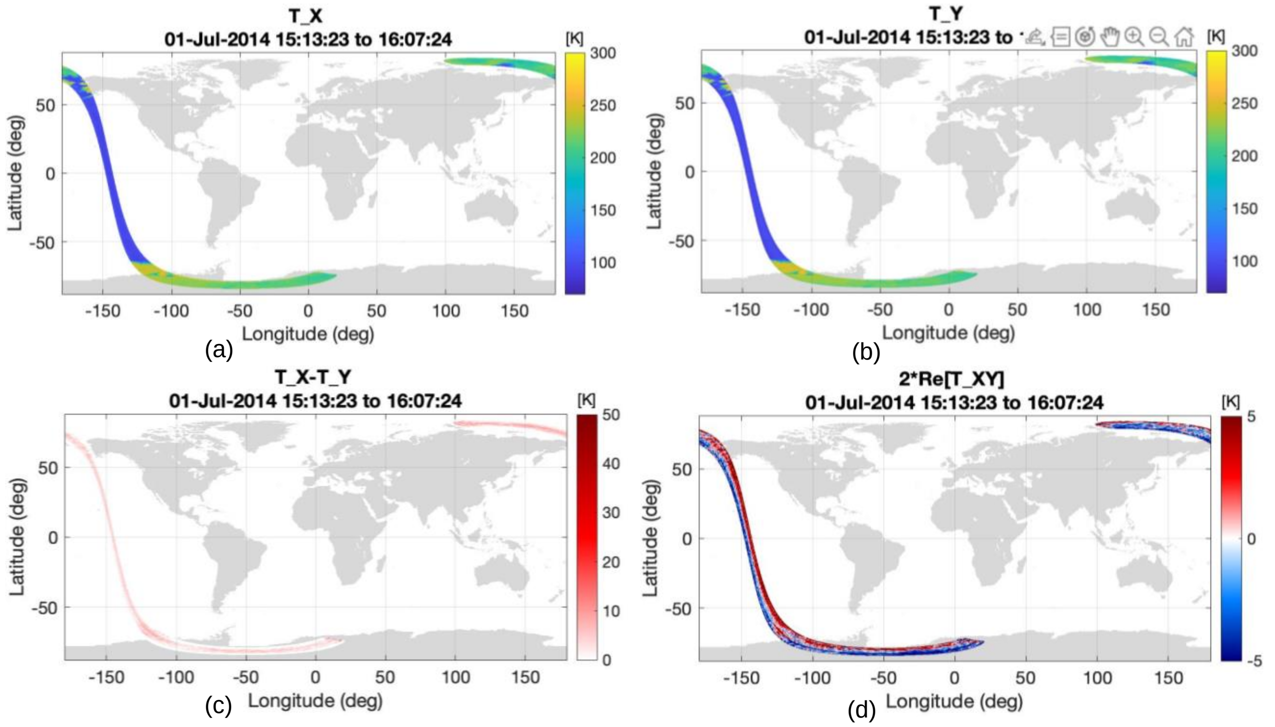

Figure A.3. Complete Brightness Temperature maps of the ascending orbit at Antenna Frame of: (a) T_B^{xx}, (b) T_B^{yy}, (c) Difference between T_B^{xx} and T_B^{yy}, (d) T3.

A.2.2. Ground Frame

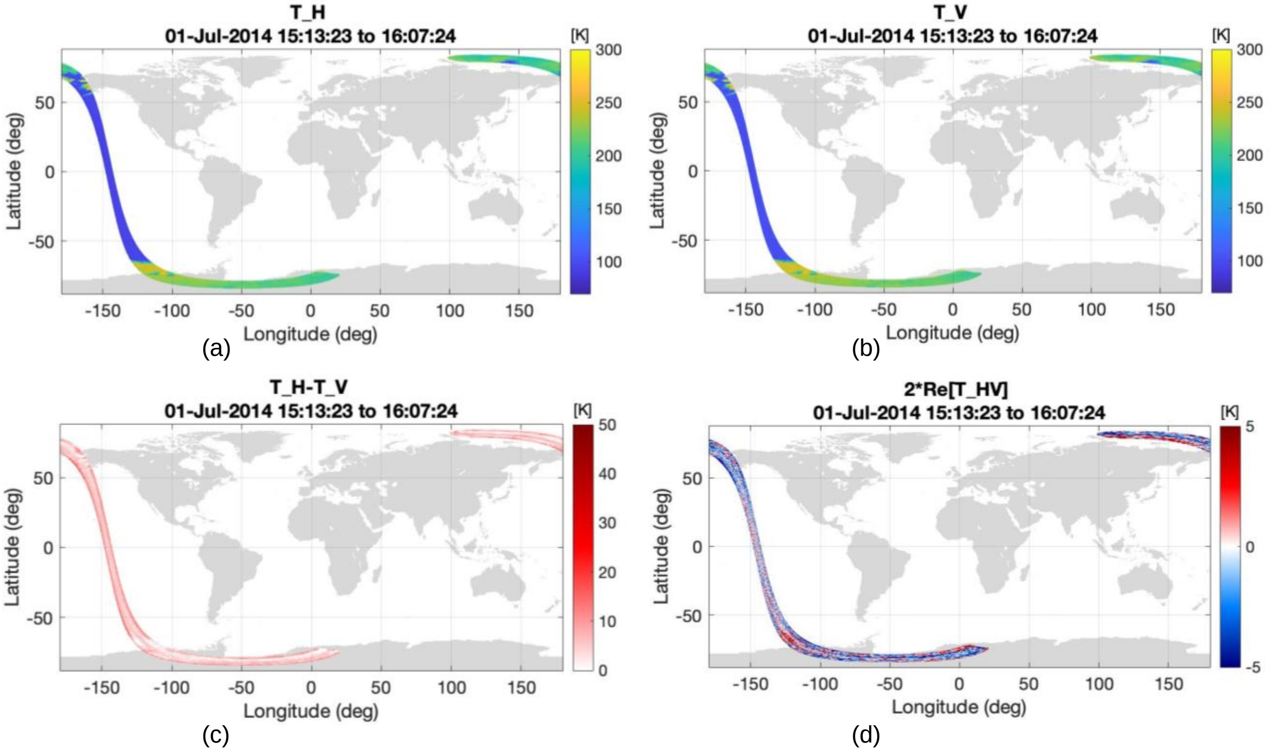

(a) (b)

(c) (d)

Figure A.4. Complete Brightness Temperature maps of the ascending orbit at Ground Frame of: (a) T_B^{xx}, (b) T_B^{yy}, (c) Difference between T_B^{xx} and T_B^{yy}, (d) T_3.

B. Thresholds

As mentioned in section 3.5., the thresholds were tested one by one with real SMOS radiometric data, in order to find the optimal value for each one of them. With the purpose of improving the error acquisition of the FRA and the VTEC by finding the most suitable thresholds in each case. The same values were tested for the two orbits. Here will be shown all the plots reproduced for each value of each threshold.

B.1. New Thresholds for the Core Methodology

B.1.1. Descending orbit

- **Threshold1**: has an original value of 4 Kelvin.
  - Threshold1 = 2:

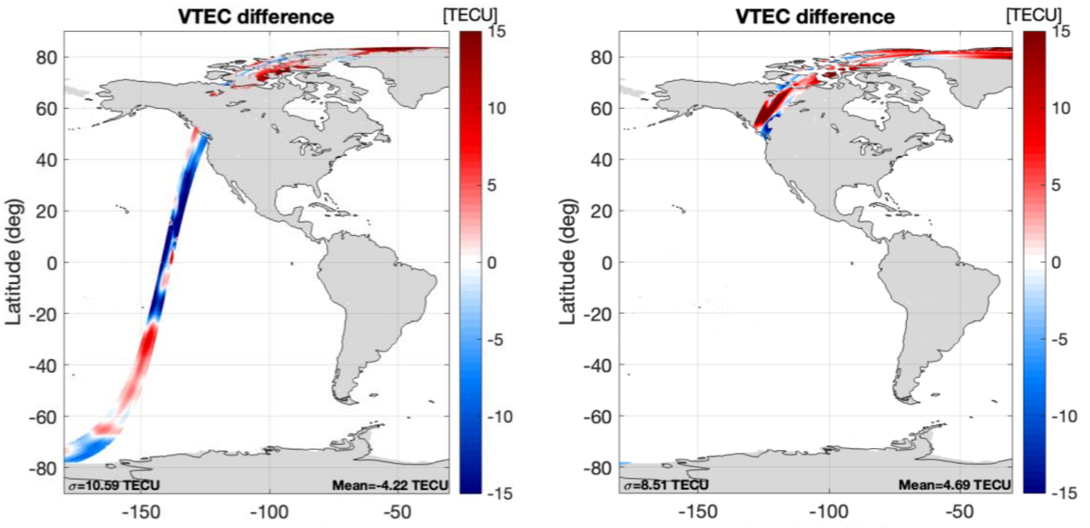

(a) (b)

Figure B.1. Difference between the recovered VTEC and the L1 VTEC snapshoots of ***descending*** *orbit of the core methodology, applying a Threshold1 = 2: (a) over ocean, (b) over land.*

- Threshold1 = 3:

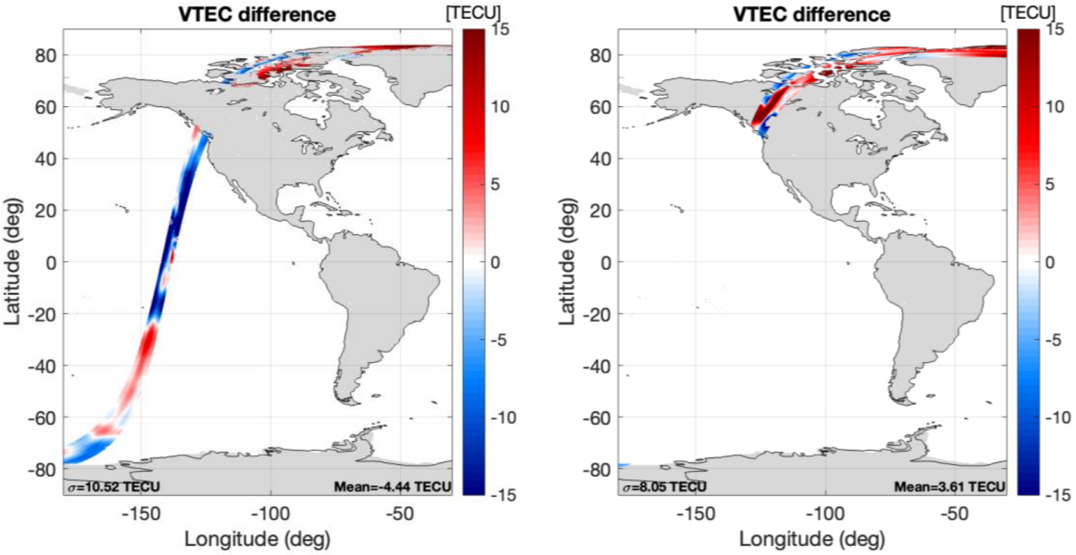

(a) (b)

Figure B.2. Difference between the recovered VTEC and the L1 VTEC snapshoots of ***descending*** *orbit of the core methodology, applying a* *Threshold1 = 3: (a) over ocean, (b) over land.*

- Threshold1 = 5:

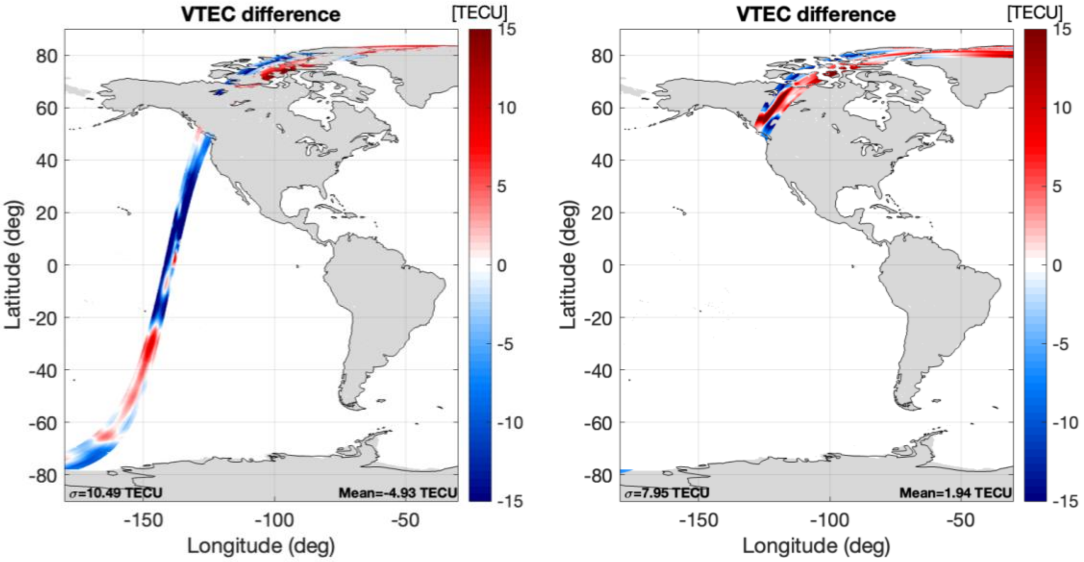

(a) (b)

Figure B.3. Difference between the recovered VTEC and the L1 VTEC snapshoots of ***descending*** *orbit of the core methodology, applying a* *Threshold1 = 5: (a) over ocean, (b) over land.*

- **Threshold2**: has an original value of 0.9 Kelvin.
  - Threshold2 = 0.5:

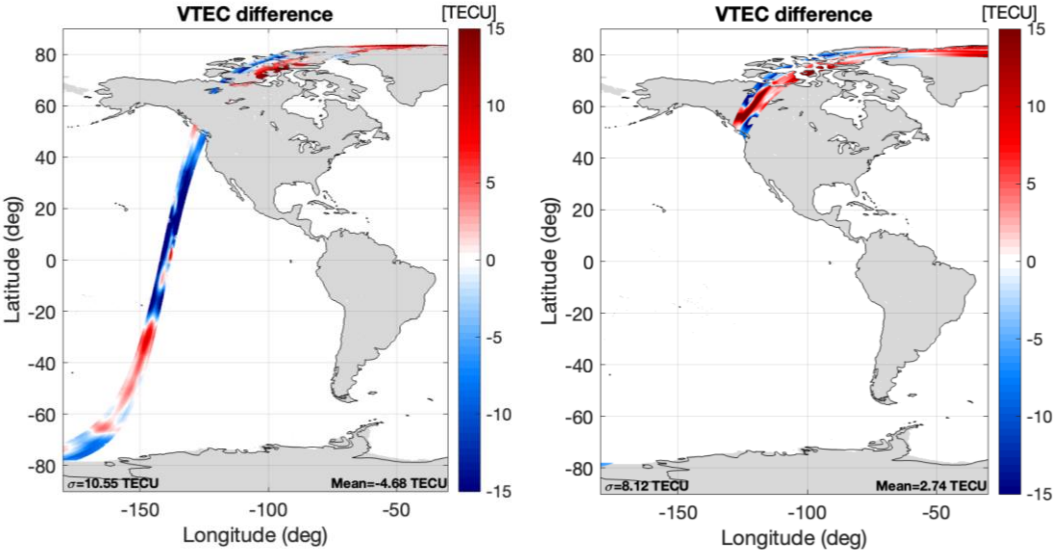

(a) (b)

*Figure B.4. Difference between the recovered VTEC and the L1 VTEC snapshoots of **descending** orbit of the core methodology, applying a Threshold2 = 0.5: (a) over ocean, (b) over land.*

  - Threshold2 = 0.8:

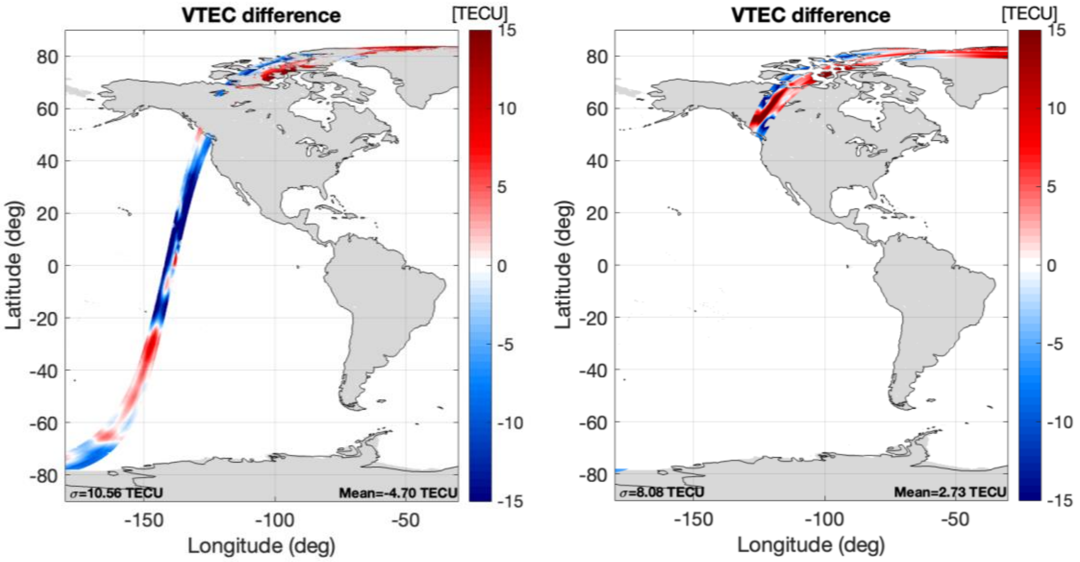

(a) (b)

*Figure B.5. Difference between the recovered VTEC and the L1 VTEC snapshoots of **descending** orbit of the core methodology, applying a Threshold2 = 0.8: (a) over ocean, (b) over land.*

- ○ <u>Threshold2 = 1</u>:

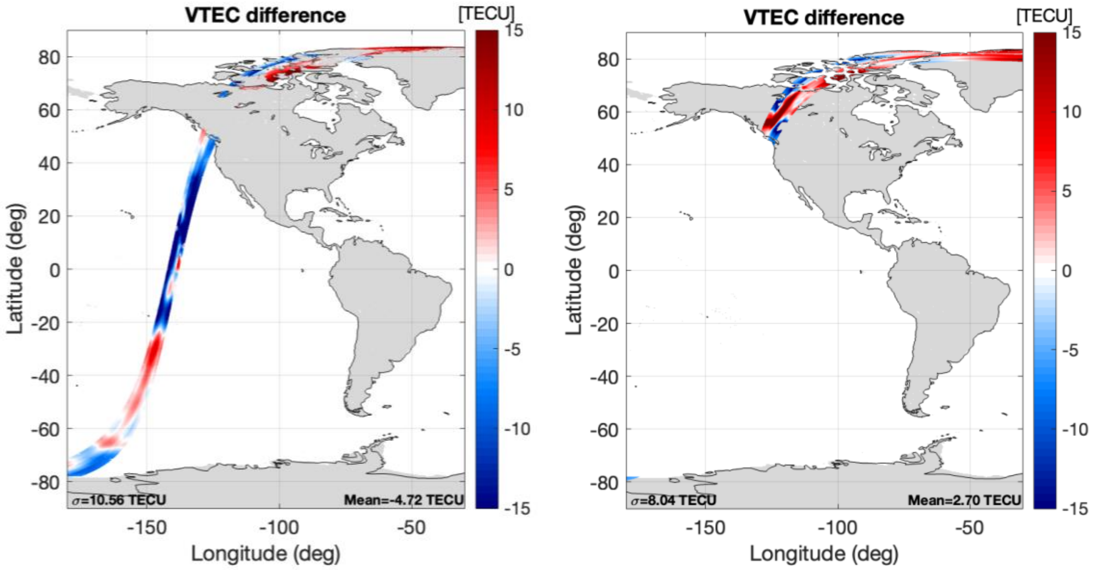

(a) (b)

*Figure B.6. Difference between the recovered VTEC and the L1 VTEC snapshoots of **descending** orbit of the core methodology, applying a <u>Threshold2 = 1</u>: (a) over ocean, (b) over land.*

- ○ Threshold2 = 1.3:

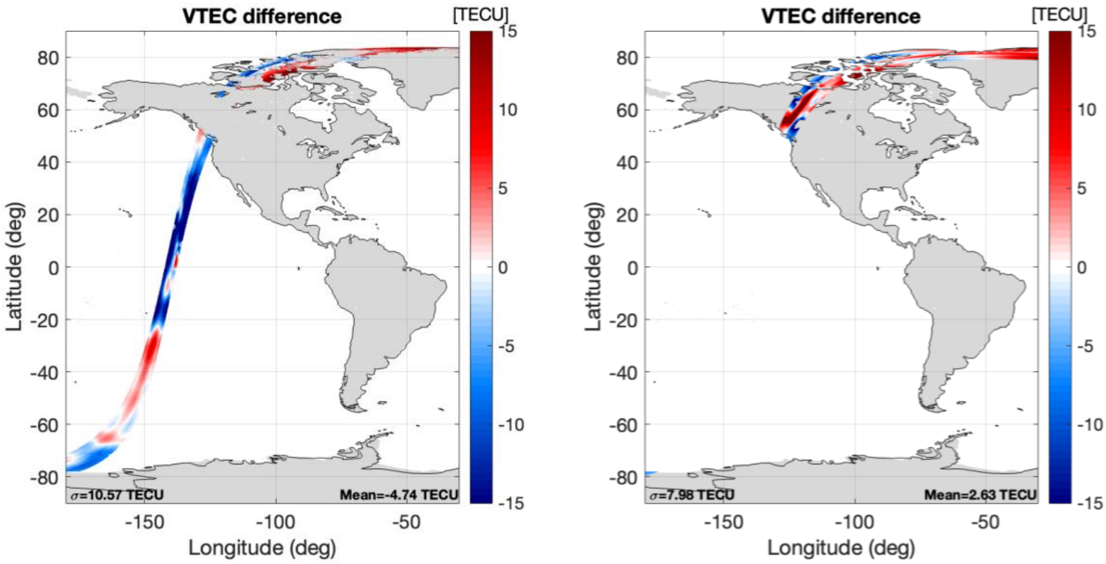

(a) (b)

*Figure B.7. Difference between the recovered VTEC and the L1 VTEC snapshoots of **descending** orbit of the core methodology, applying a <u>Threshold2 = 1.3</u>: (a) over ocean, (b) over land.*

- **Size Temporal Filter**: has an original value of 43 snapshoots.
    - Size Temporal Filter = 41:

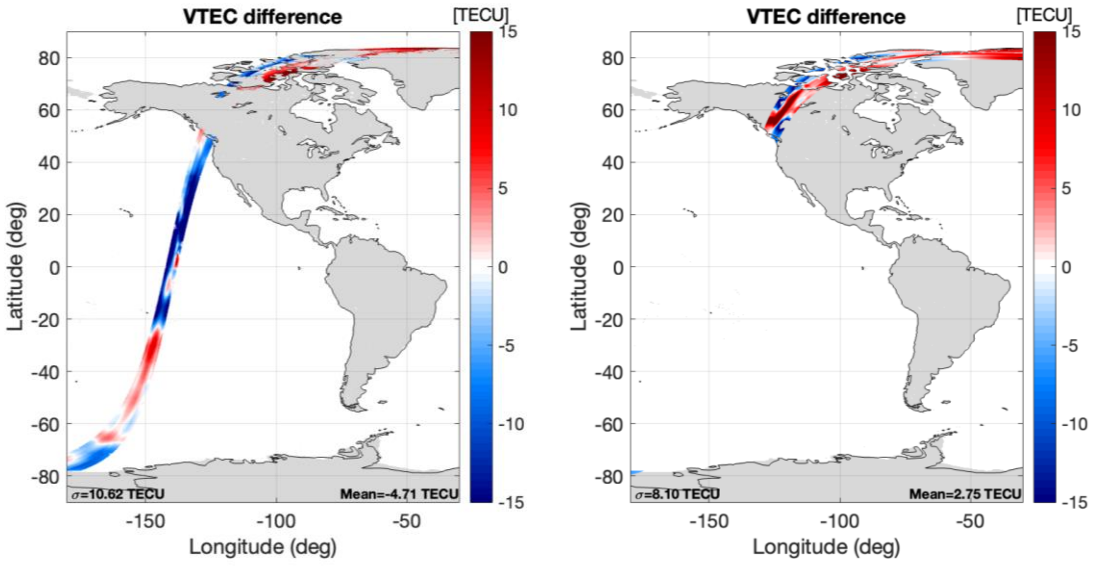

(a) (b)

Figure B.8. Difference between the recovered VTEC and the L1 VTEC snapshoots of ***descending*** *orbit of the core methodology, applying a* *Size Temporal Filter = 41: (a) over ocean, (b) over land.*

-
    - Size Temporal Filter = 45:

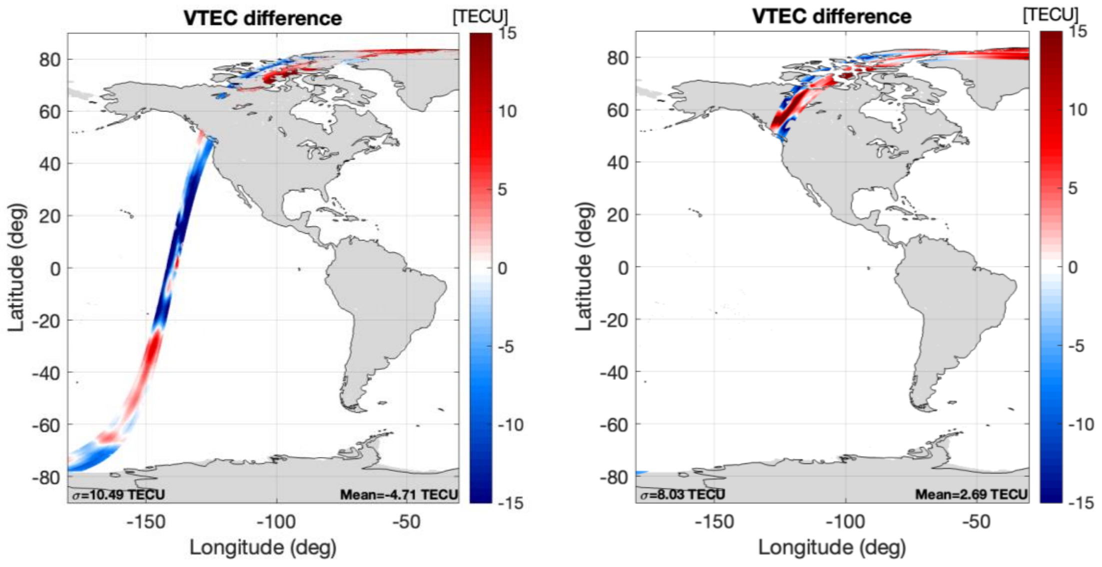

(a) (b)

Figure B.9. Difference between the recovered VTEC and the L1 VTEC snapshoots of ***descending*** *orbit of the core methodology, applying a* *Size Temporal Filter = 45: (a) over ocean, (b) over land.*

- **Size Spatial Filter**: has an original value of 0.189 d/λ.
  - Size Spatial Filer = 0.18:

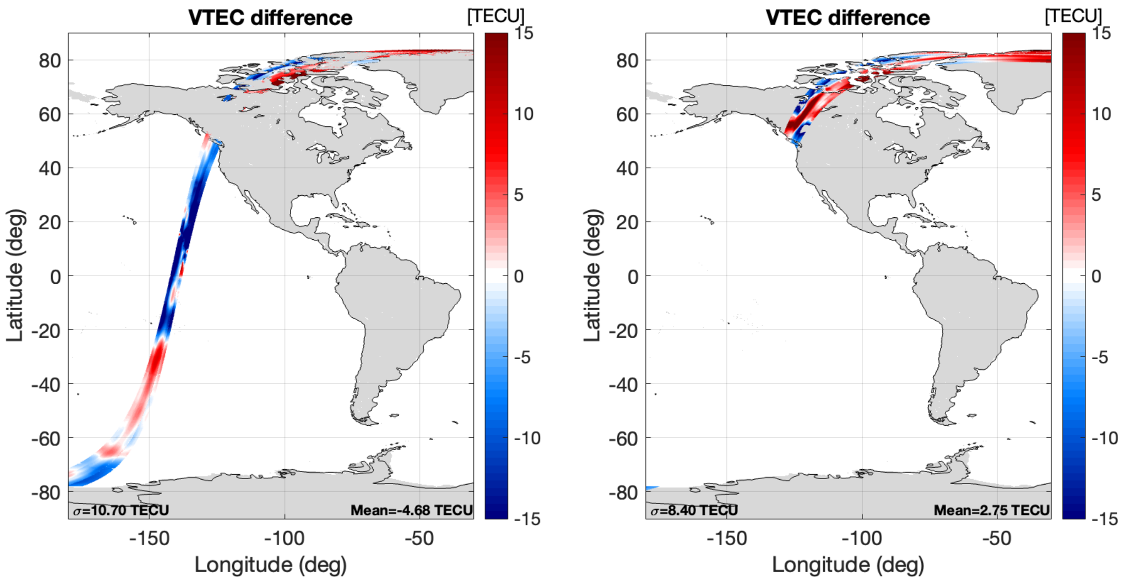

(a) (b)

Figure B.10. Difference between the recovered VTEC and the L1 VTEC snapshoots of ***descending*** *orbit of the core methodology, applying a Size Spatial Filter = 0.18: (a) over ocean, (b) over land.*

  - Size Spatial Filter = 0.195:

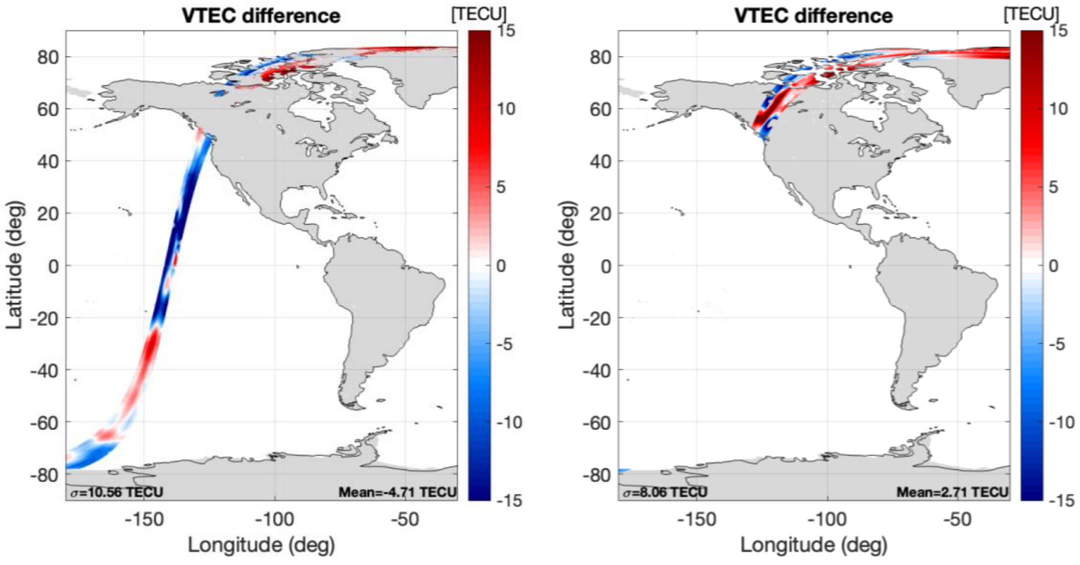

(a) (b)

Figure B.11. Difference between the recovered VTEC and the L1 VTEC snapshoots of ***descending*** *orbit of the core methodology, applying a Size Spatial Filter = 0.195: (a) over ocean, (b) over land.*

- Size Spatial Filer = 0.2:

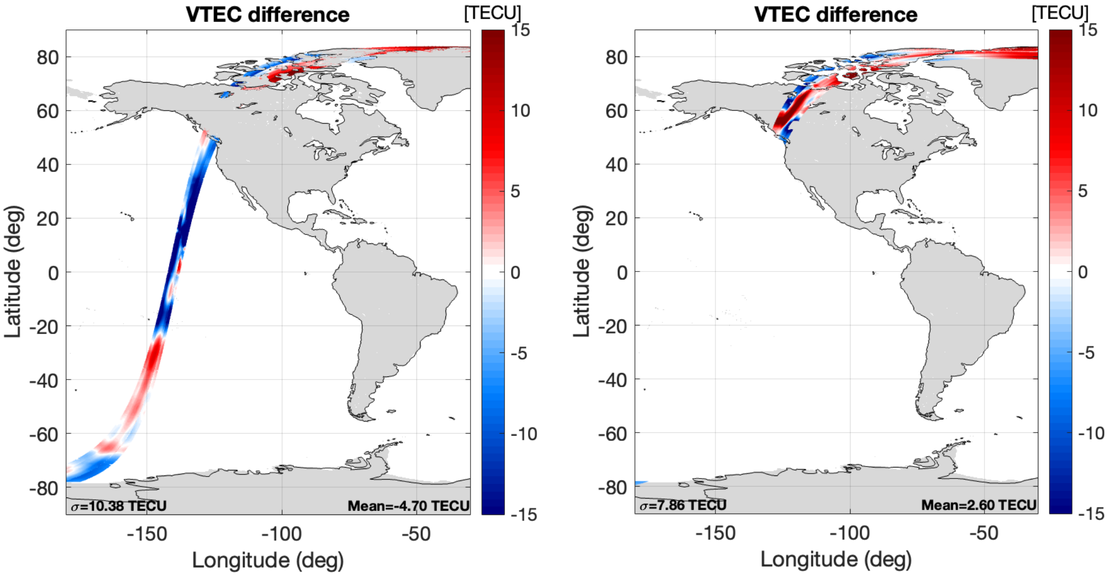

(a) (b)

Figure B.12. Difference between the recovered VTEC and the L1 VTEC snapshoots of ***descending*** *orbit of the core methodology, applying a* *<u>Size Spatial Filter = 0.2</u>: (a) over ocean, (b) over land.*

- Size Spatial Filter = 0.25:

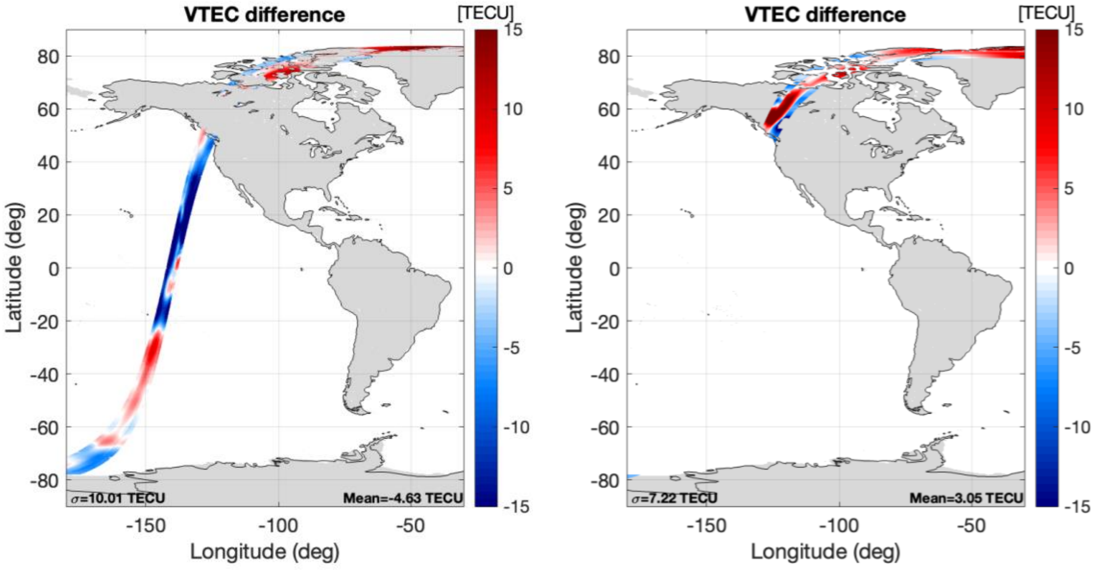

(a) (b)

Figure B.13. Difference between the recovered VTEC and the L1 VTEC snapshoots of ***descending*** *orbit of the core methodology, applying a* *<u>Size Spatial Filter = 0.25</u>: (a) over ocean, (b) over land.*

- **Incidence Angle**: has an original value of 25º.
    - Incidence Angle = 23:

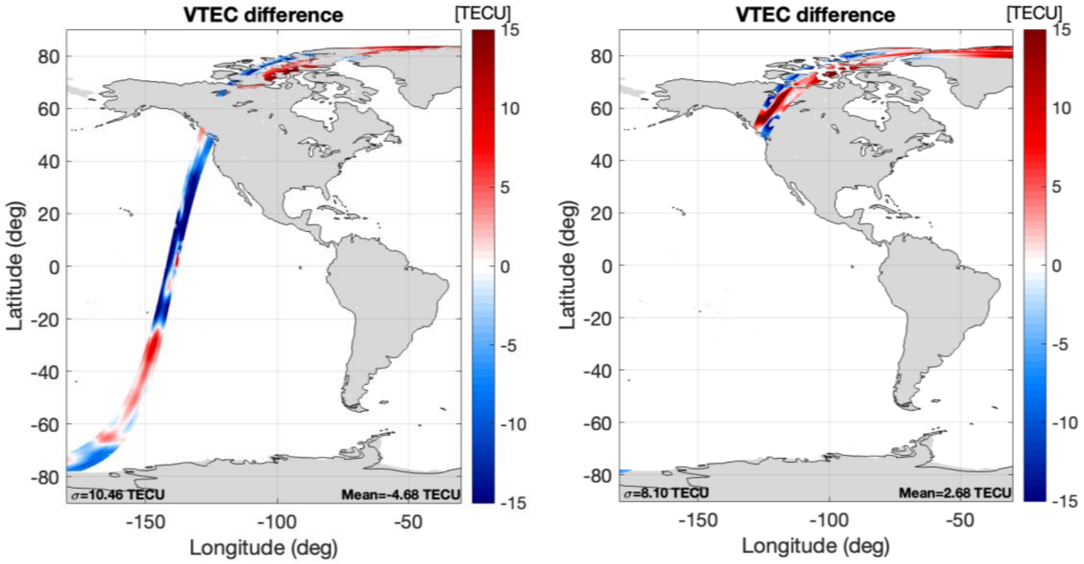

(a) (b)

*Figure B.14. Difference between the recovered VTEC and the L1 VTEC snapshoots of **descending** orbit of the core methodology, applying a Incidence Angle = 23: (a) over ocean, (b) over land.*

- Incidence Angle = 24:

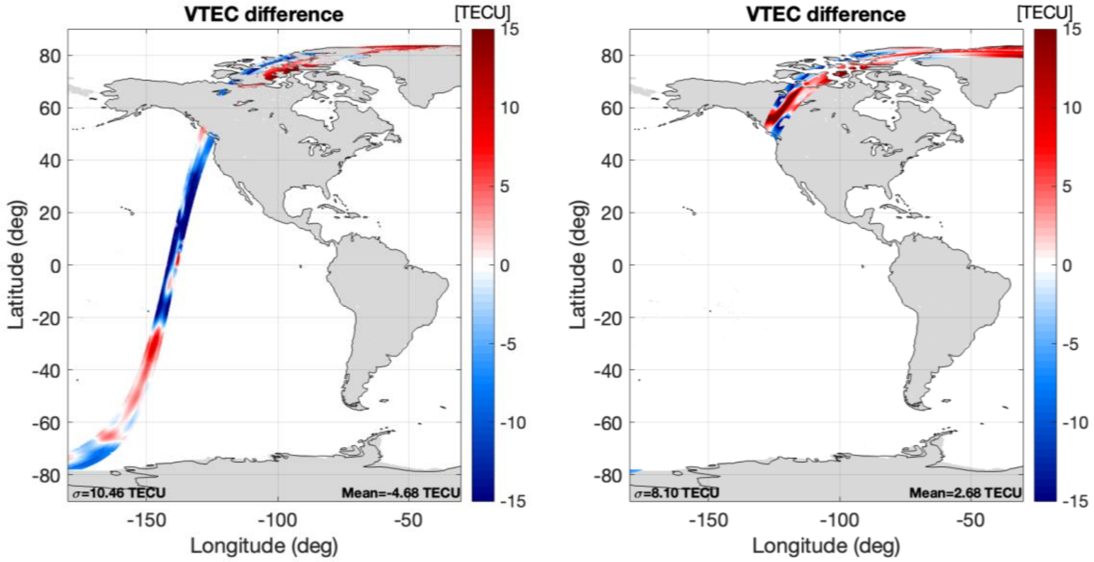

(a) (b)

*Figure B.15. Difference between the recovered VTEC and the L1 VTEC snapshoots of **descending** orbit of the core methodology, applying a Incidence Angle = 24: (a) over ocean, (b) over land.*

B.1.2. Ascending orbit

- **Threshold1**: has an original value of 4 Kelvin.
  - Threshold1 = 2:

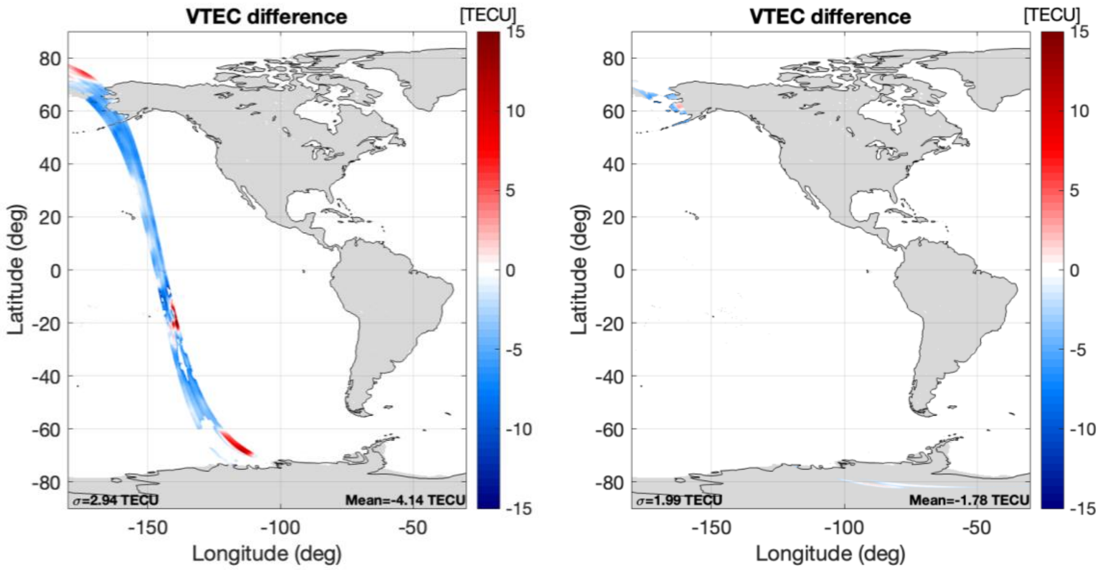

(a) (b)

Figure B.16. Difference between the recovered VTEC and the L1 VTEC snapshoots of ***ascending*** *orbit of the core methodology, applying a* *Threshold1 = 2: (a) over ocean, (b) over land.*

  - Threshold1 = 3:

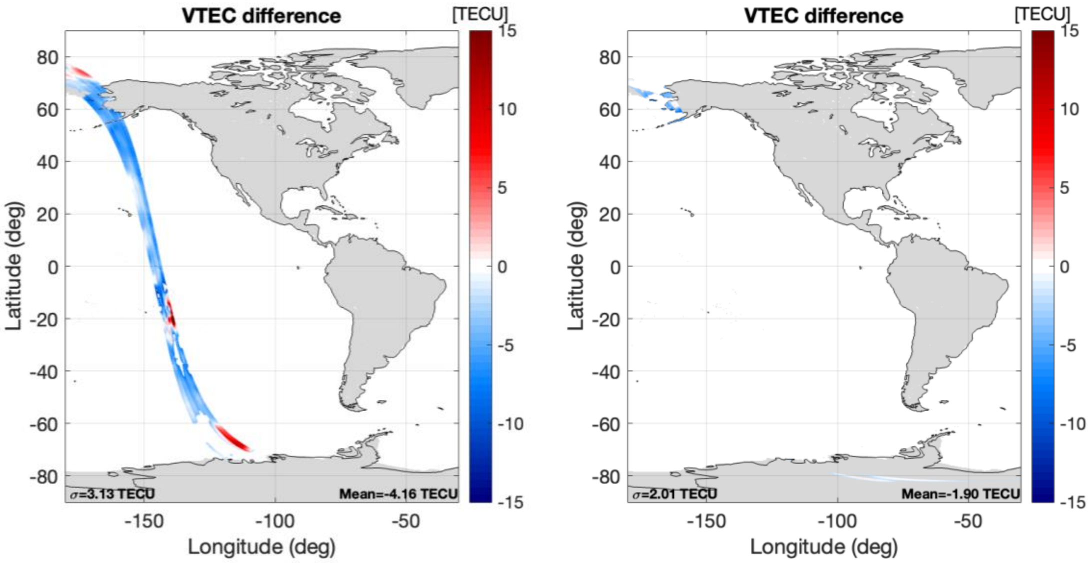

(a) (b)

Figure B.17. Difference between the recovered VTEC and the L1 VTEC snapshoots of ***ascending*** *orbit of the core methodology, applying a* *Threshold1 = 3: (a) over ocean, (b) over land.*

  - Threshold1 = 5:

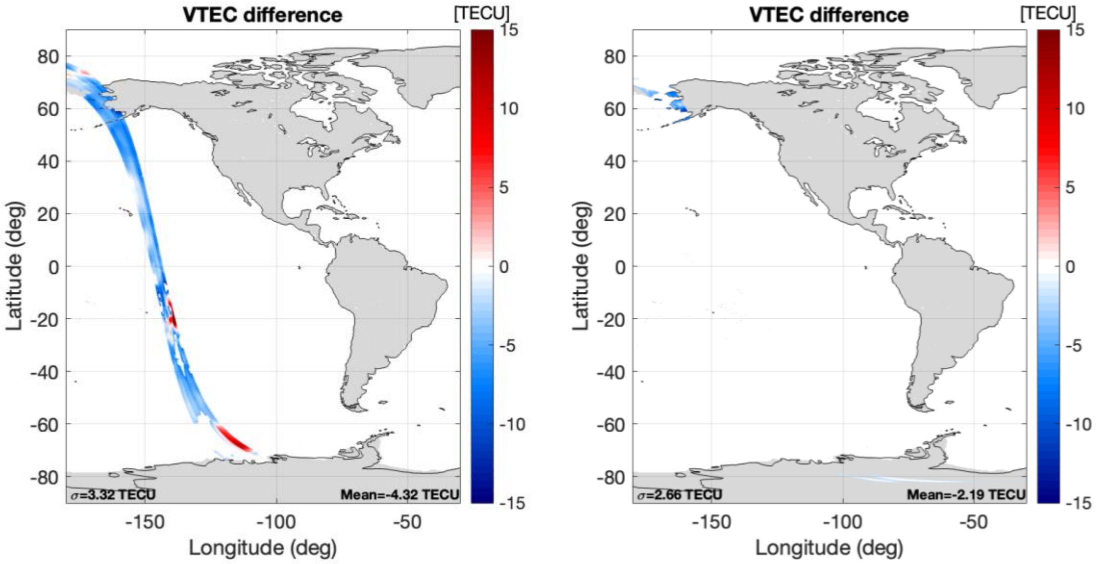

(a) (b)

Figure B.18. Difference between the recovered VTEC and the L1 VTEC snapshoots of ***ascending*** *orbit of the core methodology, applying a Threshold1 = 5: (a) over ocean, (b) over land.*

- **Threshold2**: has an original value of 0.9 Kelvin.

  - Threshold2 = 0.5:

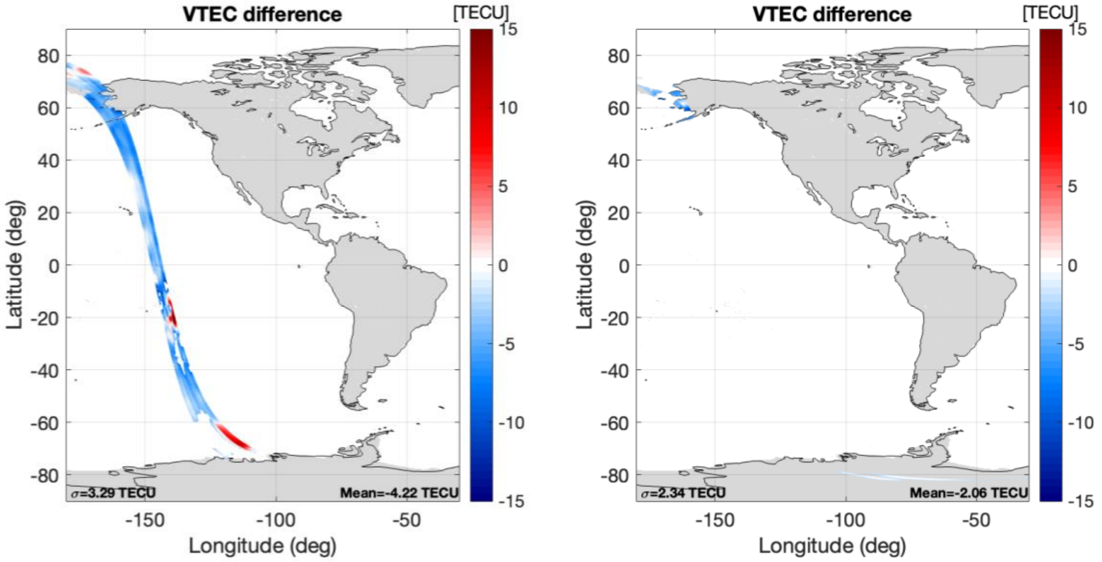

(a) (b)

Figure B.19. Difference between the recovered VTEC and the L1 VTEC snapshoots of ***ascending*** *orbit of the core methodology, applying a Threshold2 = 0.5: (a) over ocean, (b) over land.*

- <u>Threshold2 = 0.8</u>:

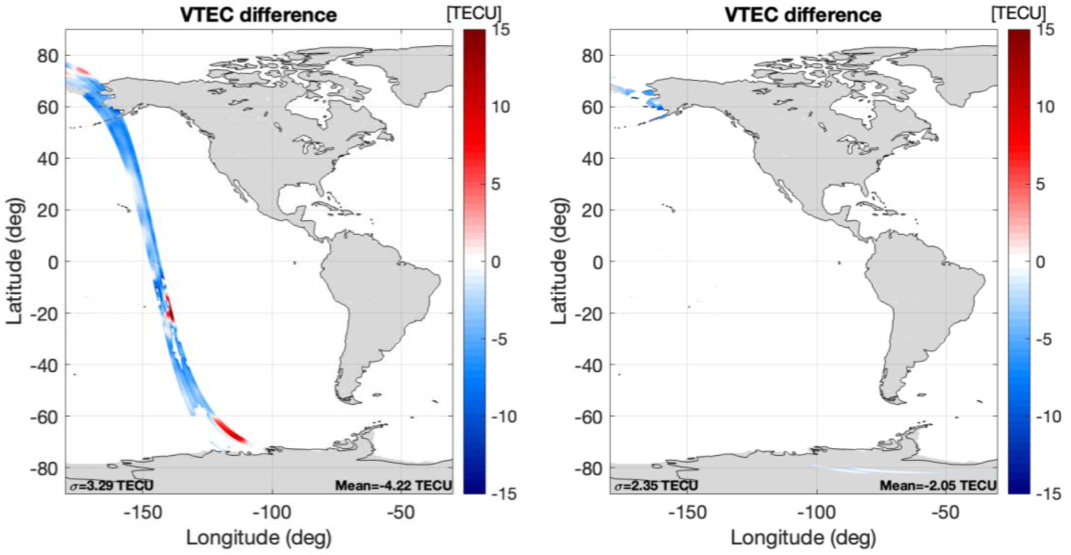

(a) (b)

*Figure B.20. Difference between the recovered VTEC and the L1 VTEC snapshoots of **ascending** orbit of the core methodology, applying a <u>Threshold2 = 0.8</u>: (a) over ocean, (b) over land.*

- <u>Threshold2 = 1</u>:

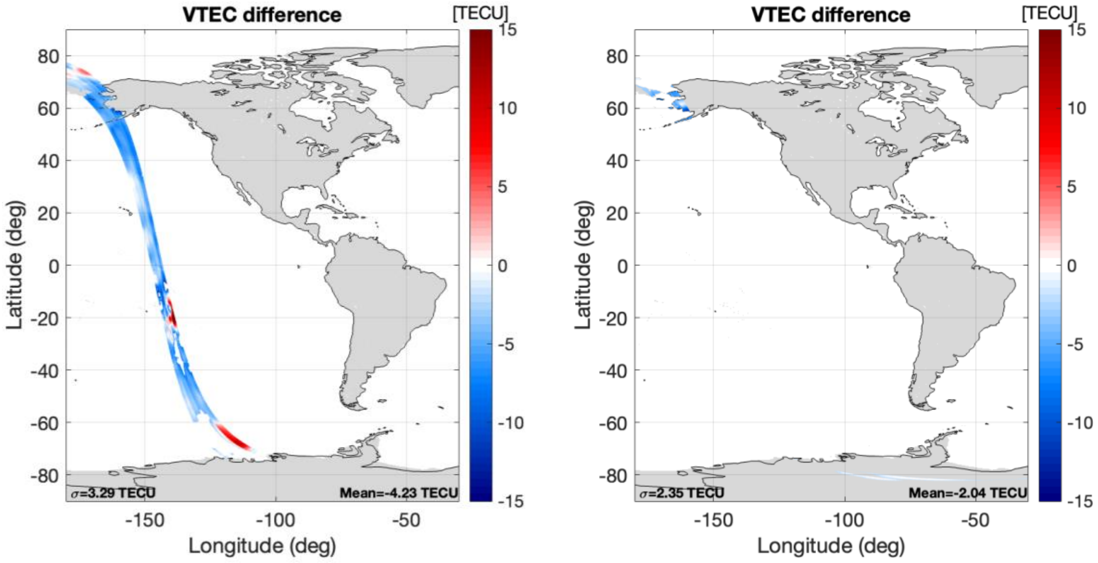

(a) (b)

*Figure B.21. Difference between the recovered VTEC and the L1 VTEC snapshoots of **ascending** orbit of the core methodology, applying a <u>Threshold2 = 1</u>: (a) over ocean, (b) over land.*

- Threshold2 = 1.3:

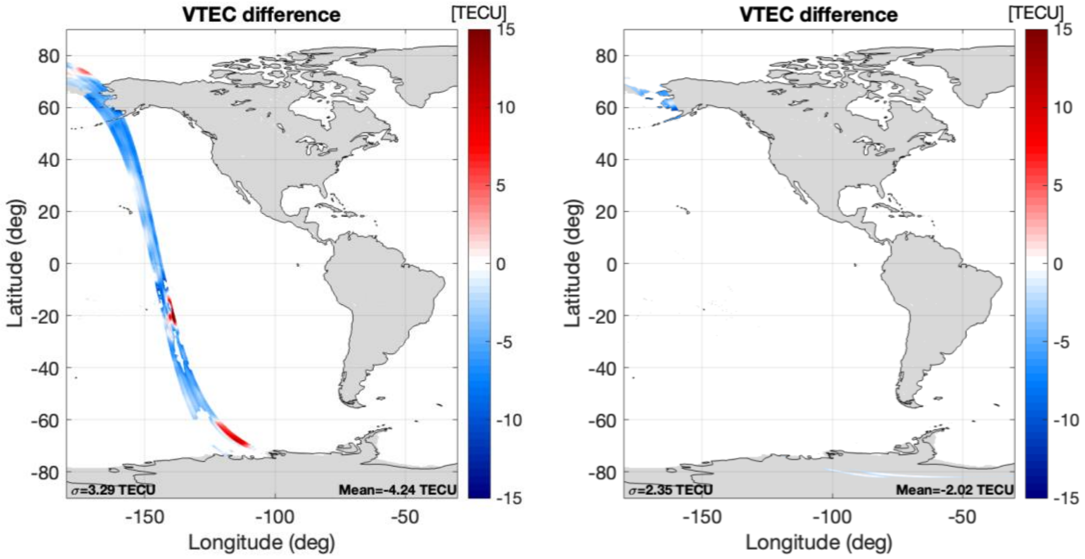

(a) (b)

Figure B.22. Difference between the recovered VTEC and the L1 VTEC snapshoots of ***ascending*** *orbit of the core methodology, applying a* *<u>Threshold2 = 1.3</u>**: (a) over ocean, (b) over land.*

- **Size Temporal Filter**: has an original value of 43 snapshoots.

  - Size Temporal Filter = 41:

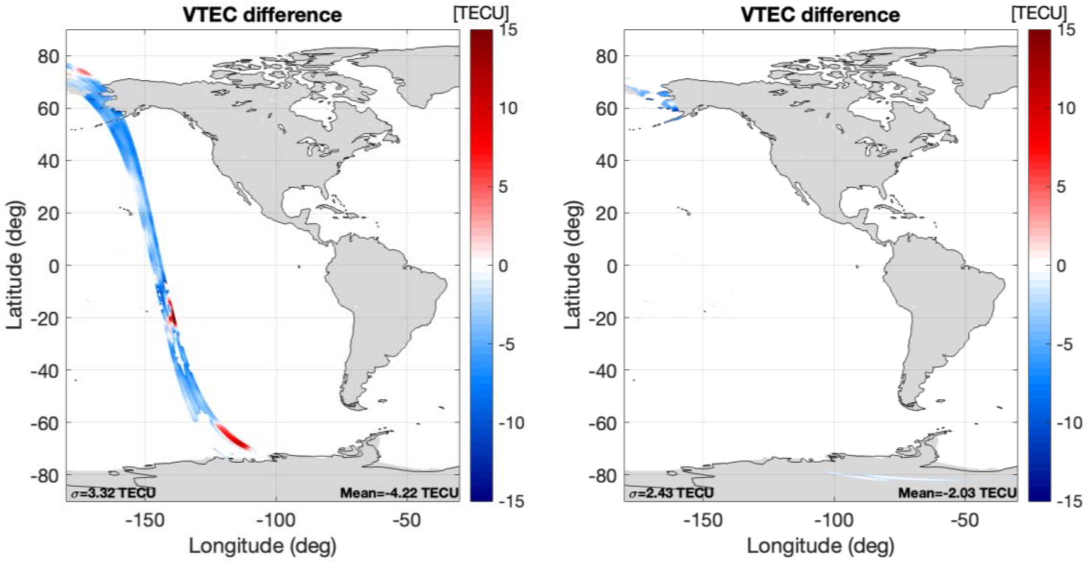

(a) (b)

Figure B.23. Difference between the recovered VTEC and the L1 VTEC snapshoots of ***ascending*** *orbit of the core methodology, applying a Size Temporal Filter = 41: (a) over ocean, (b) over land.*

- <u>Size Temporal Filter = 45</u>:

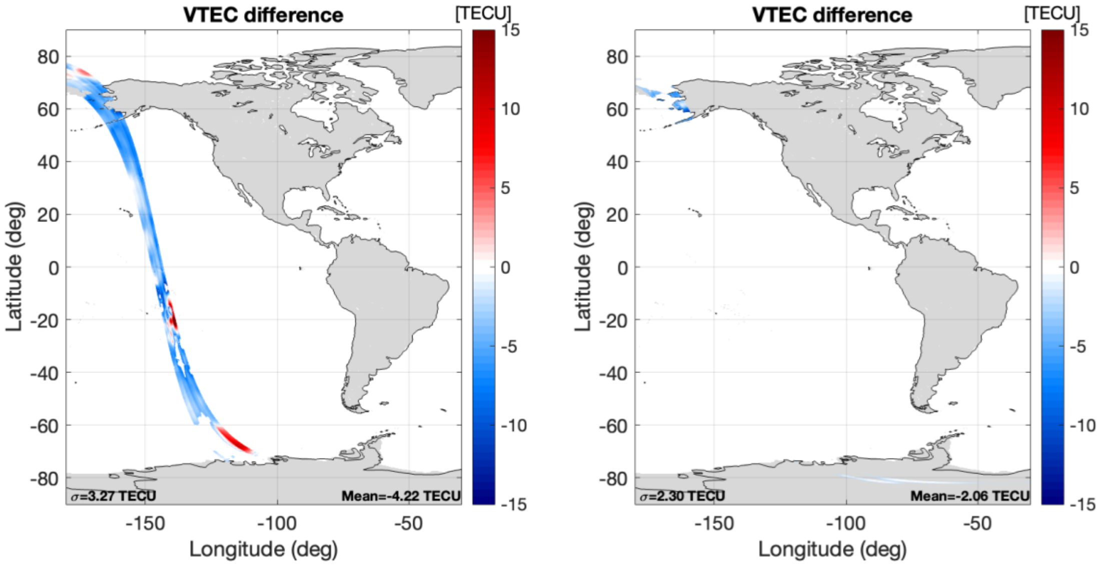

(a) (b)

*Figure B.24. Difference between the recovered VTEC and the L1 VTEC snapshoots of **ascending** orbit of the core methodology, applying a <u>Size Temporal Filter = 45</u>: (a) over ocean, (b) over land.*

- **<u>Size Spatial Filter</u>**: has an original value of 0.189 d/λ.

  - <u>Size Spatial Filer = 0.18</u>:

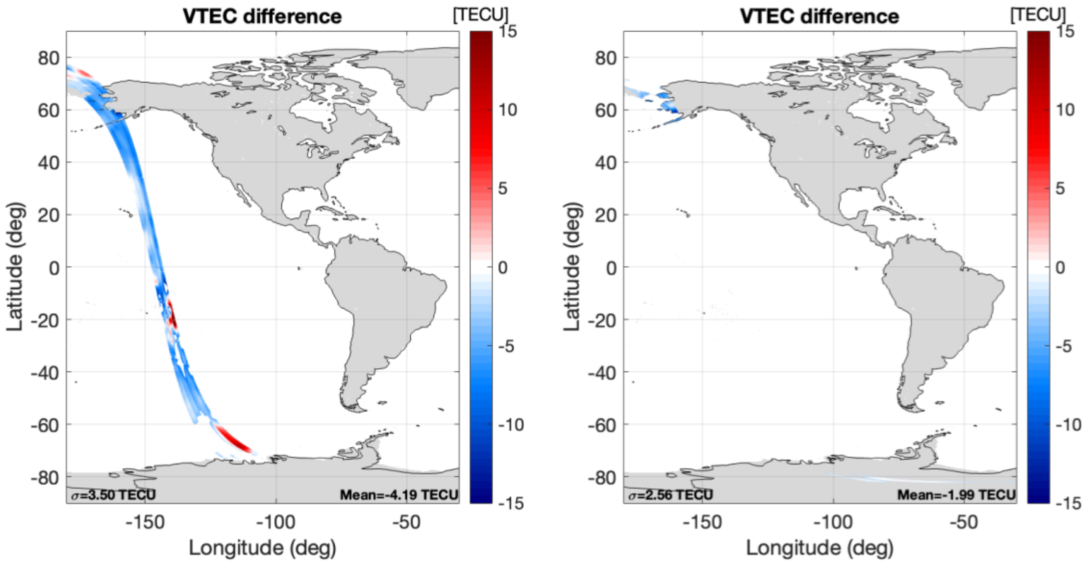

(a) (b)

*Figure B.25. Difference between the recovered VTEC and the L1 VTEC snapshoots of **ascending** orbit of the core methodology, applying a <u>Size Spatial Filter = 0.18</u>: (a) over ocean, (b) over land.*

- Size Spatial Filter = 0.195:

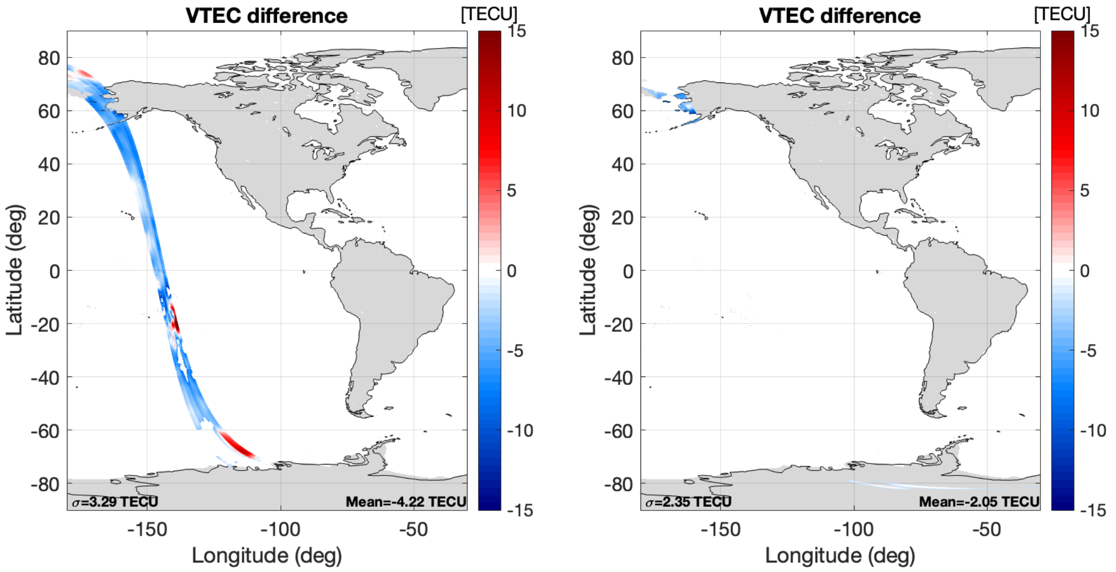

(a) (b)

*Figure B.26. Difference between the recovered VTEC and the L1 VTEC snapshoots of **ascending** orbit of the core methodology, applying a <u>Size Spatial Filter = 0.195</u>: (a) over ocean, (b) over land.*

- Size Spatial Filer = 0.2:

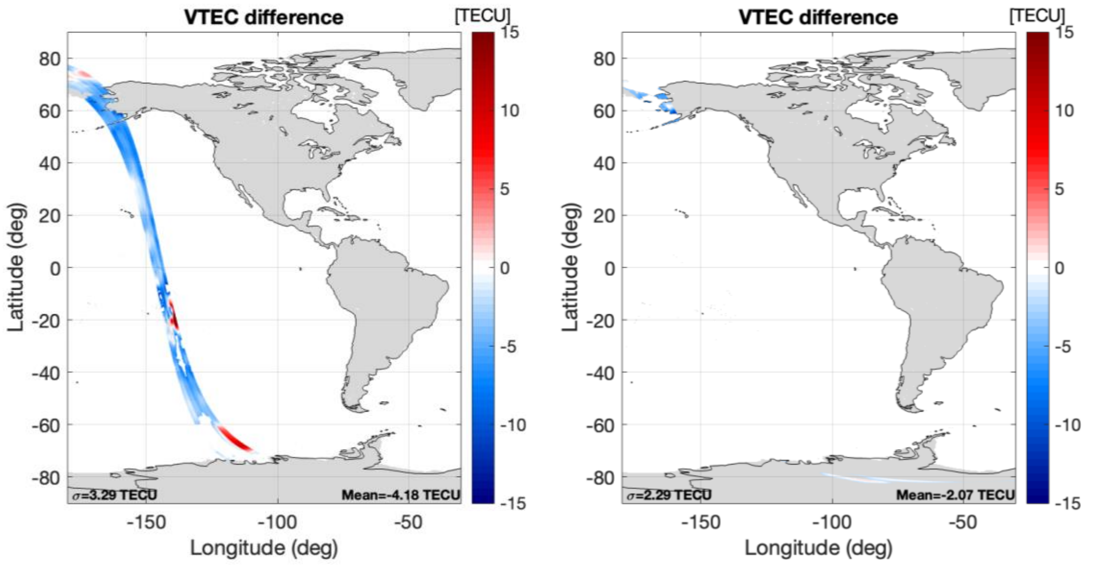

(a) (b)

*Figure B.27. Difference between the recovered VTEC and the L1 VTEC snapshoots of **ascending** orbit of the core methodology, applying a <u>Size Spatial Filter = 0.2</u>: (a) over ocean, (b) over land.*

- <u>Size Spatial Filter = 0.25</u>:

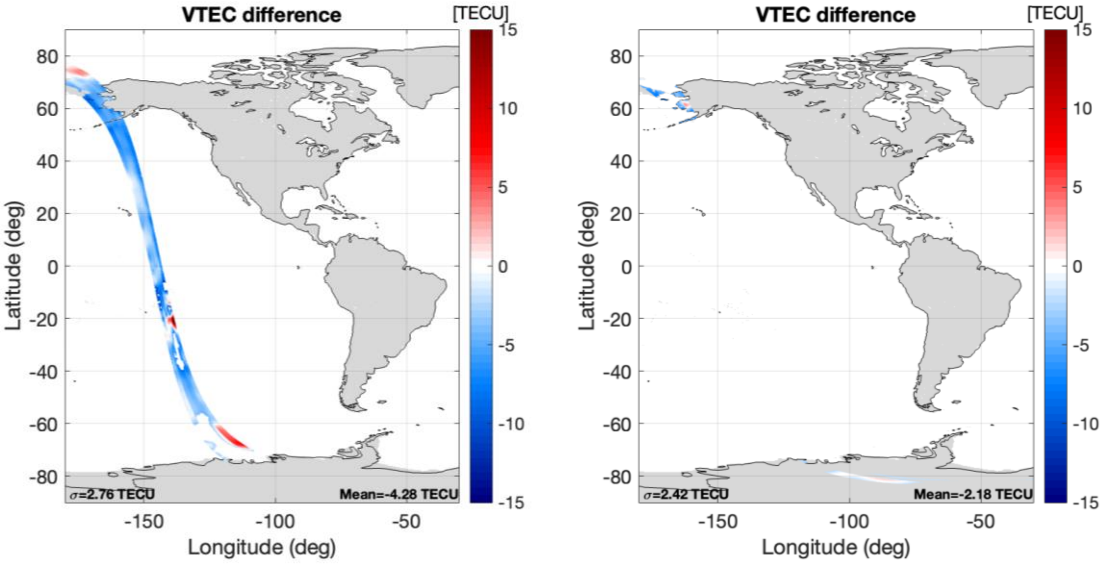

(a) (b)

*Figure B.28. Difference between the recovered VTEC and the L1 VTEC snapshoots of **ascending** orbit of the core methodology, applying a <u>Size Spatial Filter = 0.25</u>: (a) over ocean, (b) over land.*

- **<u>Incidence Angle</u>**: has an original value of 25º.

  - <u>Incidence Angle = 23</u>:

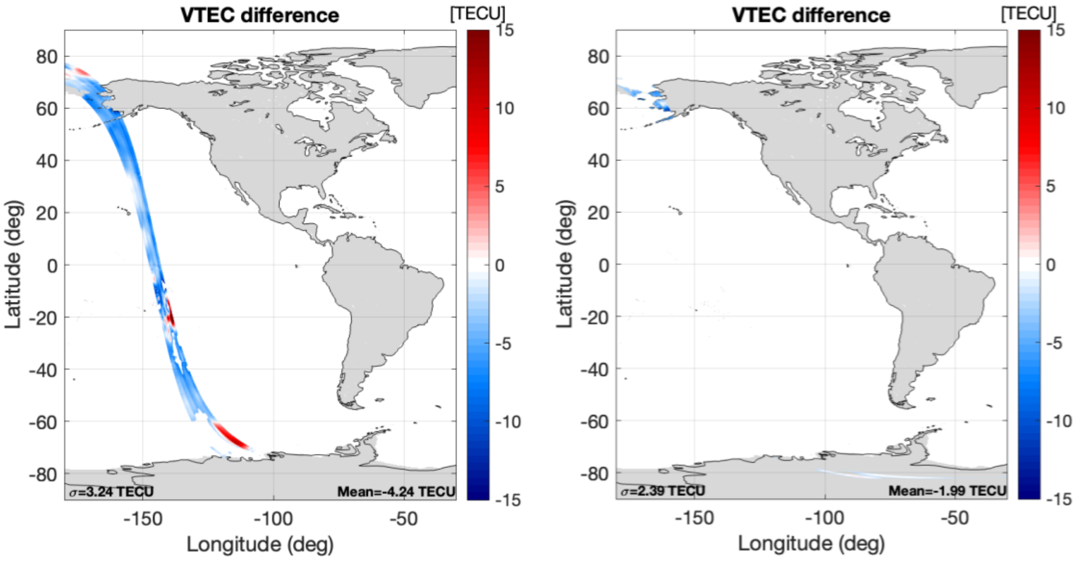

(a) (b)

*Figure B.29. Difference between the recovered VTEC and the L1 VTEC snapshoots of **ascending** orbit of the core methodology, applying a <u>Incidence Angle = 23</u>: (a) over ocean, (b) over land.*

- <u>Incidence Angle = 24</u>:

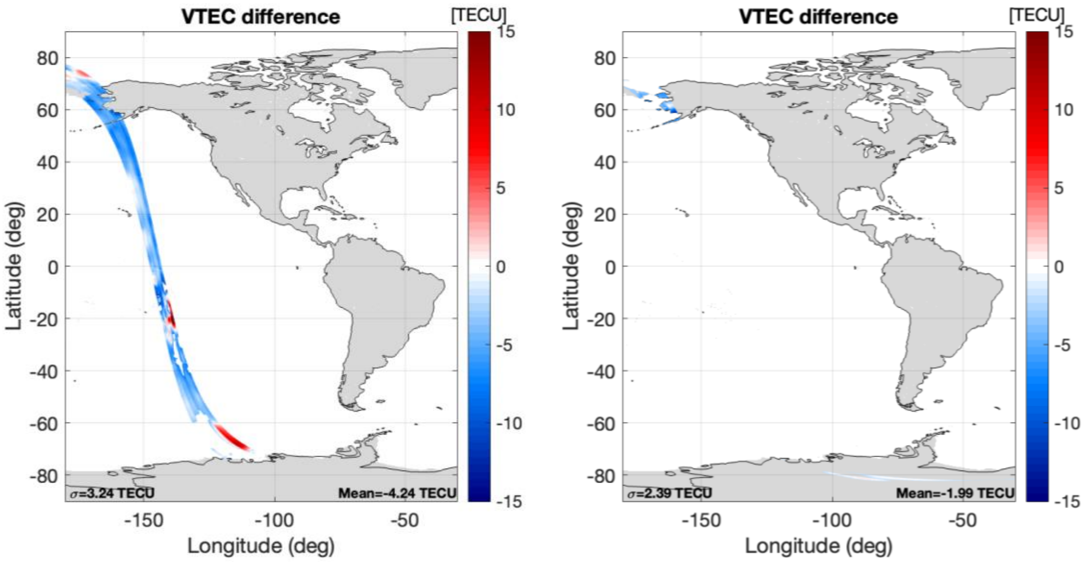

(a) (b)

Figure B.30. Difference between the recovered VTEC and the L1 VTEC snapshoots of ***ascending*** *orbit of the core methodology, applying a <u>Incidence Angle = 24</u>: (a) over ocean, (b) over land.*

B.2. <u>New thresholds for the Third Approach</u>

B.2.1. Descending orbit

- <u>**Threshold1**</u>: has an original value of 4 Kelvin.
  - <u>Threshold1 = 2</u>:

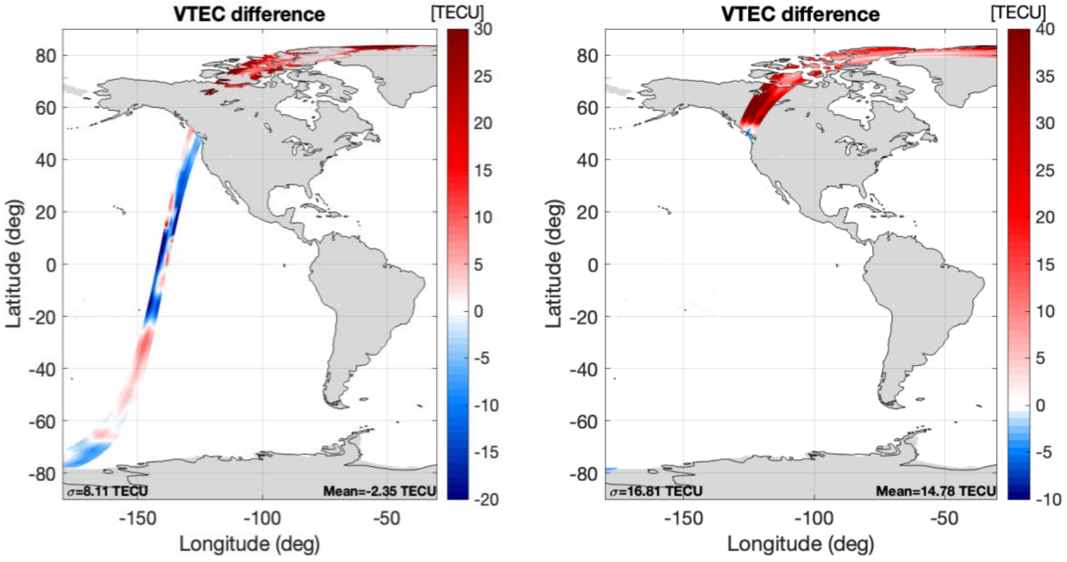

(a) (b)

Figure B.31. Difference between the recovered VTEC and the L1 VTEC snapshoots of ***descending*** *orbit of the core methodology, applying a <u>Threshold1 = 2</u>: (a) over ocean, (b) over land.*

- Threshold1 = 3:

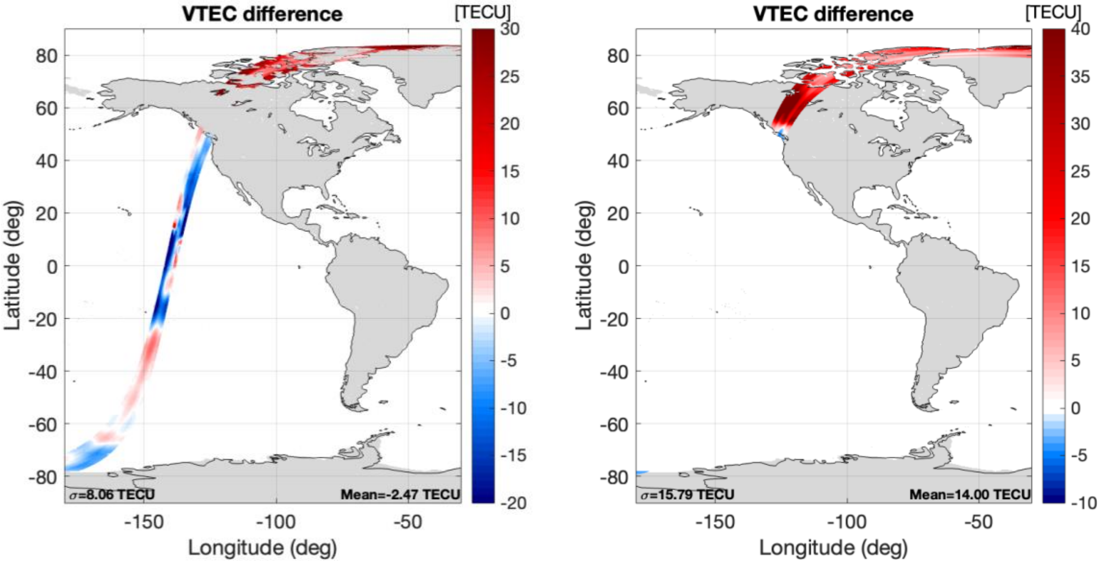

(a) (b)

Figure B.32. Difference between the recovered VTEC and the L1 VTEC snapshoots of ***descending*** *orbit of the core methodology, applying a Threshold1 = 3: (a) over ocean, (b) over land.*

- Threshold1 = 5:

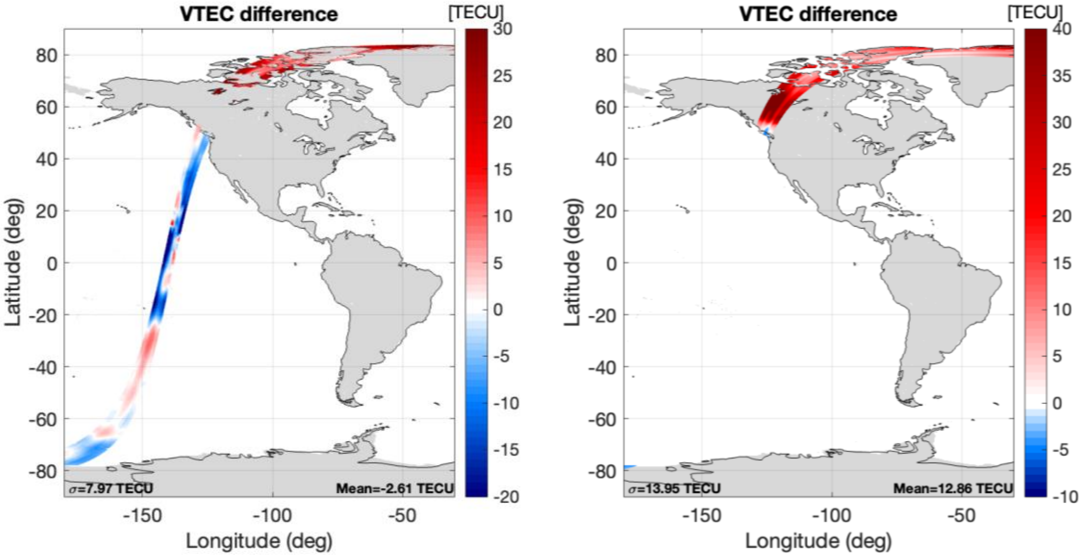

(a) (b)

Figure B.33. Difference between the recovered VTEC and the L1 VTEC snapshoots of ***descending*** *orbit of the core methodology, applying a Threshold1 = 5: (a) over ocean, (b) over land.*

- **Threshold2**: has an original value of 0.9 Kelvin.
    - Threshold2 = 0.5:

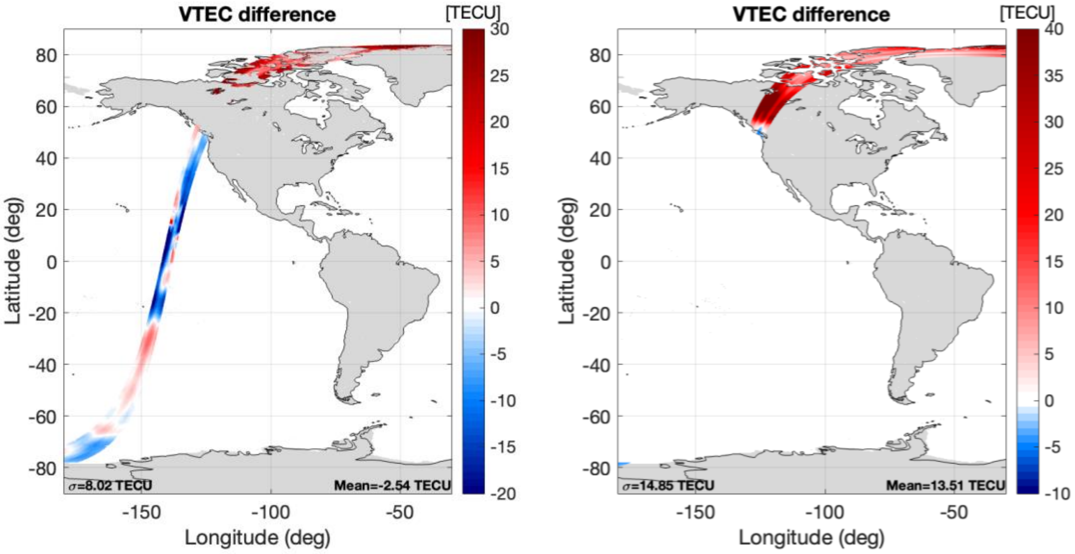

(a) (b)

*Figure B.34. Difference between the recovered VTEC and the L1 VTEC snapshoots of **descending** orbit of the core methodology, applying a Threshold2 = 0.5: (a) over ocean, (b) over land.*

- Threshold2 = 0.8:

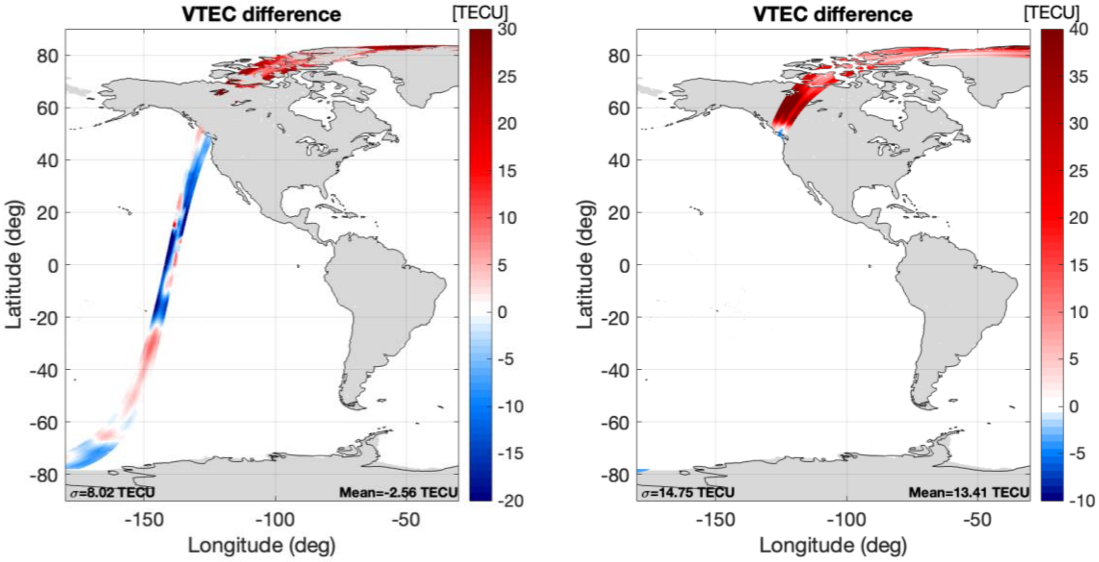

(a) (b)

*Figure B.35. Difference between the recovered VTEC and the L1 VTEC snapshoots of **descending** orbit of the core methodology, applying a Threshold2 = 0.8: (a) over ocean, (b) over land.*

- <u>Threshold2 = 1</u>:

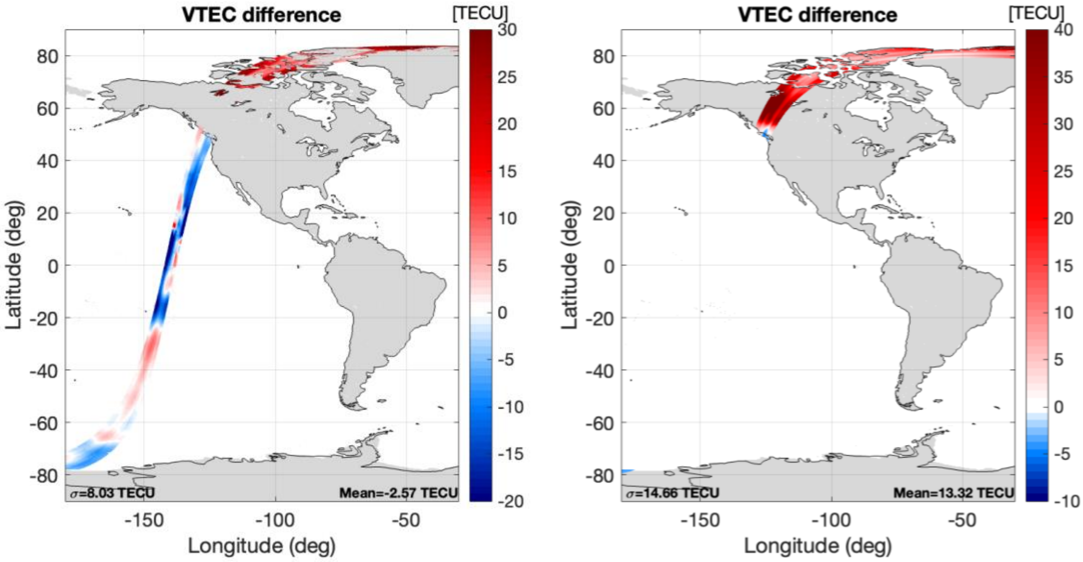

(a) (b)

Figure B.36. Difference between the recovered VTEC and the L1 VTEC snapshoots of ***descending*** *orbit of the core methodology, applying a <u>Threshold2 = 1</u>: (a) over ocean, (b) over land.*

- <u>Threshold2 = 1.3</u>:

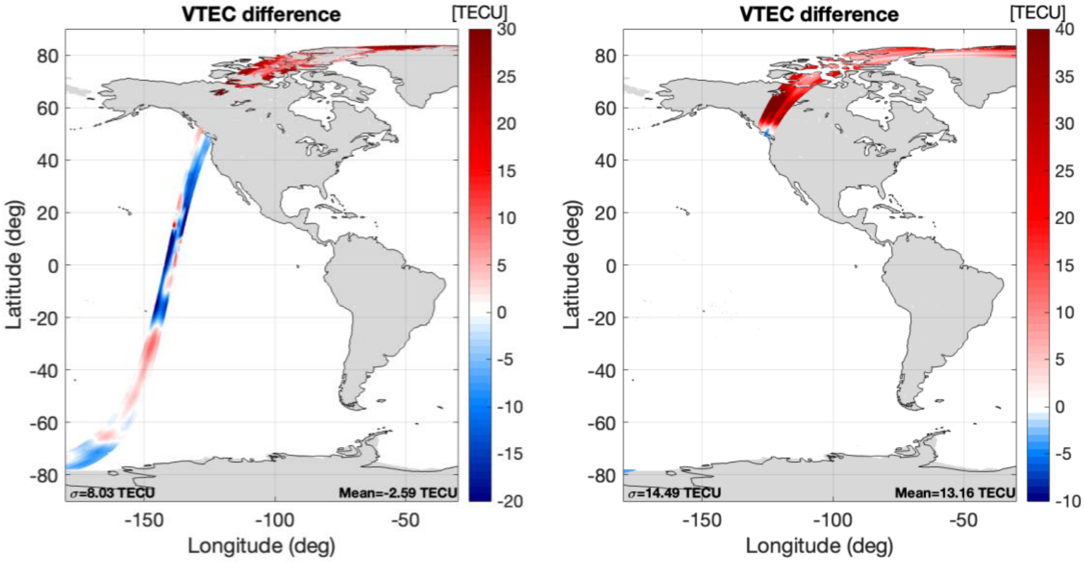

(a) (b)

Figure B.37. Difference between the recovered VTEC and the L1 VTEC snapshoots of ***descending*** *orbit of the core methodology, applying a <u>Threshold2 = 1.3</u>: (a) over ocean, (b) over land.*

- **Size Temporal Filter**: has an original value of 43 snapshoots.
  - Size Temporal Filter = 41:

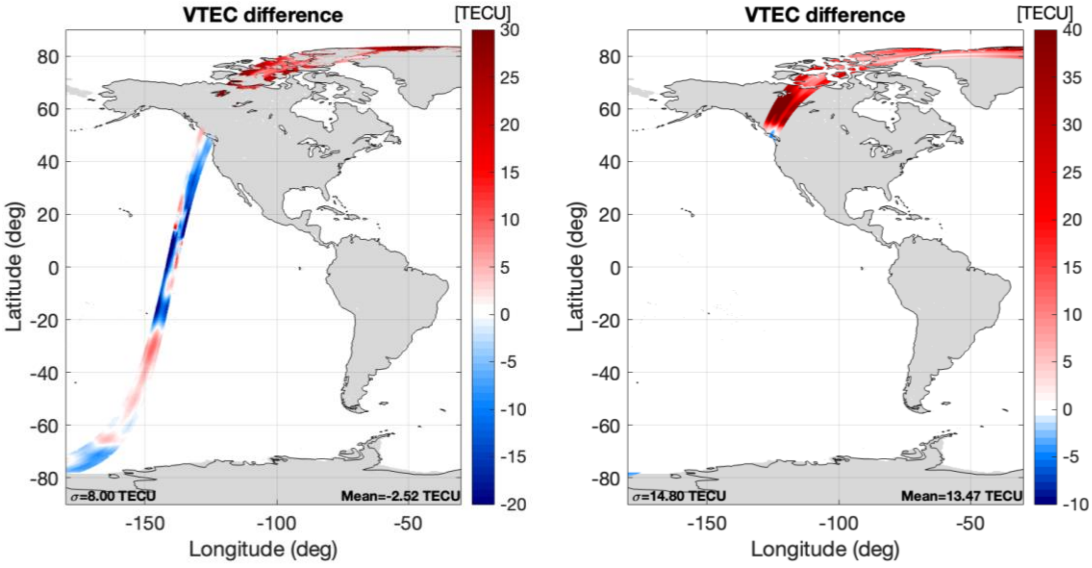

(a) (b)

*Figure B.38. Difference between the recovered VTEC and the L1 VTEC snapshoots of **descending** orbit of the core methodology, applying a Size Temporal Filter = 41: (a) over ocean, (b) over land.*

- Size Temporal Filter = 45:

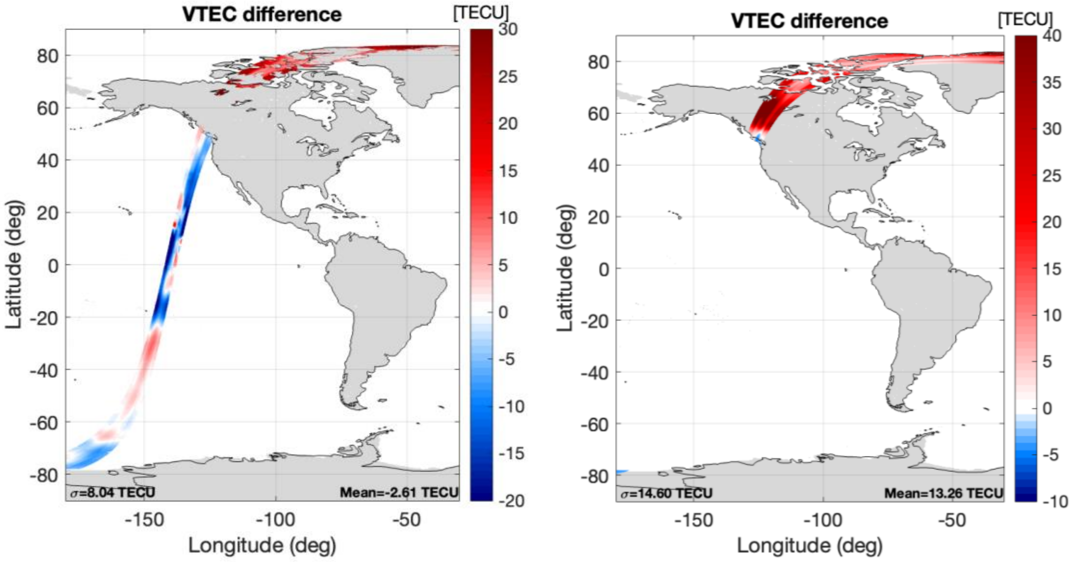

(a) (b)

*Figure B.39. Difference between the recovered VTEC and the L1 VTEC snapshoots of **descending** orbit of the core methodology, applying a Size Temporal Filter = 45: (a) over ocean, (b) over land.*

- **Size Spatial Filter**: has an original value of 0.189 d/λ.
    - Size Spatial Filer = 0.175:

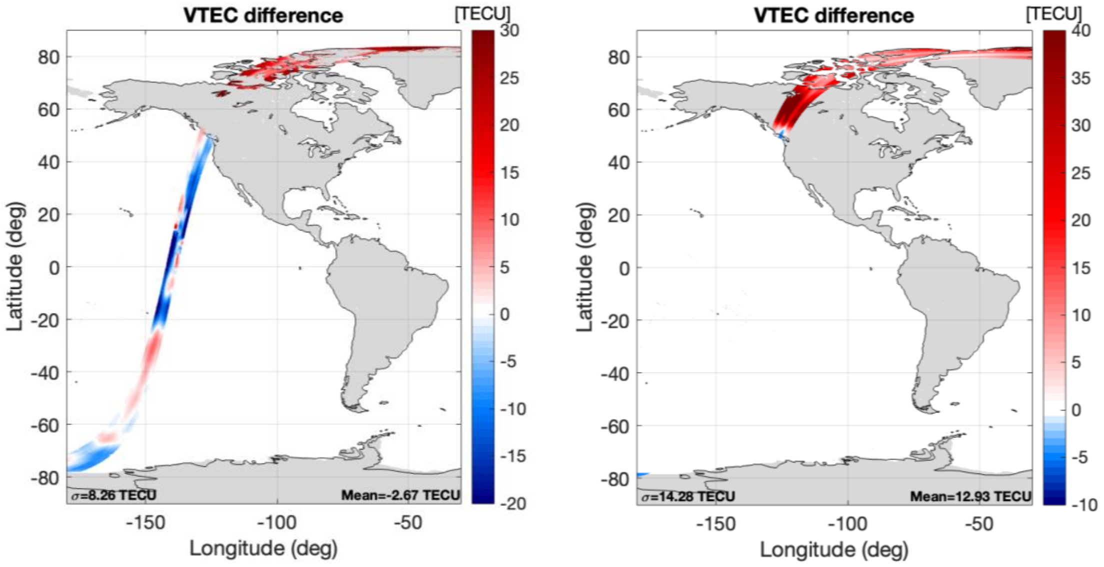

(a) (b)

*Figure B.40. Difference between the recovered VTEC and the L1 VTEC snapshoots of **descending** orbit of the core methodology, applying a Size Spatial Filter = 0.175: (a) over ocean, (b) over land.*

- Size Spatial Filter = 0.18:

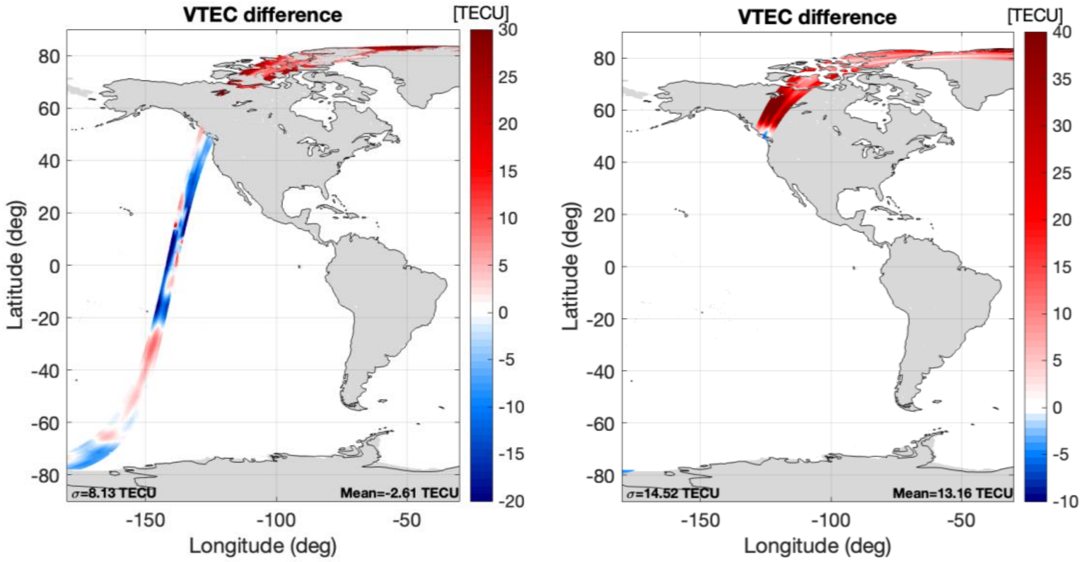

(a) (b)

*Figure B.41. Difference between the recovered VTEC and the L1 VTEC snapshoots of **descending** orbit of the core methodology, applying a Size Spatial Filter = 0.18: (a) over ocean, (b) over land.*

- Size Spatial Filer = 0.195:

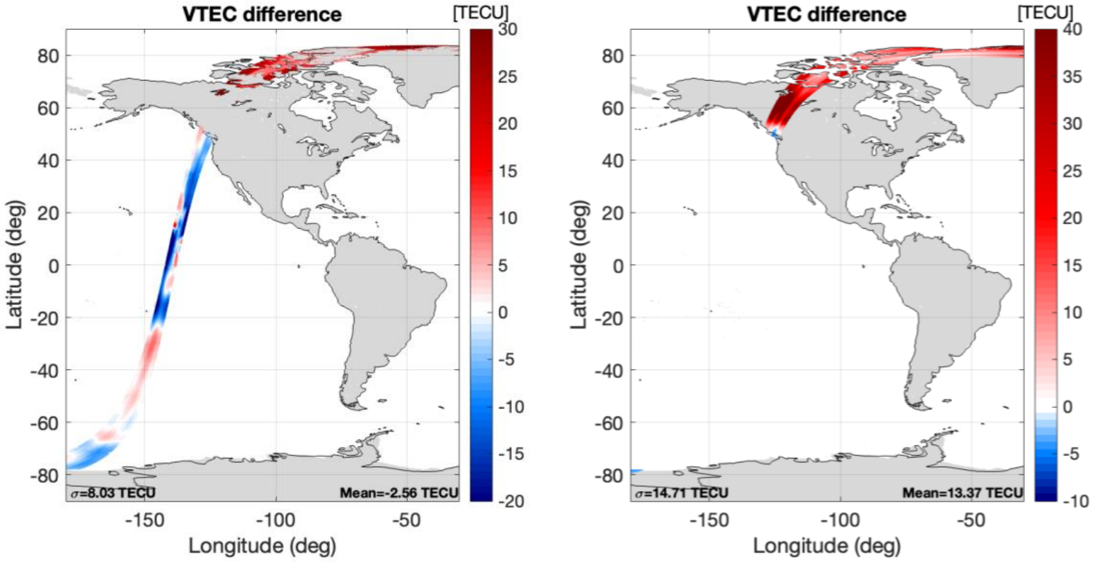

(a) (b)

Figure B.42. Difference between the recovered VTEC and the L1 VTEC snapshoots of ***descending*** *orbit of the core methodology, applying a Size Spatial Filter = 0.195: (a) over ocean, (b) over land.*

- Size Spatial Filter = 0.2:

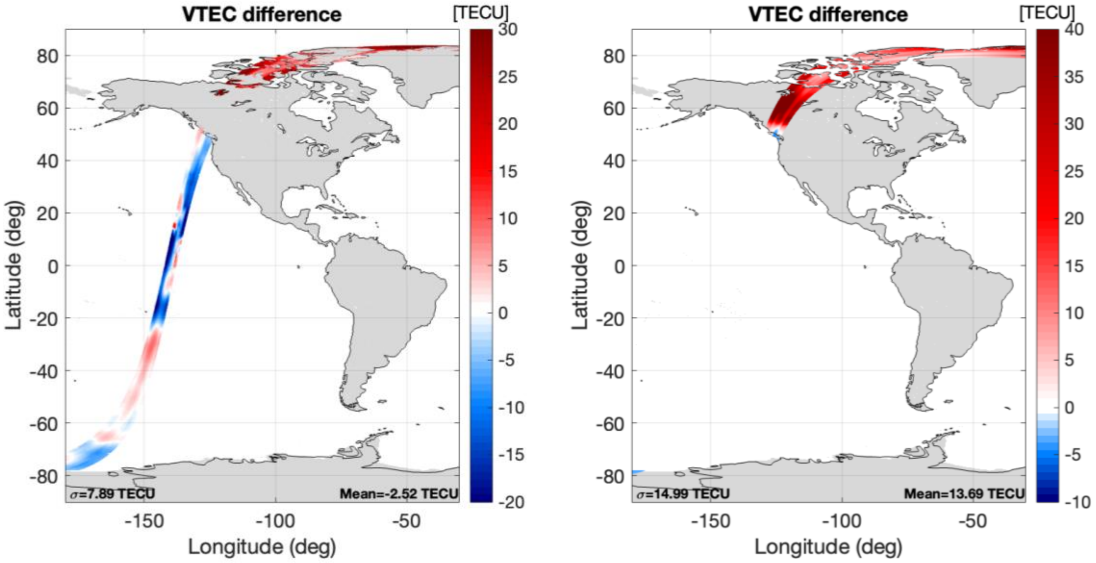

(a) (b)

Figure B.43. Difference between the recovered VTEC and the L1 VTEC snapshoots of ***descending*** *orbit of the core methodology, applying a Size Spatial Filter = 0.2: (a) over ocean, (b) over land.*

- **Incidence Angle**: has an original value of 25º.
    - Incidence Angle = 23:

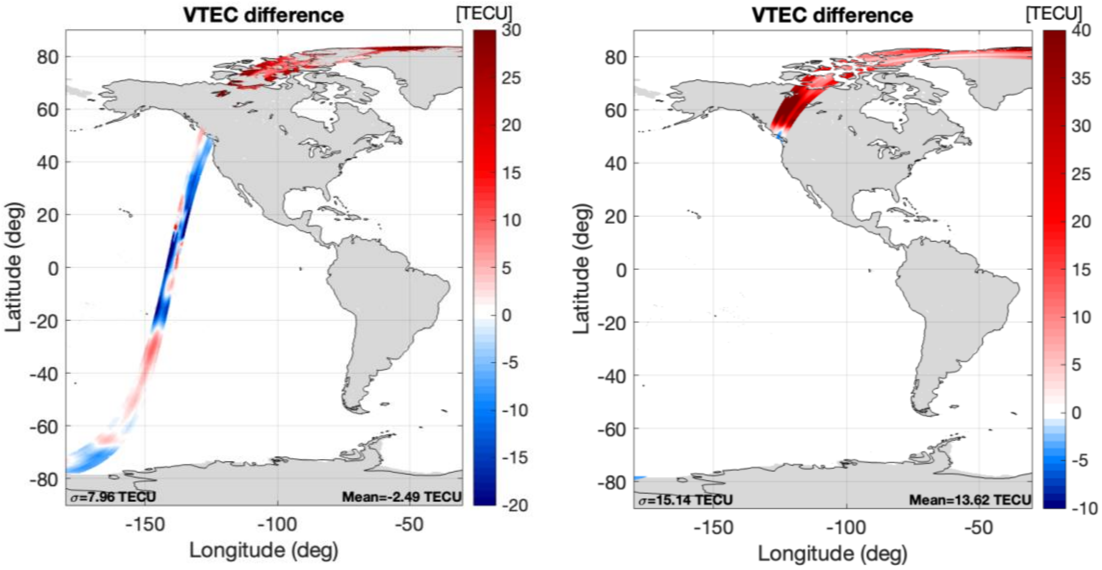

(a) (b)

*Figure B.44. Difference between the recovered VTEC and the L1 VTEC snapshoots of **descending** orbit of the core methodology, applying a Incidence Angle = 23: (a) over ocean, (b) over land.*

- Incidence Angle = 24:

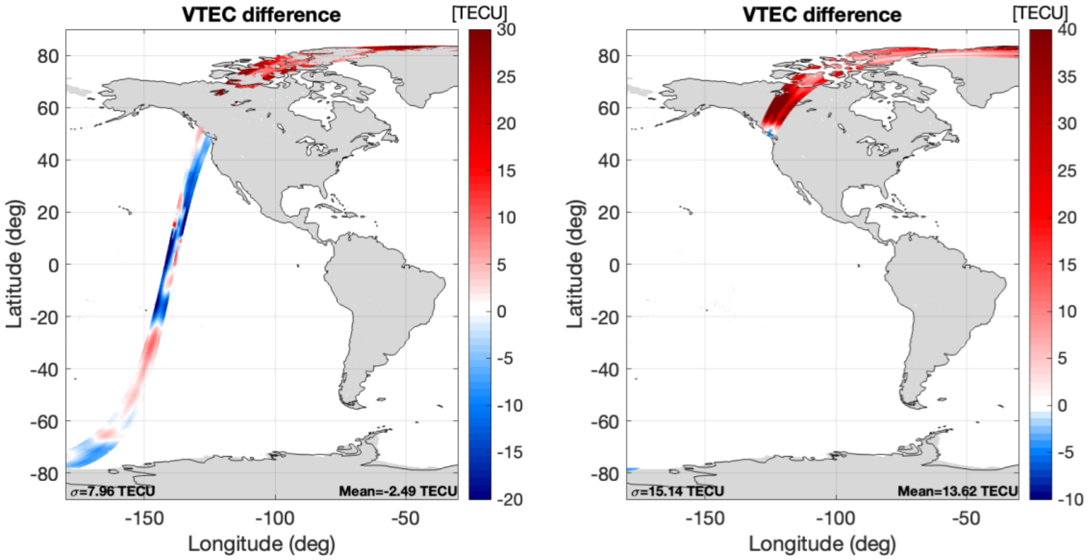

(a) (b)

*Figure B.45. Difference between the recovered VTEC and the L1 VTEC snapshoots of **descending** orbit of the core methodology, applying a Incidence Angle = 24: (a) over ocean, (b) over land.*

B.2.2. Ascending orbit

- **Threshold1**: has an original value of 4 Kelvin.
    - Threshold1 = 2:

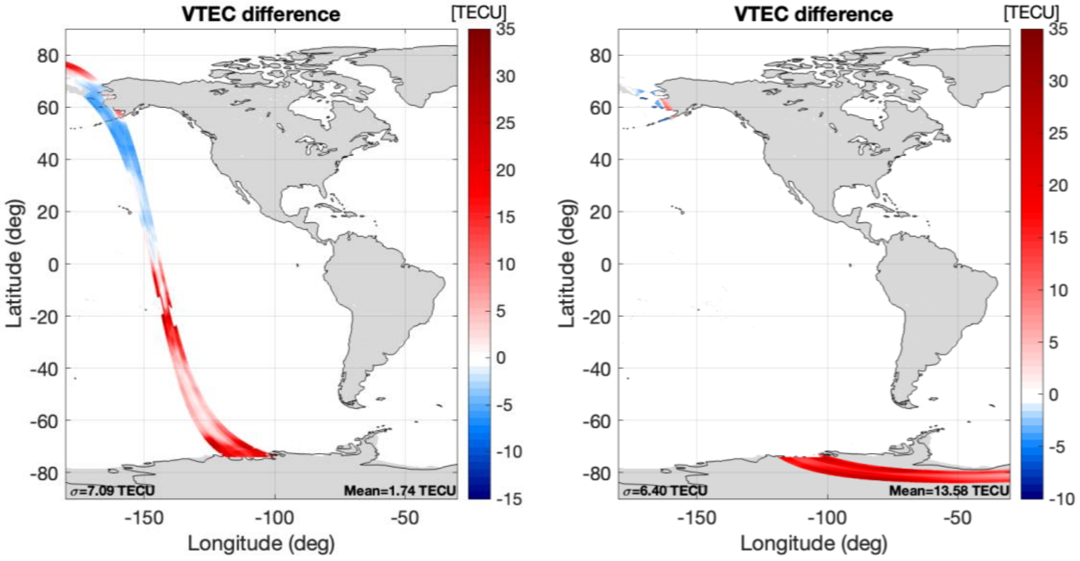

(a) (b)

Figure B.46. Difference between the recovered VTEC and the L1 VTEC snapshoots of ***ascending*** *orbit of the core methodology, applying a* *<u>Threshold1 = 2</u>**: (a) over ocean, (b) over land.*

- Threshold1 = 3:

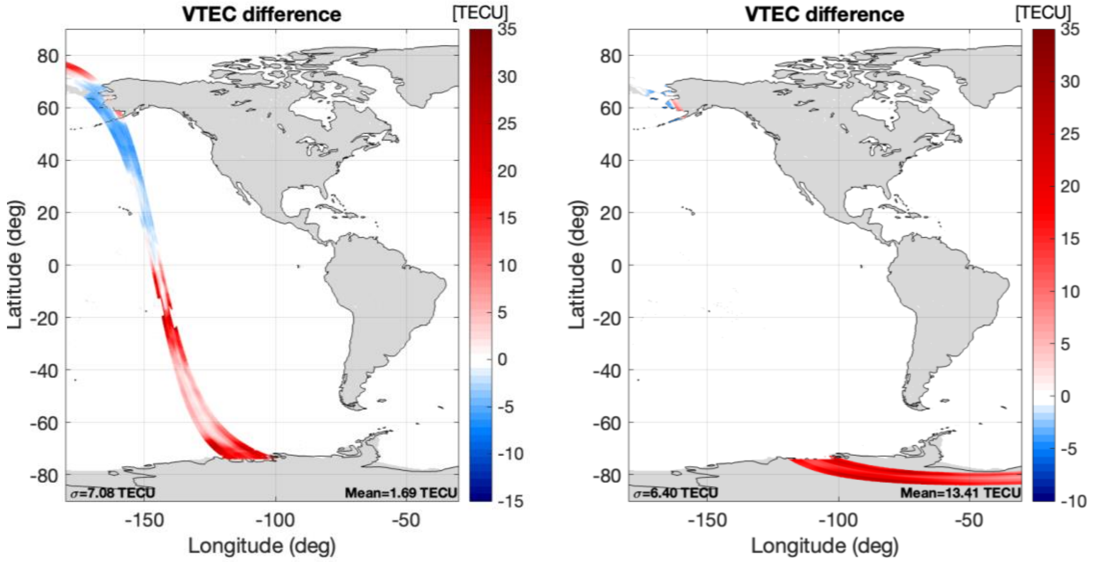

(a) (b)

Figure B.47. Difference between the recovered VTEC and the L1 VTEC snapshoots of ***ascending*** *orbit of the core methodology, applying a* *<u>Threshold1 = 3</u>**: (a) over ocean, (b) over land.*

- ○ <u>Threshold1 = 5</u>:

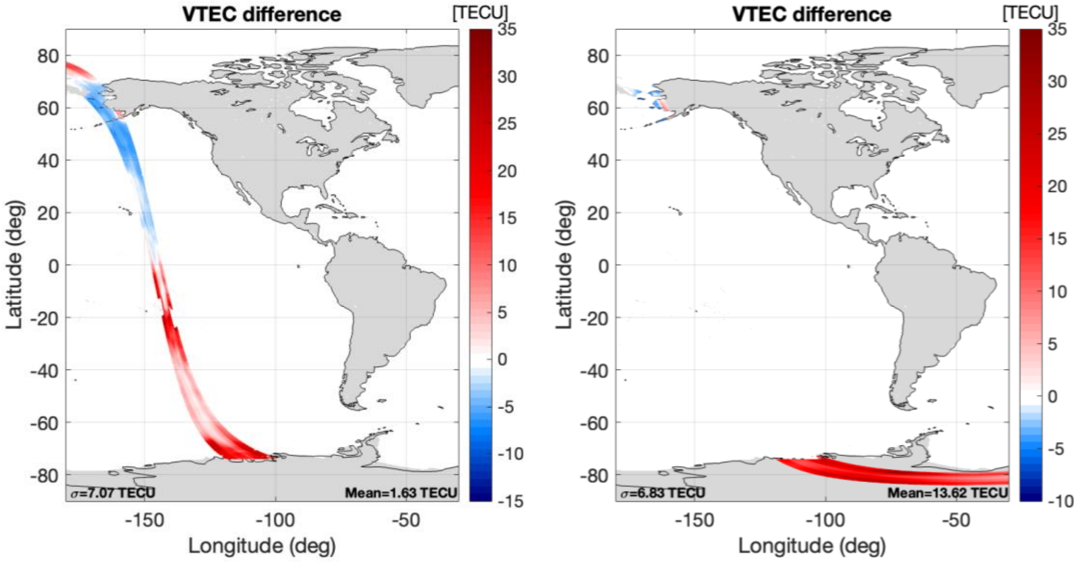

(a) (b)

*Figure B.48. Difference between the recovered VTEC and the L1 VTEC snapshoots of **ascending** orbit of the core methodology, applying a <u>Threshold1 = 5</u>: (a) over ocean, (b) over land.*

- **<u>Threshold2</u>**: has an original value of 0.9 Kelvin.

  - ○ <u>Threshold2 = 0.5</u>:

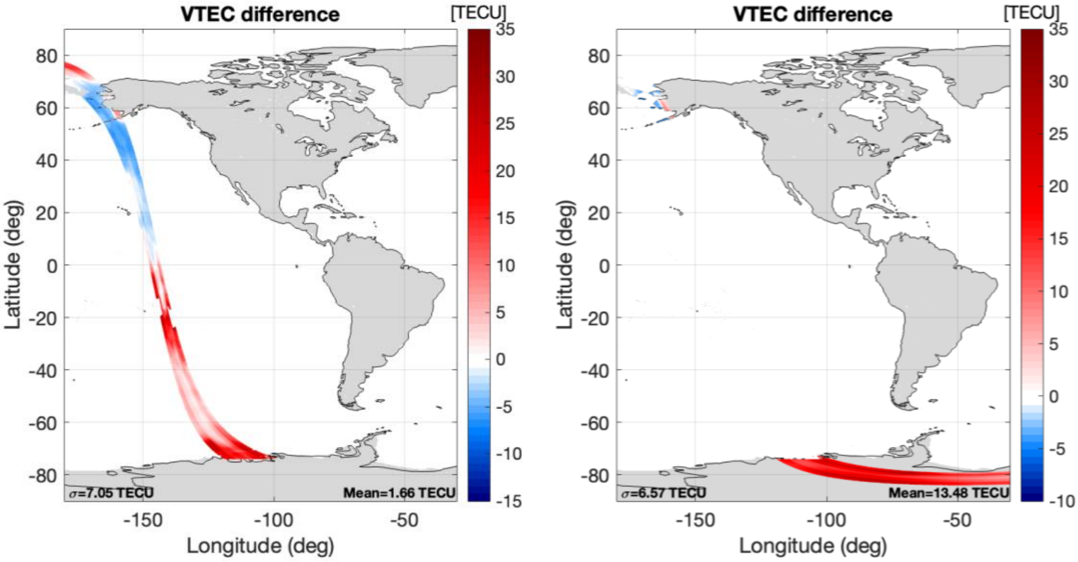

(a) (b)

*Figure B.49. Difference between the recovered VTEC and the L1 VTEC snapshoots of **ascending** orbit of the core methodology, applying a <u>Threshold2 = 0.5</u>: (a) over ocean, (b) over land.*

- Threshold2 = 0.8:

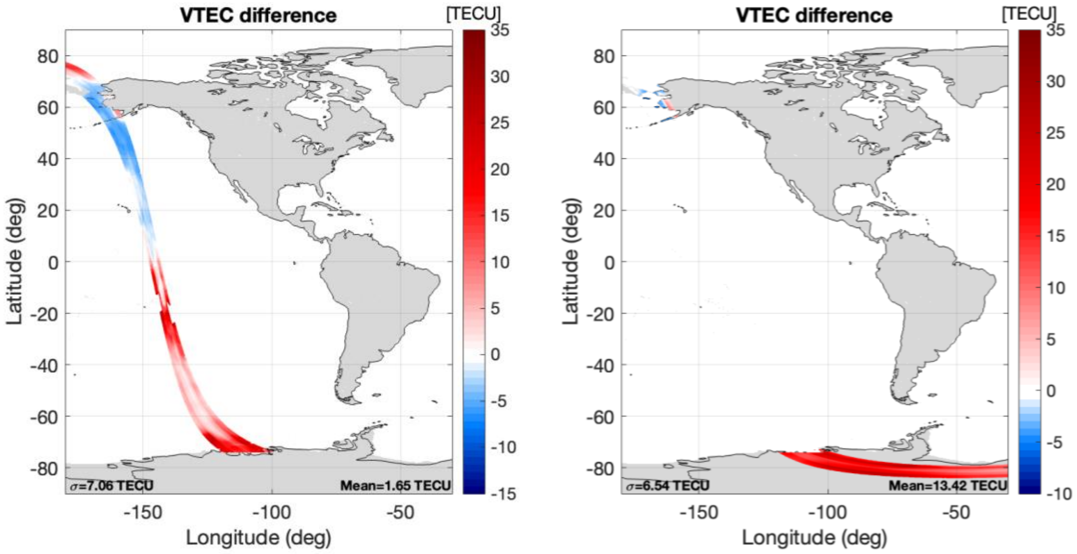

(a) (b)

Figure B.50. Difference between the recovered VTEC and the L1 VTEC snapshoots of ***ascending*** *orbit of the core methodology, applying a* <u>*Threshold2 = 0.8*</u>*: (a) over ocean, (b) over land.*

- Threshold2 = 1:

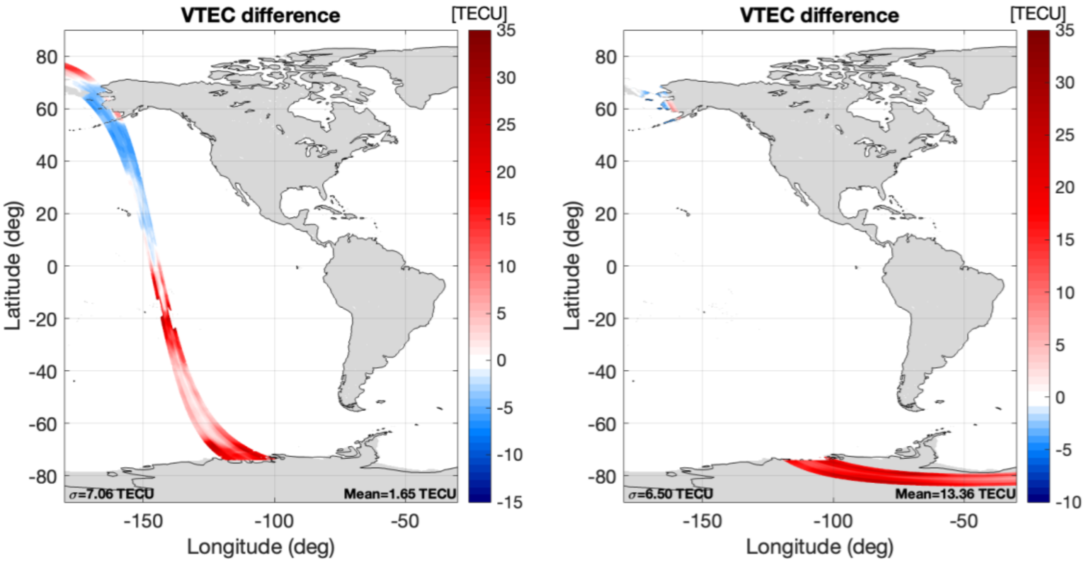

(a) (b)

Figure B.51. Difference between the recovered VTEC and the L1 VTEC snapshoots of ***ascending*** *orbit of the core methodology, applying a* <u>*Threshold2 = 1*</u>*: (a) over ocean, (b) over land.*

- Threshold2 = 1.3:

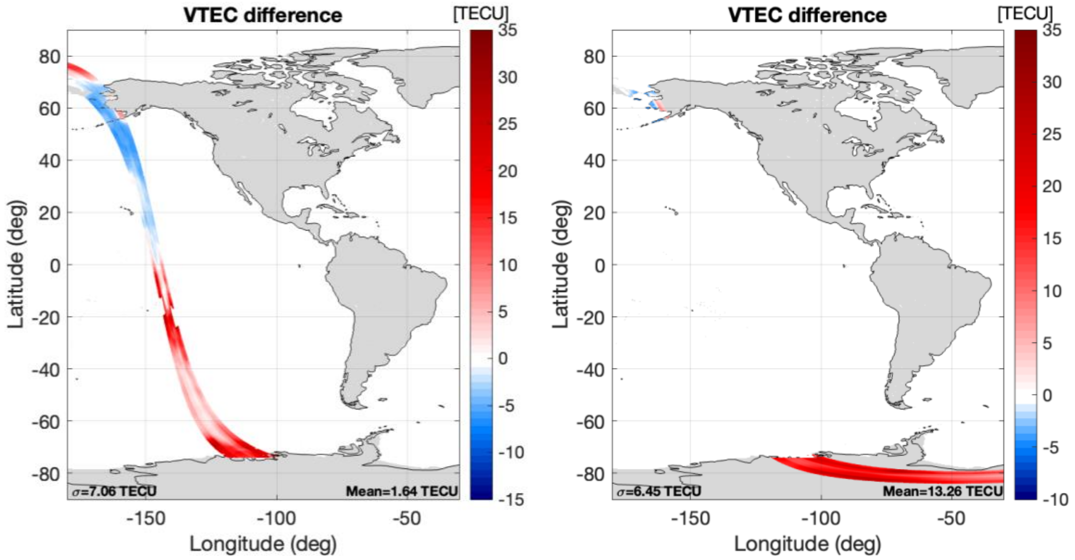

(a) (b)

Figure B.52. Difference between the recovered VTEC and the L1 VTEC snapshoots of ***ascending*** *orbit of the core methodology, applying a Threshold2 = 1.3: (a) over ocean, (b) over land.*

- **Size Temporal Filter**: has an original value of 43 snapshoots.
  - Size Temporal Filter = 41:

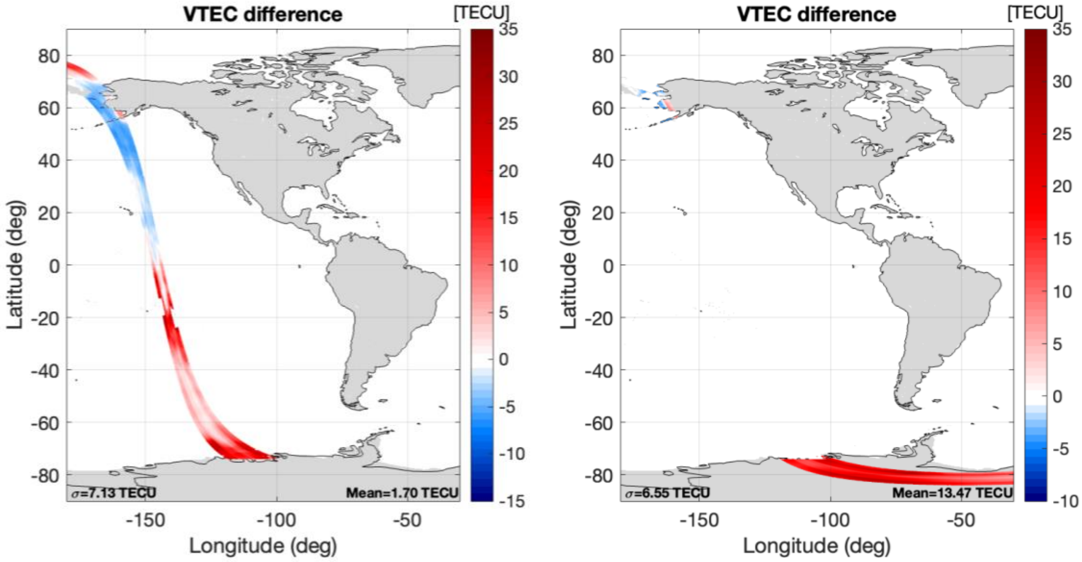

(a) (b)

Figure B.53. Difference between the recovered VTEC and the L1 VTEC snapshoots of ***ascending*** *orbit of the core methodology, applying a Size Temporal Filer = 41: (a) over ocean, (b) over land.*

- Size Temporal Filter = 45:

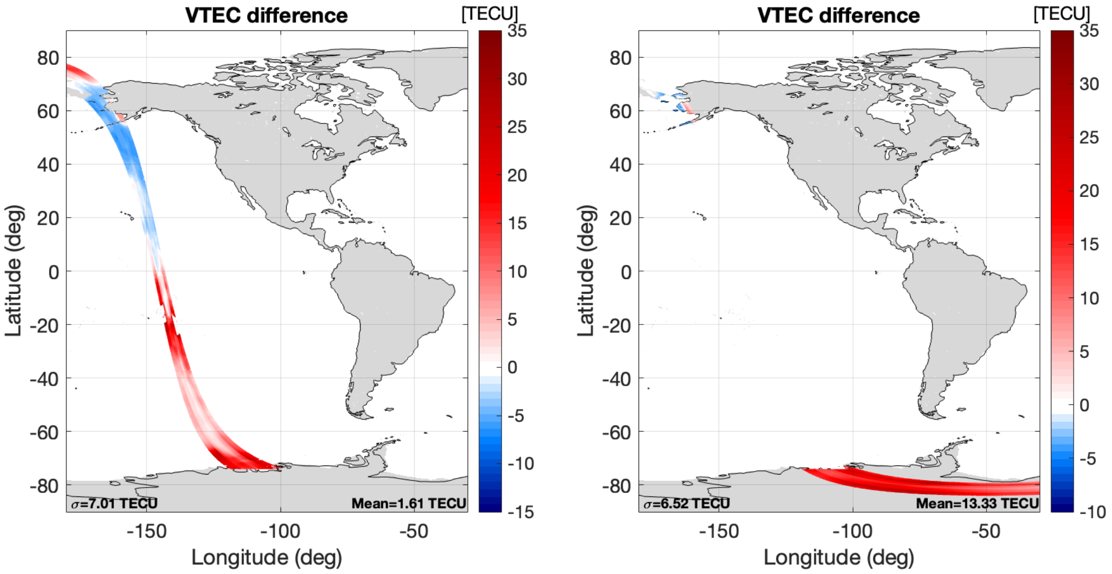

(a) (b)

Figure B.54. Difference between the recovered VTEC and the L1 VTEC snapshoots of ***ascending*** *orbit of the core methodology, applying a Size Temporal Filer = 45: (a) over ocean, (b) over land.*

- **Size Spatial Filter**: has an original value of 0.189 d/λ.
  - Size Spatial Filer = 0.175:

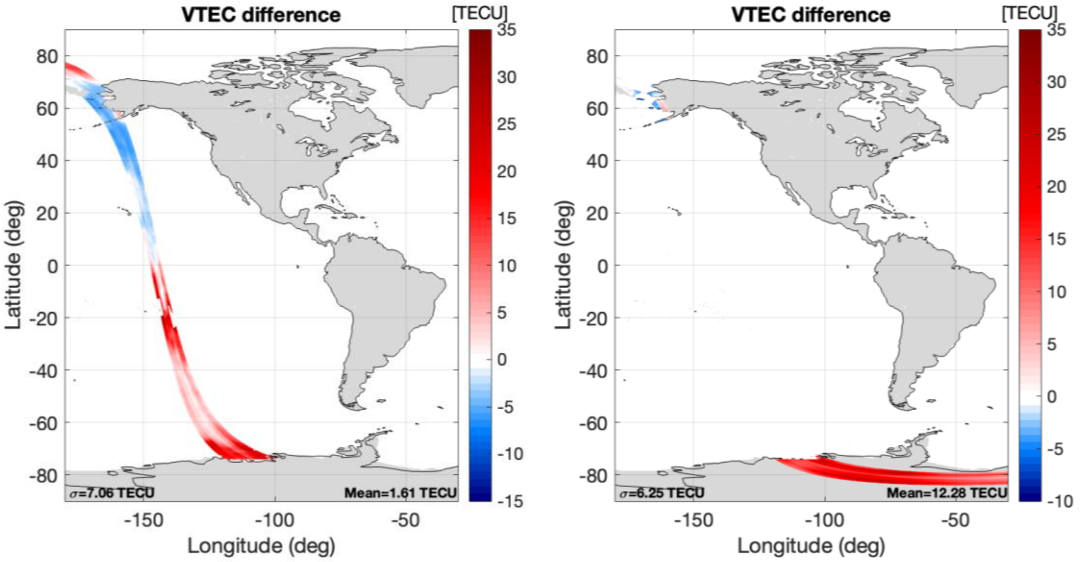

(a) (b)

Figure B.55. Difference between the recovered VTEC and the L1 VTEC snapshoots of ***ascending*** *orbit of the core methodology, applying a Size Spatial Filer = 0.175: (a) over ocean, (b) over land.*

- <u>Size Spatial Filter = 0.18</u>:

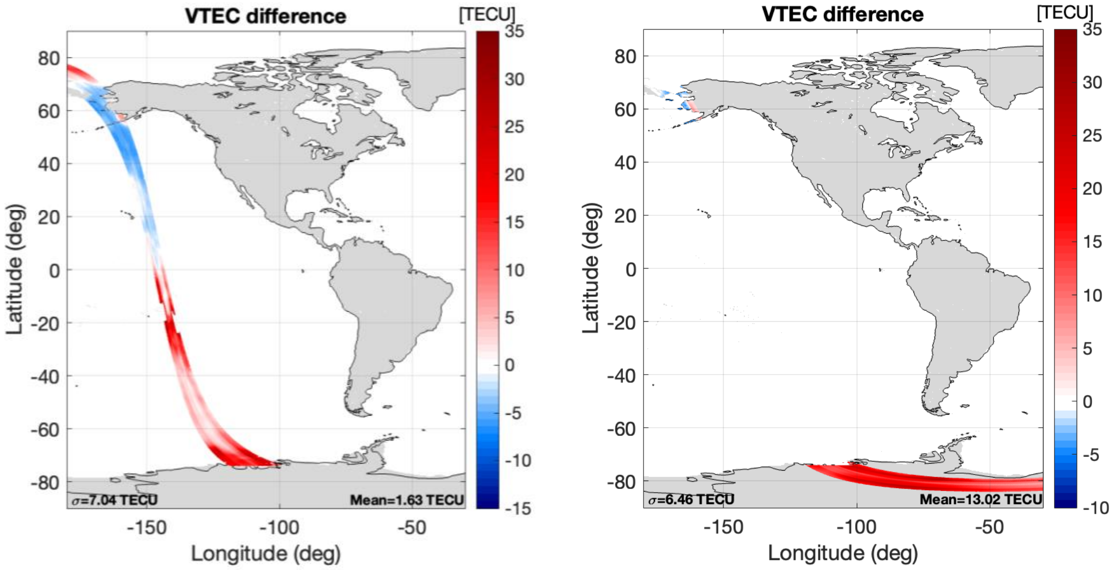

(a) (b)

Figure B.56. Difference between the recovered VTEC and the L1 VTEC snapshoots of ***ascending*** *orbit of the core methodology, applying a* *<u>Size Spatial Filer = 0.18</u>**: (a) over ocean, (b) over land.*

- <u>Size Spatial Filer = 0.195</u>:

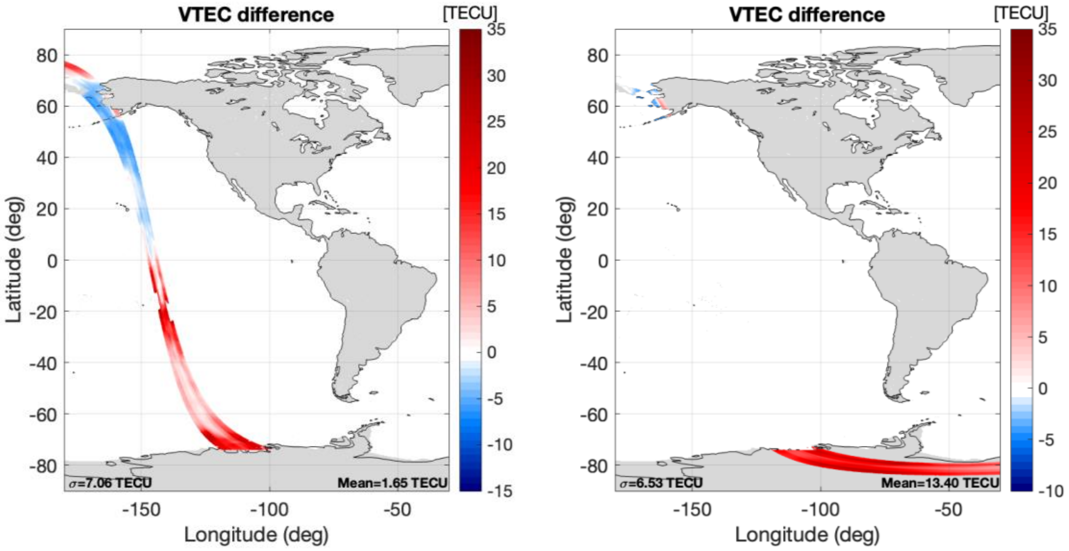

(a) (b)

Figure B.57. Difference between the recovered VTEC and the L1 VTEC snapshoots of ***ascending*** *orbit of the core methodology, applying a* *<u>Size Spatial Filer = 0.195</u>**: (a) over ocean, (b) over land.*

- <u>Size Spatial Filter = 0.2</u>:

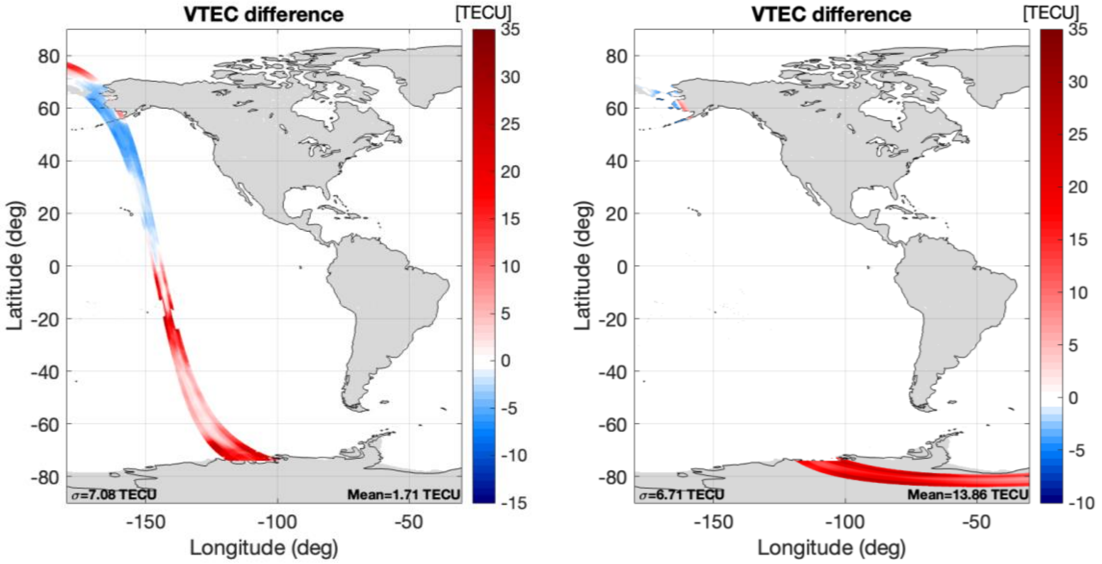

(a) (b)

Figure B.58. Difference between the recovered VTEC and the L1 VTEC snapshoots of ***ascending*** *orbit of the core methodology, applying a <u>Size Spatial Filer = 0.2</u>: (a) over ocean, (b) over land.*

- **<u>Incidence Angle</u>**: has an original value of 25º.

  - <u>Incidence Angle = 23</u>:

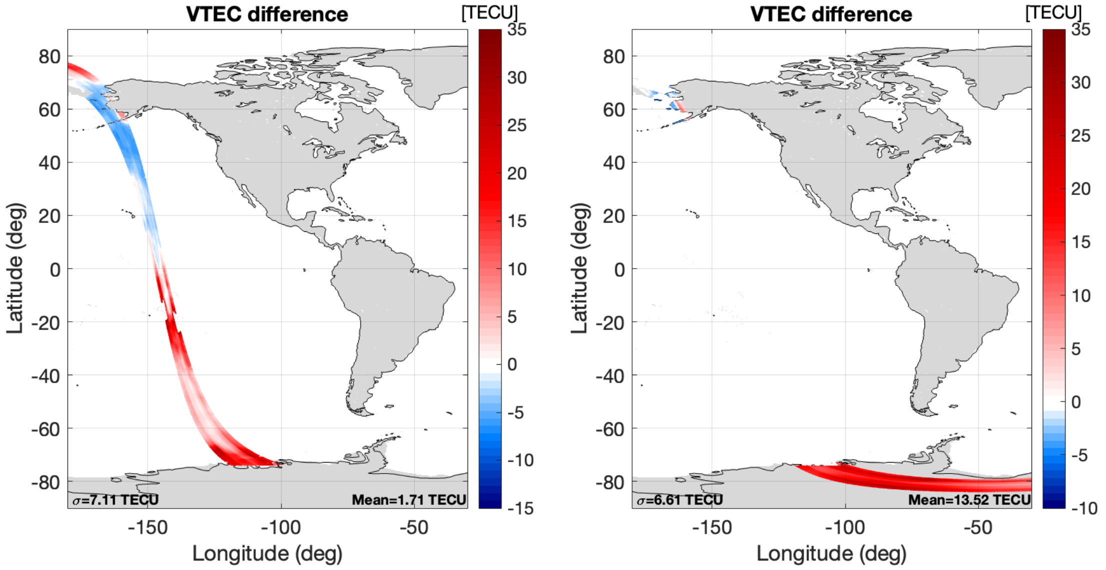

(a) (b)

Figure B.59. Difference between the recovered VTEC and the L1 VTEC snapshoots of ***ascending*** *orbit of the core methodology, applying a <u>Incidence Angle = 23</u>: (a) over ocean, (b) over land.*

- <u>Incidence Angle = 24</u>:

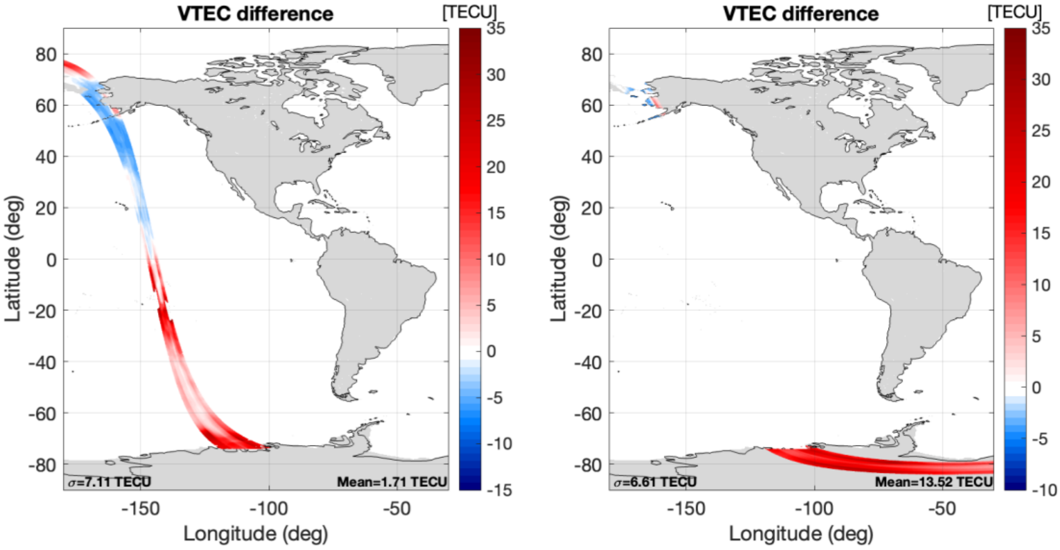

(a) (b)

Figure B.60. Difference between the recovered VTEC and the L1 VTEC snapshoots of ***ascending*** *orbit of the core methodology, applying a* *<u>Incidence Angle = 24</u>: (a) over ocean, (b) over land.*

Glossary

UPC: Universitat Politècnica de Catalunya.

SMOS: Soil Moisture and Ocean Salinity.

ESA: European Space Agency.

VTEC: Vertical Total Electron Content.

FRA: Faraday Rotation Angle.

FR: Faraday Rotation.

MIRAS: Microwave Imaging Radiometer with Aperture Synthesis.

MTS: MIRAS Testing Software.

TB: Brightness Temperature.

LICEF: Lightweight Cost-Effective Front-End.

NIRS: Noise Injection Radiometers.

FoV: Field of View.

AF-FoV: Alias-Free Field of View.

EAF-FoV: Extended Alias-Free Field of View.

ISEA: Icosahedral Snyder Equal Area.

LT: Local Time.

IGS: International GNSS Service.

GNSS: Global Navigation Satellite Systems.

IGRF: International Geomagnetic Reference Field.

A3TEC: Total Electron Content from Third Strokes Parameter at Antenna Level.

OTT: Ocean Target Transformation.

STD: Standard Derivation.

TEC: Total Electron Content.

TECU: TEC Unit.

L1: SMOS L1 data product.

L1A: SMOS Level 1A data product.

L1B: SMOS Level 1B data product.

L1C: SMOS Level 1C data product.